A SLOWLY PROGRESSIVE AND REPRODUCIBLE ANIMAL MODEL OF INTERVERTEBRAL DISC DEGENERATION CHARACTERIZED BY MRI: DEVELOPMENT OF A CUSTOM QUAD COIL FOR HIGH RESOLUTION SCANNING AT 3.0T

by

John F. Kompel

BS, University of Pittsburgh, 2001

Submitted to the Graduate Faculty of

School of Engineering in partial fulfillment

of the requirements for the degree of

Master of Science in Bioengineering

University of Pittsburgh

2007

UNIVERSITY OF PITTSBURGH

SCHOOL OF ENGINEERING

This thesis was presented

by

John F. Kompel

It was defended on

April 14, 2005

and approved by

James D. Kang, MD, Orthopaedic Surgery

Doug Robertson, MD, Ph.D, Orthopaedic Surgery

Fernando Boada, Ph.D, Bioengineering Department

Thesis Advisor: Lars G. Gilberston, Ph.D, Orthopaedic Surgery

A SLOWLY PROGRESSIVE AND REPRODUCIBLE ANIMAL MODEL OF INTERVERTEBRAL DISC DEGENERATION CHARACTERIZED BY MRI: DEVELOPMENT OF A CUSTOM QUAD COIL FOR HIGH RESOLUTION SCANNING AT 3.0T

John F.Kompel, M.S.

University of Pittsburgh, 2007

STUDY DESIGN: The progression of intervertebral disc degeneration (IDD) follows anterolateral "stab" of adult rabbit lumbar discs by 16-gauge hypodermic needle to a limited (5-mm) depth was studied for up to 24 weeks using magnetic resonance imaging (MRI).

OBJECTIVES: To develop a slowly progressive, reproducible rabbit model of IDD suitable for studying pathogenesis and pathopysiology of intervertebral disc degeneration. Moreover, to improve the MRI methods and achieve improved MRIs a custom quad coil tuned and matched for 3.0T was developed. Higher SNR achievable with this coil allowed the acquisition of higher resolution images.

METHODS: Part1 - The L2-L3, L3-L4, and L4-L5 lumbar intervertebral discs of 18 skeletally mature female New Zealand White (NZW) rabbits were stabbed by 16-gauge hypodermic needle to a depth of 5-mm in the left anterolateral annulus fibrosis (AF). Serial MRI scans of the stabbed discs and intact L1-2 and L5-6 control discs were performed at 3, 6, 12, and 24 weeks post surgery and compared with preoperative MRIs. Development of the quad coil at 3.0T was competed with reference phantom to demonstrate the advantages over the 5 inch surface coil at 1.5T. To further illustrate the coils advantages in-vivo rabbit MRIs were obtained with the custom coil and compared to the 5 inch surface coil at 1.5T

RESULTS: The stabbed discs exhibited a progressive decrease in "MRI Index" (the product of nucleus pulposus (NP) area and signal intensity from T2-weighted midsagittal plane images) starting at 3 weeks post stab and continuing through 24 weeks, with no evidence of spontaneous recovery or reversal of MRI changes. In addition, the constructed quad coil at 3.0T demonstrated the ability to obtain high resolution scans with SNR comparable to the 5 inch surface coil at 1.5T.

CONCLUSIONS: Stabbing the anterolateral AF of adult rabbit lumbar discs with a 16-gauge hypodermic needle to a limited (5-mm) depth results in a number of slowly progressive and reproducible MRI changes over 24 weeks that show a similarity to changes seen in human IDD. This model would appear suitable for studying pathogenesis and pathophysiology of IDD and testing safety and efficacy of novel treatments of IDD.

TABLE OF CONTENTS

LIST OF TABLES

LIST OF FIGURES

1.0 INTRODUCTION

1.1 INTERVERTEBRAL DISC DEGENERATION

The intervertebral disc undergoes degeneration during the natural aging process (Benoist, 2003 #52). IDD involves a number of biological and mechanical changes which include water loss, tears in the annulus, disc herniation, protrusion, and height loss (Niosi, 2004 #48; Walker, 2004 #49). IDD is a major contributor to low back pain, while its etiology and pathophysiology remain widely studied (Guiot, 2000 #47)

Aging is the most common cause of disc degeneration, which is referred to as primary disc degeneration. As the body ages, the discs in the spine dehydrate, or dry out, and lose their ability to act as shock absorbers between the vertebra. The bones and ligaments that make up the spine also become less flexible and thicken. Unlike muscles, there is minimal blood supply to the discs so they lack the ability to heal or repair (Coventry, 1951 #10).

Intervertebral discs can also undergo more rapid changes than that of the natural aging process and is termed secondary disc degeneration. For example, discs adjacent to a spinal fusion or degeneration following an annular tear. Smoking, obesity, and high spinal mechanical loads are other factors connected with secondary disc degeneration (Yoon, 2004 #33) (Danielsson, 2001 #12)

1.1.1 Impact of IDD

Low back pain is one of the most common medical conditions, afflicting approximately 85% of all persons sometime during their lives. Annually, 2% of the national work force incurs industrially related back injuries. A review of the epidemiologic studies showed that the peak incidence of low-back pain occurred in the persons' most productive years, within the age range if 25-60 years. Also, approximately 20% of the population studied had been incapacitated for periods ranging from 3 weeks to 6 months, and 4% had been incapacitated for more than 6 months (Bigos, 1986 #7).

The prevalence of musculoskeletal impairments of the spine in the U.S. is estimated to be greater than 18 million—many of which are the direct or indirect result of intervertebral disc disease (Georgy, 1994 #17). The limited available technology for the treatment of disc herniation and other pathologic and disabling conditions arising from IDD generally is highly invasive (e.g., surgical discectomy and fusion), manifesting a certain degree of complications and unsatisfactory clinical outcomes. To date, little effort has been made to directly treat the underlying problem of disc degeneration—a chronic process characterized in part by progressive loss of proteoglycans leading to disc dehydration, alterations in disc structure, and impaired disc function. (Deyo, 1991 #13) (Evans, 1989 #14).

1.1.2 Treatments of IDD

The first step in the recovery from IDD is non-surgical treatment. Some conservative therapies include physical therapy, where physical therapists will work with patients to strengthen and stretch the lower back, leg, and stomach muscles. Also, chiropractic manipulation is a primary treatment for patients with back or neck pain to restore the joints to more normal motion. Moreover, medications can be prescribed, which include pain relievers, nonsteroidal anti-inflammatory medications (NSAIDs), and steroids. If there is an unfavorable respond to this treatment a doctor may recommend surgery, which normally involves a highly invasive procedure.

Current surgical techniques for treating IDD are limited and are rarely recommended unless a patient has a proven disc herniation or instability and the symptoms do not significantly improve with non-surgical treatments. Inter-body Fusion is a surgical procedure in which one or more of the bony vertebrae of the spine are permanently joined together to provide stability to the spine. Spinal fusion can be performed at any level of the spine but is most common in the lumbar and cervical regions where it is most moveable. Discectomy is a common surgical treatment for ruptured or herniated discs of the lumbar spine. Once the inner disc material extends out past the regular margin of the outer disc wall, it can press against very sensitive nerve tissue in the spine. The "bulging" disc can compress or even damage the nerve tissue, and this can cause weakness, tingling, or pain in the back area and into one or both legs. Open discectomy uses surgery to remove part of the damaged disc and thus relieve the pressure on the nerve tissue and alleviate the pain. Surgical approaches are not cures for IDD and their limitations are apparent.

Advancements for future treatments of IDD are currently in development. For example, potential techniques include NP replacement, artificial disc implantation, and gene therapy. If you imagine the disk as a jelly doughnut, the annulus fibrosis (a ring of cartilage between the vertebrae) is the doughnut and the nucleus pulposus (a gel-like material inside the annulus) is the jelly. If you have a herniated disk, it's as if the jelly is squeezed out of the doughnut. Research is currently underway to create an artificial replacement materials, such as hydrogels and various polymers, for the nucleus pulposus when all or part of it is removed. The objective of implanting replacement material is to maintain or restore the physiologic (normal functional) height of the intervertebral disc space, as well as the mobility and the mechanical function of the spine.

1.1.3 Magnetic Imaging of Low Back Pain

Magnetic resonance imaging (MRI) has assumed a preeminent role in the imaging evaluation of spine. It is a particularly valuable method for the clinical assessment of IVD pathology, since it offers a noninvasive method for determining whether an IVD is normal or abnormal (Georgy, 1994 #17). Owing to its multiplanar capability and superior soft tissue contrast, MRI is the procedure of choice for a host of spinal disorders including IDD, tumor evaluation, trama, and spinal deformities (Gundry, 1997 #20) (Beattie, 1998 #6). The ability to image in multiple planes allows direct visualization of complex anatomy providing greater information to the spine surgeon. This is particularly helpful in the evaluation of complex spinal deformities. MRI enables direct assessment of disc hydration and integrity, and allows for visualization of nerve roots, cauda equine, and disc and vertebral body margins (Gundry, 1997 #19).

In addition to superb demonstration of anatomic detail, manipulation of various MR imaging parameters allows accentuation of certain soft tissue properties, which in turn, reflect

underlying pathophysiologic processes. Scanning parameters used in spinal MR imaging depend on the portion of the spine being studied and the clinical question at hand. In general, images are obtained in the sagittal and axial planes. Studies are performed using proton density, T1, and T2- weighted sequences. Lumbar spine scans generally consist of sagittal T2 weighted Fast Spin Echo (FSE) images. These newer imaging techniques such as FSE result in superb image resolution and allow for shorter acquisition time, while at the same time permitting long repetition times and long echo times to obtain heavily T2 weighted images (Gundry, 1999 #41) (Modic, 1991 #50) (Boos, 1996 #8).

Quantitative MRI methods and grading systems for human IDD have been established and previously reported (Antoniou, 1998 #4) (Sether, 1990 #30) (Chatani, 1993 #9). However, there is a paucity in the literature when it comes to specifically addressing MRI changes in animal models of DDD.

1.1.4 Specialized Imaging Techniques

Numerous specialized imaging sequences have been developed that allow tailoring if spinal MR imaging examinations (Georgy, 1994 #17). Fat suppression techniques have been used in conjunction with gadolinium enhancement to improve visualization of enhancing inflammation (Georgy, 1995 #18; Georgy, 1994 #17). The short T1 inversion recovery sequence represents a type of fat suppression technique that produces images with greater sensitivity for spinal metastases compared with routines spin echo (SE) and FSE techniques. Volumetric acquired sequences allow for thin section contiguous images that can be reformatted into multiple planes from a single acquisition. Finally, phase contrast techniques enable study of cerebral spinal fluid

flow dynamics, which in turn may aid in distinction of various types of cysts occurring in the subarachnoid space (Gundry, 1997 #19).

2.0 SPECIFIC AIMS

2.1 PART 1: SOFTWARE

Development of a slowly progressive and reproducible animal model of IDD, characterized using MRI.

(A) Clinical MRI analysis of rabbit 'stab' model of IDD. An AGFA PACS workstation, which is clinically used to analyze MRIs, will be used to quantitatively assess the degeneration in rabbit lumbar discs (L1-2, L2-3, L3-4, L4-5, L5-6).

(B) MRI analysis of "stab" model will be further analyzed using AMIRA 3.0 software. This software offers a more objective approach when compared to the PACS software, which primarily is used for qualitative analysis of medical images.

2.2 PART 2: HARDWARE

Development of a custom quad coil with optimized geometry for imaging rabbit lumbar spine at 3.0T.

3.0 BACKGROUND

3.1 ANATOMY, BIOCHEMISTRY, AND PHYSIOLOGY OF THE IVD

Normally, there are 23 IVDs in the spinal column, making up roughly a quarter of the height of the column. While there is some variation in the structure between the cervical, thoracic, and lumbar regions, the basic anatomy of the disc is similar throughout the spinal column. The IVD is composed of 3 distinct parts. Human IVDs consist of an outer annulus fibrosis (AF) and a central nucleus pulposus (NP) (Coventry, 1969 #11). The annulus consists of peripheral concentric rings of collagen lamellae and a larger inner area of fibrocartilage. Anteriorly, the AF is generally thicker. The NP occupies the most central area of the disk and is separated from the inner fibrocartilaginous region of the AF by a narrow transition zone. Finally, cartilage endplates intervene between nucleus and trabecular bone and provide for longitudinal growth, and is comprised of hyaline cartilage (Eyring, 1969 #15). Throughout life the AF is roughly 60% to 70% water, whereas the water concentration in the NP declines from approximately 80% to 90% at birth to approximately 70% in adults (Pritzker, 1977 #29). Figure shows spinal column and functional spinal unit (FSU), showing nucleus pulposus and annulus fibrosus.

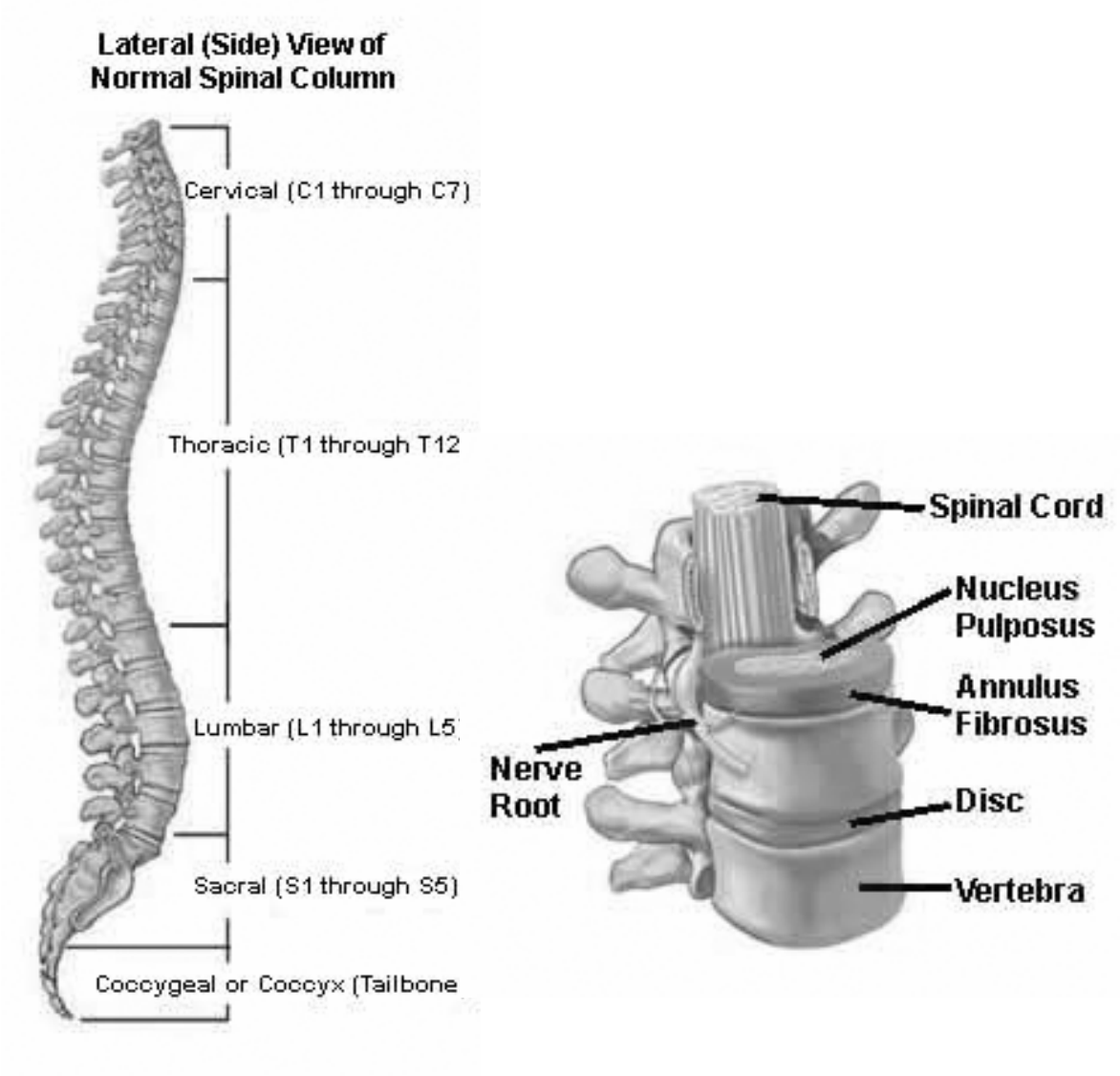

Figure 1. Lateral view of normal spinal column (A), and functional spinal unit illustrating nucleus pulposus and annulus fibrosus (B).

Collagen provides mechanical strength and structural integrity of the IVD. It accounts for approximately 50% to 60% of the dry weight of the AF, 15% to 20% of the dry weight of the NP, and 50% to 70% of the endplate. In the annulus, the concentration of type I collagen decreases from approximately 80% of the total collagen in the outermost region to less than 1% in the NP, and the concentration of type II collagen increases from less than 1% to approximately 80% of the total collagen.

The contribution of proteoglycans to adult IVDs dry weight increases from about 10% to 20% in the outer regions of the AF to approximately 50% in the central regions of the NP. Multiple noncollagenous proteins within the matrix of the IVD appear to help organize and stabilize the matrix and influence cell function (Bayliss, 1990 #5).

3.2 LITERATURE REVIEW OF PREVIOUS ANIMAL MODELS OF IDD

There are two basic types of animal models of IDD: spontaneous disc degeneration and induced degeneration of normal healthy discs. The animal models of spontaneous disc degeneration include the sand rat, the pin tail mouse (Mason, 1984 #26) Chinese hamster (Silberberg, 1976 #42) and certain dogs and baboons (Hansen, 1951 #21) (Goggin, 1970 #43) (Ford, 1951 #16) (Lauerman, 1992 #22). For example, the sand rat develops spontaneous cysts and tears in the AF, degeneration of the facet joint, and herniation of the NP. This animal model of spontaneous disc degeneration has been the most extensively studied (Silberberg, 1979 #50) (Silberberg, 1988 #31) (Moskowitz, 1990 #28) (Adler, 1983 #3).

Models of induced degeneration have included disruption of the AF, facetectomy, repetitive electrical stimulation of muscles, and whole body vibration. Models that involve

disruption of the outer AF have been the most extensively studied and appear to produce a process that resembles human disc degeneration in rabbits, dogs, monkeys, sheep, pigs, and goats.

The earliest work dates to the 1930s, where Lob reported experimental anterior disruption of an animal disc. He noted that disc degeneration gradually developed after an anterior incision in the disc, similar to that which occurred in humans, based on radiographic and qualitative analysis. Filippi later added microscopic examination at various times after transversely sectioning the anterior portion of the AF.

Smith and Walmsley (Smith, 1951 #32) completed a similar study prompted by the superficial healing seen after posterior annulotomy in the dog disc (Key and Ford). They performed a 4mm long transverse ventral annulotomy through the AF and into the NP. The main findings were that (1) healing occurred in the outermost portion of the lesion, and (2) progressive degeneration occurred throughout the disc.

In 1980, Lipson and Muir (Lipson, 1981 #24) (Lipson, 1981 #25) (Lipson, 1980 #23) first applied biochemical analyses to this research. The classic "stab model" of Lipson and Muir is arguably the most widely known and well-characterized animal model of IDD currently available. A 2mm full-thickness, ventral stab of AF of rabbit lumbar discs by a number-11 scalpel blade appears to produce changes in certain biochemical and histological outcome measures that are similar to changes seen in human IDD. However, this model has some drawbacks for certain applications. Notably, the immediate herniation of NP upon full-thickness stab would appear to render this model less suitable for (A) studying the effects of less precipitous changes in NP and AF that may be important in the onset and progression of IDD, and (B) testing efficacy of novel therapeutic approaches that target the processes of early IDD.

3.3 MRI TUTORIAL

MRI has been established as an important diagnostic technique, most clearly showing diagnostic technique, most clearly showing its clinical utility and efficacy in the central nervous system, spine, and musculoskeletal system. In the spine and musculoskeletal system MRI has particular advantages and disadvantages.

The Advantages and Disadvantages of MRI
Advantages
High intrinsic soft tissue contrast and discrimination
Direct transverse, sagittal, coronal and oblique imaging
Multi-section imaging
No bone or air artefacts
Artefacts only from some metals
No ionizing radiation used
Demonstration of normal development and function
No known biological hazards
Disadvantages
Long scanning times
Many protocol options
Correct choice of rf pulse sequences parameters essential
Poor bone and calcium detail (including periosteal reaction)
Motion artefacts with scanning thorax and abdomen
Relative difficulty in monitoring/maintaining ill patients
Patients with pacemakers restricted
Claustrophobia (2%-5% cases studied)
High capital and revenue costs
Limited availability
? Long-term side effects

Figure 2. The Advantages and Disadvantages of MRI

3.3.1 Basics of MRI Physics

3.3.1.1 Magnetism

Magnetism is a property of matter that is a result of the orbiting electrons in atoms. The orbiting electrons cause the atoms to have a magnetic moment associated with an intrinsic angular momentum called 'spin'. When placed in a magnetic field of strength B, a particle with a net spin can absorb a photon, of frequency ν. The frequency depends on the gyromagnetic ratio, γ of the particle. For hydrogen, γ = 42.58 MHz / T (**$\nu = \gamma B$).** The hydrogen nuclei (protons) of the various tissues of the body become magnetized when a patient is placed within the powerful magnetic field. The orientation if this tissue net magnetization vector (NMV) will lie along the same direction as the external magnetic field B_o to which the tissue was exposed.

The degree to which the tissue is magnetized is dependent upon several factors. For example, the stronger the magnetic field B_o that the tissues are exposed to results in a greater degree of magnetization and a longer NMV. Also, the greater the number of protons per unit volume of tissue results in a greater amount of magnetization (per unit volume) from the tissue. Thus, two tissues exposed to the same magnetic field B_o may well differ in their initial magnetization magnitudes due to inherent differences in their relative proton densities. The tissue with the greater proton density (also known as spin density) will be more magnetized per unit volume of tissue, and will thus be depicted with a longer vector, than another tissue with fewer protons per unit volume. In summary, MR will be the creation, manipulation, and ultimate detection of tissue magnetization, the greater the relative proton density of the tissue the more this will contribute to that tissue's signal intensity, and the whiter it will appear on the image.

3.3.1.2 Resonance and RF

Protons in a magnetic field have a microscopic magnetization and act like tiny toy tops that wobble as they spin. The rate of the wobbling or precession is the *resonance* or Larmor frequency. In the magnetic field of an MRI scanner at room temperature, there is approximately the same number of proton nuclei aligned with the main magnetic field Bo as counter aligned. The aligned position is slightly favored, as the nucleus is at a lower energy in this position. For every one-million nuclei, there is about one extra aligned with the Bo field as opposed to the field. This results in a net or macroscopic magnetization pointing in the direction of the main magnetic field.

If the magnetized tissue is now exposed to a radiofrequency oscillating magnetic field that is oscillating at a precise, particular frequency, the result is an extremely efficient transfer of energy, or resonance, between the oscillating RF magnetic field transmitter and the tissue's protons. The grossly evident effect of such an energy transfer is a change in orientation of the tissue's NMV away from the vertical Z axis along which it was initially oriented. It is important to note that the brief RF pulses used in practical MR effectively change the direction, but not the magnitude / strength, of the tissue NMV.

On a macroscopic level, exposure of an object or person to RF radiation at the Larmor frequency, causes the net magnetization to spiral away from the Bo field. In the rotating frame of reference, the net magnetization vector rotate from a longitudinal position a distance proportional to the time length of the RF pulse. After a certain length of time, the net magnetization vector rotates 90 degrees and lies in the transverse or x-y plane. The receiver coils used in MRI to detect the magnetization brought down to the horizontal plane are oriented in such a way that they can only detect magnetic fields that are moving in the horizontal plane. It is in this position that the net magnetization can be detected on MRI.

3.3.1.3 Image Acquisition

Relaxation Times

The return of excited nuclei from the high energy state to the low energy or ground state is associated with loss of energy to the surrounding nuclei. T1 relaxation is characterized by the longitudinal return of the net magnetization to its ground state of maximum length in the direction of the main magnetic field. Thus, after turning off the 90 degree RF pulse the net magnetization vector (of each tissue) would immediately begin returning, or relaxing, toward the state that it had been in prior to disturbing it with the RF pulse (namely returning to the Z axis, parallel to the B_o static magnetic field). The rate of return is an exponential process as is shown in figure 3.

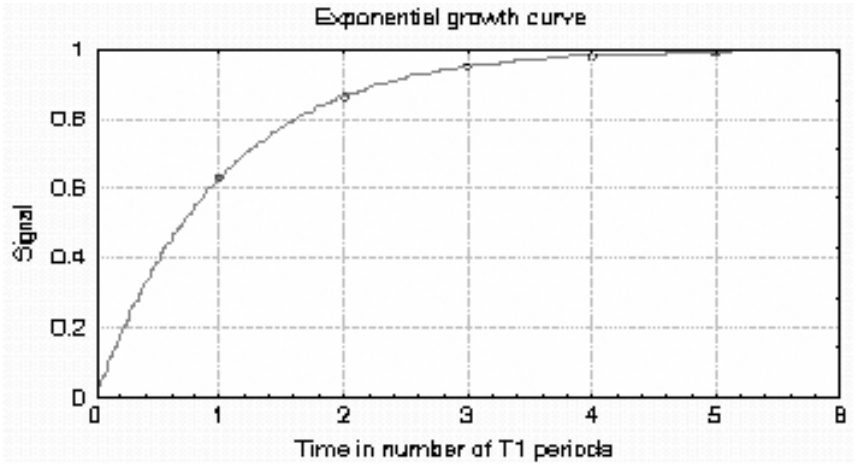

Figure 3. T1 relaxation rate is demonstrated. After two T1 times, the magnetization is at 86% of its original length. Three T1 times gives 95%. Spins are considered completely relaxed after 3-5 T1 times.

The rate at which this vertical magnetization recovers will differ from tissue to tissue. T1 value of a tissue is defined as the time after the 90 degree RF pulse that must pass before the tissue recovers 63% of its initial vertical magnetization.

Immediately following a 90 degree RF pulse , the magnetic moments of the individual nuclei comprising the tissue's net magnetization vector are no longer in a random orientation but rather are in phase together. This results in a detectable net magnetization vector, and yields a strong intensity for the receiver coils. Thus, the initial higher amplitude from each tissue will decrease over time until there is no horizontal tissue magnetization component (i.e., signal) detectable anymore. The rate at which the signal from the various tissues decays to zero is determined by the T2 value of that tissue, and is defined as the time after the 90 RF pulse that must pass before the tissue loses 63% of its initial horizontal magnetization (i.e., signal). T2 relaxation occurs exponentially like T1 relaxation with 63% of the transverse magnetization gone after one T2 period as shown in the following figure 4.

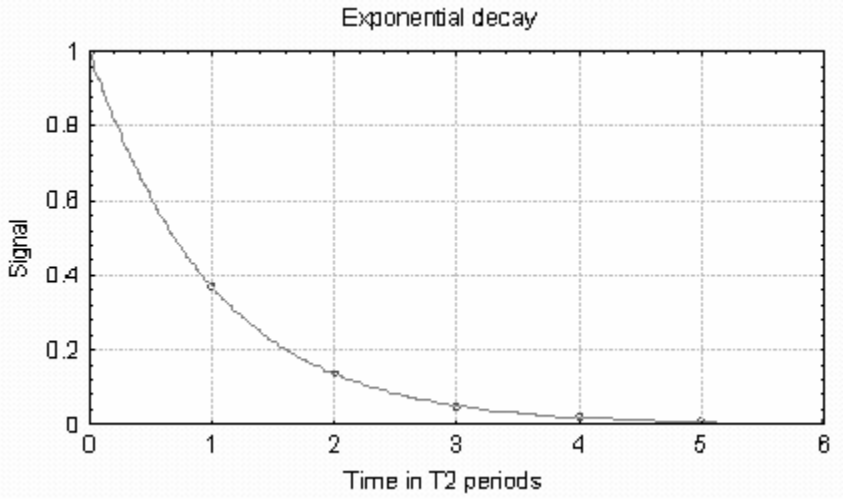

Figure 4. T2 relaxation rate is demonstrated. Note 63% of the transverse magnetization gone after one T2 period and approximately 100% gone after five T2 periods

Repetition Time (TR)

In order to measure how much of the vertical component of the NMV has recovered at any given time following a 90 degree RF pulse, the NMVs have to be flipped back into the horizontal plane by another RF pulse. Since a 90 degree RF pulse tips all vertical tissue magnetization into the

horizontal axis without changing its vector length, applying a second 90 degree RF pulse at a given time following the first enables the measurement of what has already been vertically recovered by that point in time when to the second 90 degree RF pulse is applied. The time interval between successive 90 degree RF pulses is referred to as he Repetition Time, or TR. It can be thought of as the amount of time that is allowed for recovery of the vertical magnetization of the tissues being studied.

Time To Echo (TE)

TE is another operator controlled parameter that dictates when to examine and measure how much horizontally oriented magnetization is present at the time for each tissue following an RF excitation pulse. It helps to think of the TE as the chosen time to examine how much signal (coherent horizontal magnetization) is still present for each tissue. This permits the user to take advantage of differing horizontal magnetization decay rates (i.e., T2) in order to attempt to measure horizontal NMV components form each tissue when they are most different.

K-Space in 2D

The digital MR signal is sampled and stored during data acquisition as a function of phase and time from an imaging sequence. Prior to image formation, is the production of information that fills k-space. K-space is the amount of space which must be filled with information that can be mathematically manipulated (Fourier Transform) in order to form an image. How it is filled can have an impact on the appearance of the image. K-space can also be defined as raw data – the intersection of one phase encoded axis and one frequency encoded axis (figure). It is where the

spatially- encoded MR signals collected during the application of the frequency encoding gradient are placed.

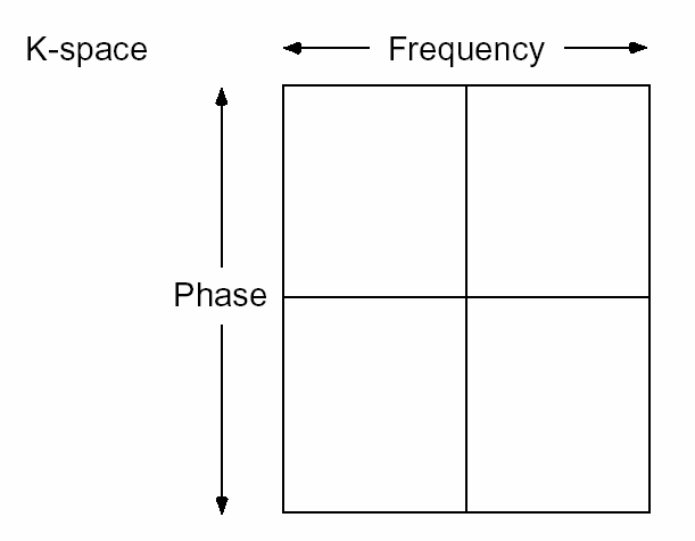

Figure 5. K-space showing phase and frequency directions

K-space itself does not directly relate to positions within the patient. In other words, the left side of k-space does not directly relate to the left side of the patient. Each data point, or sample, in k-space contributes to the entire image. These data points correlate to different magnetic field conditions imposed on the object being imaged.

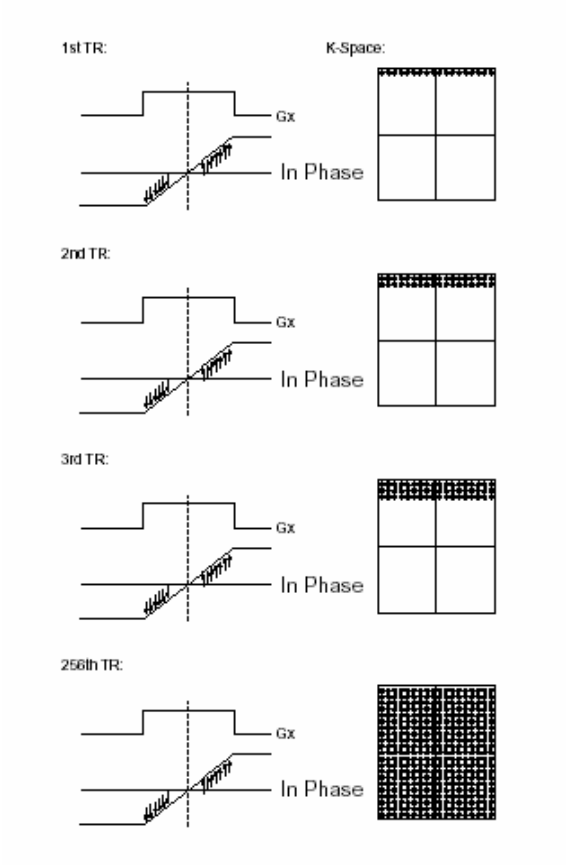

Figure 6. Demonstrates manner in which k-space is filled in.

FT is a mathematical procedure to separate out the frequency components of a signal from its amplitudes as a function of time, while the Inverse Fourier transformation (IFT) converts from the frequency domain to the time domain. In 2D FT, a line of data corresponds to the digitized MR signal at a particular phase encoding level. The data acquired for MR image reconstruction generally correspond to samples of k-space, that is, they represent values of the Fourier Transform of the image at a particular set of locations in k-space. Thus, FT is a mathematical process by which raw data or k-space is processed into a usable image.

3.3.1.4 Fast Spin Echo (FSE) Pulse Sequence

Fast Spin Echo (FSE) is a new fast scanning method that uses spin echoes and altered k-space filling.

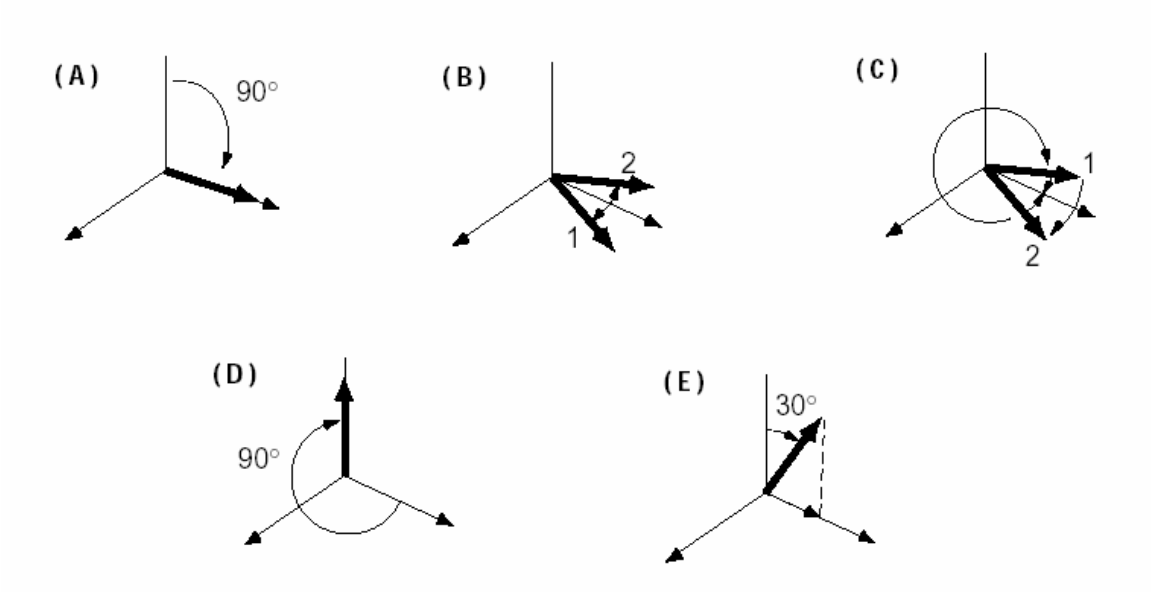

Figure 7. Fast Spin Echo sequence

It is designed to provide more conventional spin-echo-type contrast in shorter times (12 to 30 sec for a few slices). Fast Spin Echo (FSE) techniques produce long TR/long TE images in scan times that are approximately four to sixteen times shorter than those obtained via conventional spin echo techniques. FSE produces contrast that can be associated with a user-selectable TR and a user selectable average spin echo TE.

In conventional spin echo imaging, the phase encoding gradient is applied only once, even if two or four echoes are being generated. Each echo possesses the same phase encoding but, as each echo (TE1, TE2, TE3, TE4) is sampled, the sampled data contribute to a separate image. Figure 8 illustrates the spin echo sequence

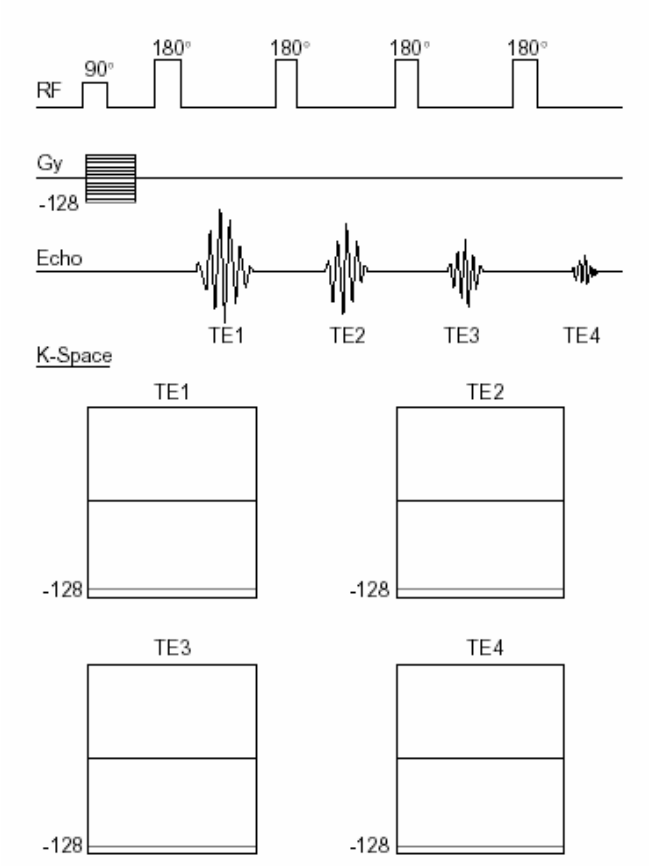

Figure 8. Spin Echo imaging sequence

For example, if a TR of 2000 ms, a 256x256 matrix, a TE of 15 ms, and four echoes were chosen, the result would be: at time TR the 90-degree pulse would be applied, phase encode gradient -128 would be applied and then four 180-degree pulses would be applied. Each of these would produce an echo and be accompanied by a readout gradient. Since only one line of k-space is filled at a time, the experiment is repeated 255 more times (256 lines/1 line-TR interval = 256 TR intervals). The associated scan time is 2 sec x 256 repetitions x 1 NEX = 8:53.

If, however, each echo were acquired with a different value of the phase encoding gradient, four lines of k-space would be filled for each TR interval. Figure 9 illustrates the fast spin echo sequence and k-space filling.

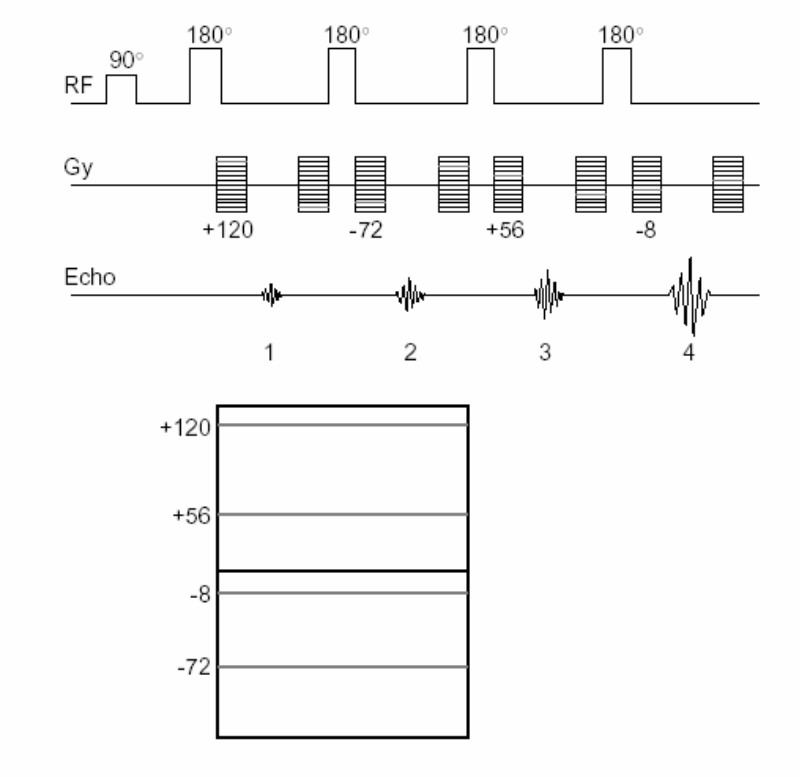

Figure 9. Fast spin echo sequence and k-space filling

In the FSE pulse sequence, the initial 90-degree pulse is followed by the acquisition of from 2 – 16 echoes. The number of echoes selected is called the *echo train length* (ET) and the time

TR would then have to be repeated only 64 times in order to fill k-space for a 256x256 scan (256 lines/4 lines-TR interval = 64 TR intervals). The associated scan time with this technique is 2 sec x 256/4 repetitions x 1 NEX = 2:13.

In the FSE pulse sequence, the initial 90-degree pulse is followed by the acquisition of from 2 – 16 echoes. The number of echoes selected is called the *echo train length* (ET) and the time

3.3.2 Instrumentation

Magnets

An essential component of an MRI system is a relatively stable and homogeneous static magnetic field. This is provided by one of three types of magnets designs – permanent, resistive, or superconducting. Each has its advantages and disadvantages (McFarland, 1986 #44). The single most costly item for a MR system is the magnet, and new and more compact designs are currently being developed.

Magnetic field strengths are measured in units of gauss (G) and Tesla (T). One Tesla is equal to 10,000 gauss. The earth's magnetic field is about 0.5 gauss. The strength of electromagnets used to pick up cars in junk yards is about the field strength of MRI machines (1.5-2.0T). You will run across four terms describing the magnetic properties of materials, such as contrast agents, used in MRI. These terms are ferromagnetism, paramagnetism, superparamagnetism, and diamagnetism.

Radiofrequency Coils

The basic radiofrequency (rf) coils are the "antenna" of the MR system that surrounds the part of the patient to be examined and broadcasts the rf signal to the patient and/or receive the return signal. RF coils can also be receive-only, in which case the body coil is used as a transmitter; or transmit and receive (transceiver). This produces the appropriate signal data from which digital images can be produced.

Surface coils are the simplest design of coil. They are simply a loop of wire, either circular or rectangular, that is placed over the region of interest. The depth of the image of a

surface coil is generally limited to about one radius. Surface coils (Figure 10) are commonly used for spines, shoulders, TMJ's, and other relatively small body parts.

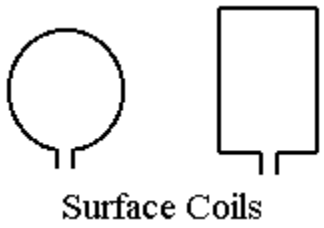

Figure 10. Linear surface coils. Round shaped surface coil (left), and license plate design (right).

Paired saddle coils (Figure 11) are commonly used for imaging of the knee. These coils provide better homogeneity of the RF in the area of interest and are used as volume coils, unlike surface coils. Paired saddle coils are also used for the x and y gradient coils. By running current in opposite directions in the two halves of the gradient coil, the magnetic field is made stronger near one and weaker near the other.

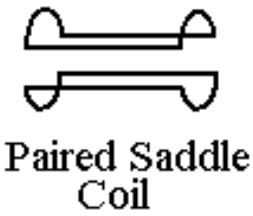

Figure 11. Paired Saddle Coil

The Helmholtz pair coils (Figure 12) consist of two circular coils parallel to each other and separated by a distance equal to their diameter. They are used as z gradient coils in MRI scanners. They are also used occasionally as RF coils for pelvis imaging and cervical spine imaging.

Helmholtz
Pair Coil

Figure 12. Helmholtz Pair Coil

The bird cage coil (Figure 13) provides the best RF homogeneity of all the RF coils. It has the appearance of a bird cage; hence, its name. This coil is commonly used as a transceiver coil for imaging of the head. This type of coil is also used occasionally for imaging of the extremities, such as the knees.

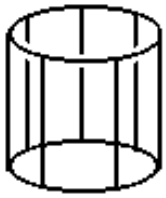

Bird Cage
Coil

Figure 13. Bird Cage Coil

The main magnetic field is modified during scanning for short periods (typically a few milliseconds) by the gradient magnetic fields. Gradient field strengths are usually only about 2% of the main field. Gradient coils are used to produce deliberate variations in the main magnetic field (Bo) and sections of tissue in any plane, as well as within the section, can be identified from the magnetized volume. There are usually three sets of gradient coils (X, Y, and Z), that are oriented in three orthogonal directions. The variation in the magnetic field permits localization

of image slices as well as phase encoding and frequency encoding. The set of gradient coils for the z axis are Helmholtz pairs, and for the x and y axes, paired saddle coils.

Electronics and Data Processing

These components are very similar to those employed in computed tomography (CT) and are required to collect and process the signal data to form images, which can then be displayed in digital form on a viewing console. Data acquisition times for conventional MRI are typically on the order of minutes, whereas data reconstruction takes only seconds. Digital data can be stored as in CT on magnetic tape, optical or floppy disc, or a hard copy can be created. The following schematic diagram describes the major components of a MRI scanner and setup.

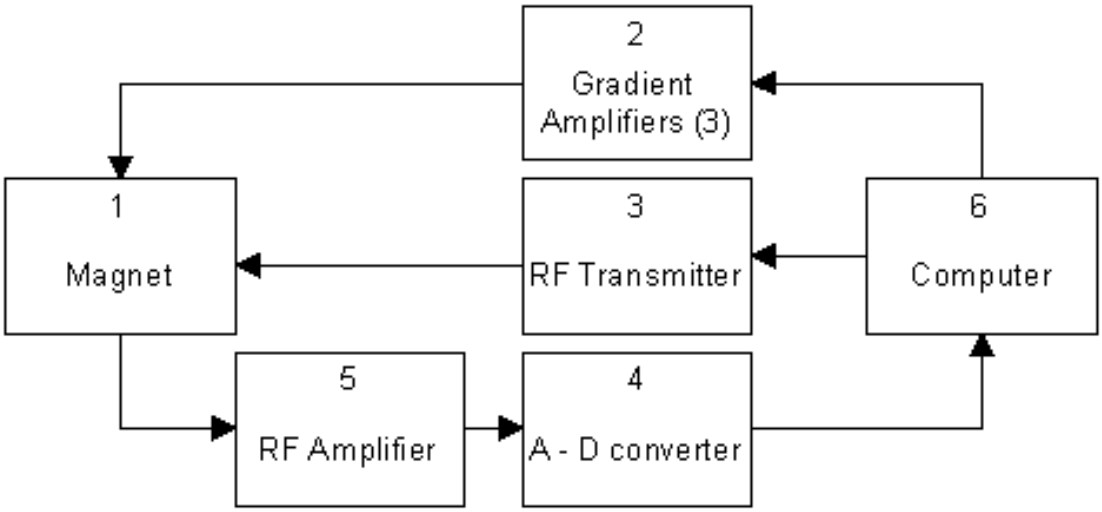

Figure 14. Schematic of the components required to collect and process signal data to form MR images

Focusing on the far right of the diagram is the computer that directs all of the action in the MRI acquisition, which acquires and processes the data. The computer dictates to the gradient amplifiers and RF transmitter when to turn on and off to obtain the proper pulse sequence. The RF receiver amplifier is also controlled by the computer and relays the signal

received by the RF coil from the patient to the A-D converter that digitizes the signal, and from there to the computer to be reconstructed into an image

3.3.3 MRI Safety

No genetic or mutagenic effects have been demonstrated using presently available MRI instrumentation (Budinger, 1981 #35). Although, there are potential sources of hazard that exist relating to the different types of magnetic fields encountered in MRI.

Static Main Magnetic Field Effects

There is no evidence to suggest any biological risk for those exposed to MRI from the static main field. The main concern is the attractive force on ferromagnetic objects which increases with field strength, and inversely with the distance from the magnet. Thus, loose ferromagnetic metal objects can become dangerous projectiles. Most orthopaedic implants are non-ferromagnetic or demonstrate a weak magnetic effect. Even if the clips or other implants are made from non-magnetic material, cold cutting during manufacture or bending can induce significant ferromagnetism within stainless steel (New, 1983 #36). A further practical problem concerns cardiac pacemakers, two types of which contain reed switches activated by magnetic fields. Deaths have occurred from trauma as a result of these effects. Finally, it is important to stress that the main magnetic field is not confined to the bore of the magnet, but extends for a significant distance in all directions.

Varying (Gradient) Magnetic Field Effects

Varying magnetic fields are imperative in order to obtain images in MRI. Rapidly changing magnetic field induces electric currents in tissues, which act as a conductor. It has been noted that skin sensations and muscular contractions would be induced before ventricular fibrillation because of the higher densities in these tissues (Saunders, 1984 #37)

In patients with metal in their body, the potential exists for electrical currents being induced in the metal with subsequent heating (Luechinger, 2004 #38). This may occur with metal foreign bodies or some surgical implants. Even tooth pain and taste sensation have been reported due to movement of the patient's head through a changing magnetic field, which indicates that patients should not be moved quickly when gradient fields are on.

Radiofrequency Magnetic Field Effects

The radio frequency power that is capable of being produced matches that of many small radio stations (15-20 kW). As a result there is the presence of heating effects from the RF (Armenean, 2004 #39). In most pulse sequences, the heating is insignificant and does not exceed the FDA guidelines. New pulse sequences such as for echo planar imaging and some spectroscopy localization techniques are capable of exceeding the FDA guidelines. Monitoring of the power deposition in patients is a requirement for FDA approval of clinical MRI scanners (Cline, 2004 #40). Potential for electrical shock exists with RF coils so proper grounding and insulation of coils is necessary. Any damage to coils or their cables needs prompt attention. Also looping of the cable to a coil can result in burns to patients that come into contact with them. It is best to avoid all contact with the RF coil cables

4.0 METHODS

4.1 PART 1: SOFTWARE: DEVELOPMENT OF A SLOWLY PROGRESSIVE AND REPRODUCIBLE ANIMAL MODEL OF IDD, CHARACTERIZED USING MRI.

4.1.1 Rabbit "Stab" Surgical Procedure

Each rabbit was tranquilized by IM injection of xylazine (3 mg/kg) and ketamine (40 mg/kg), and hair shaved from left flank and mid-back. Each rabbit was put under general anesthesia (inhalation anesthesia by 500 cc/min nitrous oxide and 2% isoflurane), and operative field prepped in sterile fashion with betadine. A longitudinal skin incision was made from the inferior margin of the rib cage to the pelvic rim, 2 cm ventral to the paraspinal musculature. The left anterolateral vertebral column from L1 to L6 was exposed by sharp and blunt dissection of the overlying subcutaneous tissue, retroperitoneal fat, and musculature. Disc levels were identified using the pelvic rim as an anatomic landmark for the L5-6 disc level. The L2-3, L3-4, and L4-5 lumbar intervertebral discs were stabbed by 16-gauge hypodermic needle (B-D PrecisionGlide® Needle, Becton Dickinson & Co., Franklin Lakes, NJ) to a depth of 5 mm in the left anterolateral annulus fibrosus.

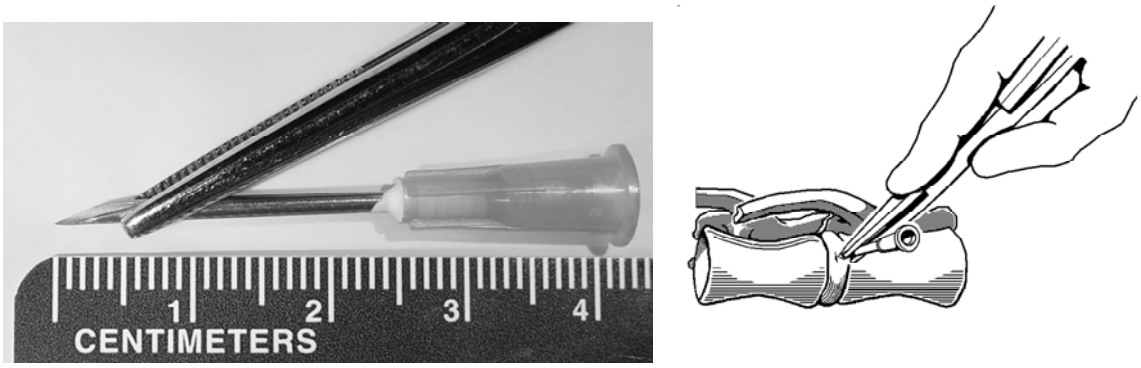

(A) **(B)**

Figure 15. Rabbit lumbar intervertebral discs were stabbed by 16-gauge hypodermic needle to depth of 5 mm in left anterolateral annulus fibrosus.

Depth of penetration was controlled by a locking forceps clamped 5 mm from the needle tip. The L1-2 and L5-6 discs were left undisturbed to serve as the superior and inferior intact control discs. After stab, the deep fascia, superficial fascia, and skin were closed in layers with absorbable sutures. Throughout all procedures, care was taken to not disturb the periosteal tissues of the vertebrae. Following surgery, the rabbits were permitted free cage activity (4000 cm^2), food, and water. At sacrifice, rabbits received an intramuscular injection of ketamine (25.0 mg/kg), followed by an intravenous injection of sodium pentobarbital (1.2 g/kg).

4.1.2 MRI Scanning Procedure

A total of 23 skeletally mature female New Zealand White rabbits (weighing approximately 4-5kg each and ranging in age from 1-2 years) were used in this study. The rabbits were followed serially by MRI for up to 24 weeks, with MRI scans taken pre-operatively, and at 3, 6, 12, and 24

weeks post-surgery. At each of these time points, 3 rabbits chosen at random were also x-rayed. Two to three rabbits were sacrificed for histology at each time point. (A limited number of rabbits were also sacrificed at selected time points to provide disc specimens for Real-Time quantitative PCR gene expression assays. Histology and RT-PCR data are not reported here.)

MRI scans were obtained using a 5 inch surface coil connected to a 1.5 Tesla clinical magnet, shown in Figure 16 (Signa Horizon LX, General Electric Medical Systems) furnished with GE Signa Level 9.0 ASP2 Software.

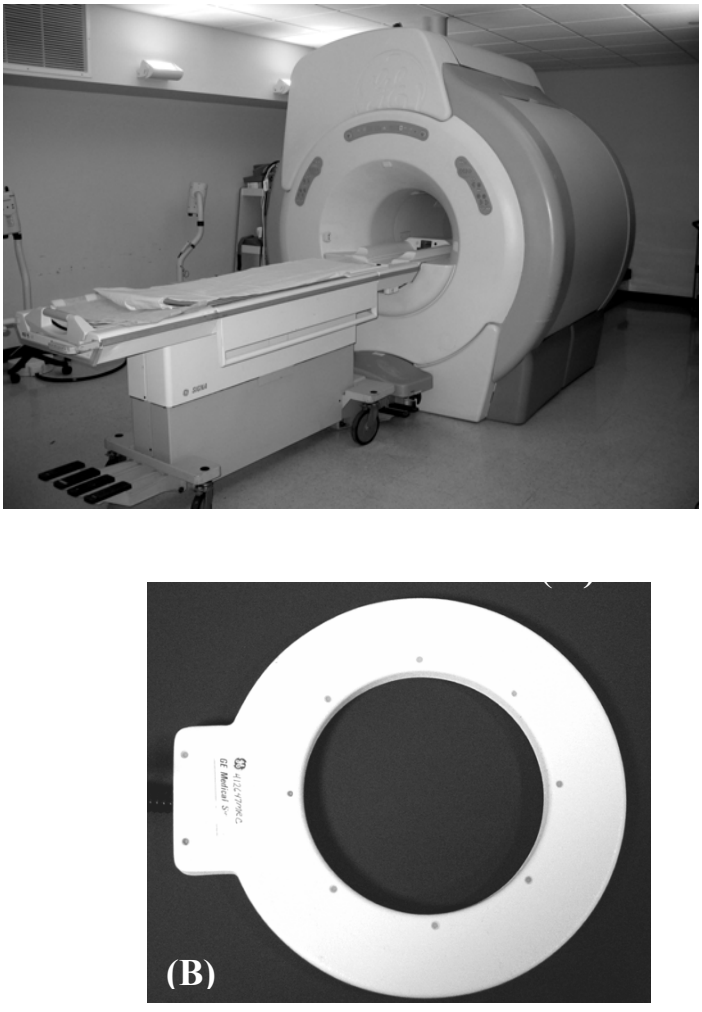

Figure 16. (A). 1.5T clinical magnet, (B) 5 inch surface coil

Rabbits were tranquilized by IM injection of xylazine (3 mg/kg) and ketamine (40 mg/kg) and placed supine within the magnet, with lumbar region centered over a 5-inch diameter circular surface coil (General Electric Medical Systems).

MRI Scanning Parameters at 1.5T

First, a sagittal localizer (TR 300ms, TE 37ms) was obtained along with a coronal localizer image (TR 1445ms, TE 37ms) to establish the position of the lumbar discs from L1-2 to L5-6. Then, a 3-mm thick mid-sagittal section (12 x 9 cm field of view, 256 x 192 matrix size) was imaged, using a T2-weighted imaging sequence (TR 3500 ms, TE 103 ms) to highlight the signal from the nucleus pulposus. T2-weighted axial images (TR 3500 ms, TE 100 ms) and T1-weighted mid-sagittal images (TR 400ms, TE 12ms) were also obtained (data not shown here). Figure 17 contains the scanning parameters used with the 5 inch surface coil at 1.5T.

	MRI Scanning Parameters: 5 inch Surface Coil (1.5T)					
	TR(ms)	TE(ms)	Acq . Matrix	FOV (cm)	Slice Thickness (mm)	Mode
T1 Sagittal Localizer	300	37	256 x 128	20	3 skip 1	2D
T2 Coronal Localizer	1445	37	256 x 128	20	3 skip 1	2D
T2 Sagittal	3500	103	256 x192	18	3 skip 0.5	2D

	MRI Scanning Parameters: 5 inch Surface Coil (1.5T)					
	ETL	Bw	Freq. Dir.	Phase FOV (cm)	NEX	Imaging Options
T1 Sagittal Localizer		15.83	S/I	1	1	
T2 Coronal Localizer		15.83	S/I	1	1	
T2 Sagittal	12	20.63	S/I	0.75	4	FC, ED,TRF, NP, FSE

Figure 17. MRI scanning parameters used for 5 inch surface coil at 1.5T

4.1.3 MRI Image Analysis Using PACS Clinical Software

The Dicom-formatted image data (Dicom 3.0) were transferred to a PACS (Picture Archiving and Communications System) furnished with Agfa IMPAX 3.5 Software, v2.6 (Bayer Corporation. Figure 18 illustrates the manner and format in which the images were transferred from the MR scanner to the PACS workstation for analysis.

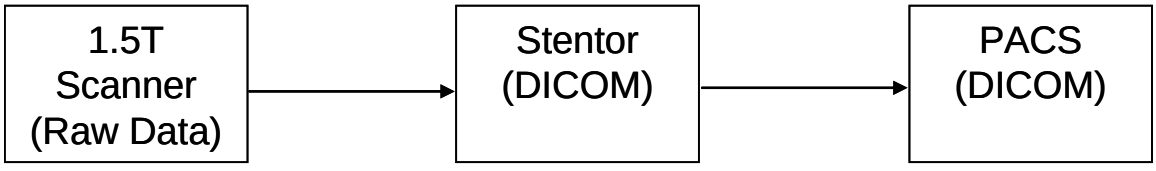

Figure 18. Illustrates the process of transferring of MR images from MR scanner to PACS workstation

4.1.3.1 ROI Measurement of NP using PACS

The T2-weighted mid-sagittal images of the intact and stabbed discs were analyzed qualitatively for evidence of degenerative changes. Region of Interest (ROI) measurements of the NP where obtained and quantitative analysis of these images was completed using the PACS as follows (Sobajima, 2005 #51). The nucleus pulposus of each disc was outlined on-screen using the computer mouse to define the region of interest (ROI), shown in figure 19.

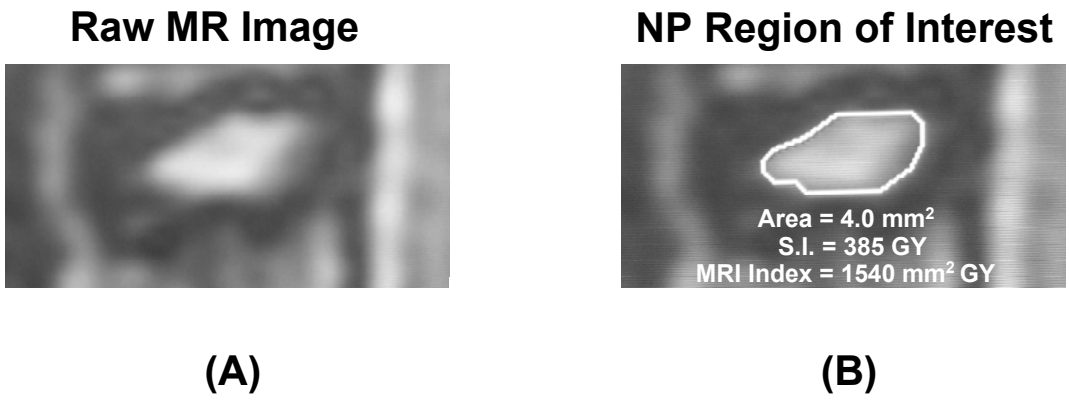

Figure 19. Computer screen captures showing T2 weighted MRI of healthy, intact rabbit lumbar disc (A) and the same image with NP outlined to define ROI.

The area and average signal intensity (Gray Scale value) of this ROI were then computed automatically by the IMPAX software, and the data downloaded to a computer spreadsheet (Microsoft® Excel 2000) for analysis.

4.1.3.2 Quantitative Analysis of MRI Images Using PACS

MRI Index

Understanding that MR images of a nucleus pulposus of a degenerating disc potentially could demonstrate changes in area, signal intensity, or both, an additional MRI outcome measure

"MRI Index" (the product of nucleus pulposus area and average signal intensity) was computed. This allowed for a more comprehensive measure of degenerative changes apparent in the NP.

The MRI data of each disc at 3, 6, 12, and 24 weeks post-surgery were normalized to that disc's corresponding pre-operative data (and expressed as "% of Pre-op"). For each disc level, mean and standard deviation of the pre- and post-operative nucleus pulposus area, average signal intensity, and MRI Index were computed at each time point, and General Linear Modeling techniques were applied to test for differences between the means (significance set at $p < .05$). In addition, at each time point the MRI Index data of the stabbed discs (L2-3, L3-4, and L4-5) were grouped and compared with the corresponding grouped data of the intact control discs (L1-2, L5-6) to assess the effects of stab without regard to disc level.

95% Confidence Interval

Mean MRI Index (and 95% confidence interval for the mean) was computed at each time point, and linear regression performed to determine rates of change of MRI Index with time.

Number of Discs Exhibiting Degeneration

Finally, the MRI Index data of the stabbed disc group were analyzed to determine the percentages of stabbed discs at 3, 6, 12, and 24 weeks exhibiting at least a 15, 30, or 45% decrease in MRI Index with respect to pre-operative MRI Index. This was done to determine whether this model of IDD resulted in progressive "recruitment" of stabbed discs exhibiting certain thresholds of MRI Index decrease, or, on the other hand, spontaneous recovery or reversal of MRI changes.

4.1.4 MRI Image Analysis Using AMIRA 3.0 Imaging Software

The DICOM formatted image data (DICOM 3.0) were transferred to the AGFA workstation as described in section 4.1.3. The DICOM images were then transferred to a public FTP server and downloaded to a PC containing AMIRA software. Figure 19 is a flow chart demonstrating the manner and format in which the MRIs were transferred from the scanner to the PC containing the AMIRA 3.0 software.

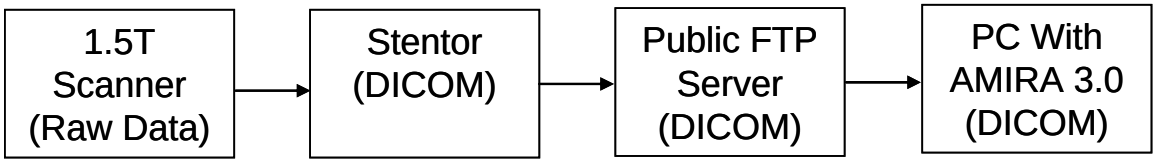

Figure 20. Describes the data transfer method from the MR scanner to the AMIRA workstation

4.1.4.1 ROI Measurement NP using AMIRA 3.0

The T2-weighted mid-sagittal images of the intact and stabbed discs were analyzed qualitatively for evidence of degenerative changes. ROI measurements of the NP where obtained and quantitative analysis of these images were completed using the AMIRA as follows.

AMIRA 3.0 allows higher magnification of a digital image such that each pixel and its corresponding signal intensity can be viewed, whereas the AGFA station does not permit this high magnification. Moreover, the AGFA software is used more for clinical and qualitative assessment, while AMIRA warrants a more scientific approach to obtain the NP area. The NP of control and stabbed discs were magnified such that each pixel of the disc was visible on screen. The NP of each disc was outlined on-screen using the computer mouse to define the region of interest (ROI). The area and average signal intensity of this ROI were then computed by the

AMIRA software, and the data compiled in a Microsoft excel spreadsheet for analysis. Figure 21 illustrates an AMIRA screen capture and measurement.

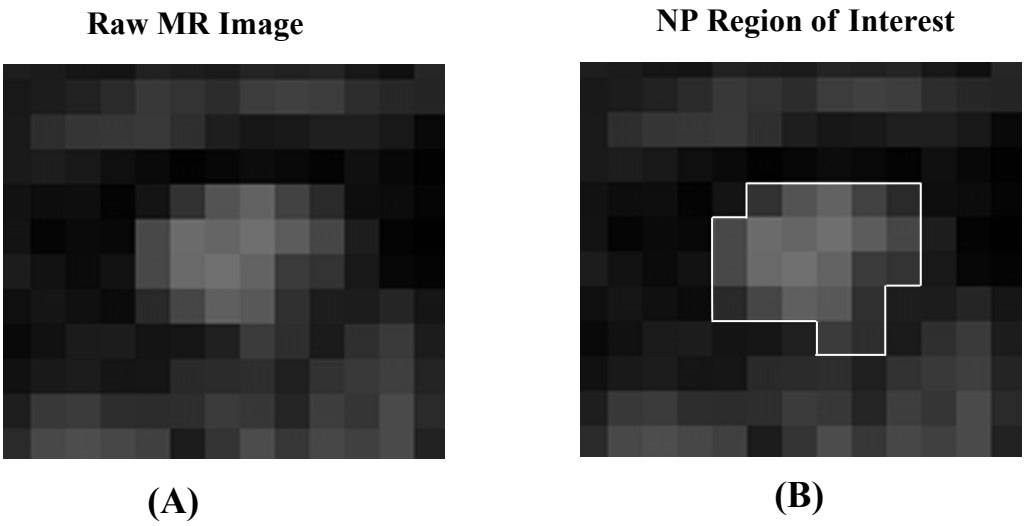

Figure 21. AMIRA screen captures showing T2-weighted MRI of a representative healthy, intact rabbit lumbar disc (A), and the same image with NP outlined to define ROI (B).

4.1.4.2 Quantitative Analysis of MRI Images Using AMIRA 3.0

MRI Index, 95% confidence interval, and number of discs exhibiting degeneration were then calculated for control (L1/2, L5/6) and stabbed discs (L2/3, L3/4, L4/5) as described in section 4.1.3.2.

4.1.5 MRI Intra- and Inter-Observer Repeatability

Four rabbits at 12 weeks post-stab were scanned twice using the scanning parameters described in section 4.1.2. T2-weighted mid-sagittal images were obtained, and the resulting data were analyzed by two independent observers in a blinded fashion (as seen in section 4.1.3). These rabbits were completely removed from the magnet and then re-positioned onto the magnet bed

following each scan. Intra-class Correlation Coefficients (ICCs) were calculated to determine intra- and inter-observer repeatability of the MRI measurements.

4.1.6 Natural Course

A total of 4 skeletally mature female NZW rabbits were used in this study. The rabbits discs (L1/2-L5/6) were left intact (no stab surgey), and were followed serially by MRI. T2-weighted mid-sagittal scans were taken at time 0, 12, and 24 weeks with scanning parameters described in Section 4.1.2. ROI measurements of the NP (section 4.1.3.1), MRI Index, and 95% confidence intervals (section 4.1.3.2) of these images were completed using PACS.

4.2 PART 2: HARDWARE: : DEVELOPMENT OF 3.0T MRI QUAD COIL FOR IMAGING RABBIT SPINE

4.2.1 Tests of Existing Clinically Available MR Coils

Experiments were completed with the following commercially available coils: 5inch surface, 3inch surface, head, body, and license plate coils at 1.5T; and body and head coils at 3.0T. Figure shows the coils used in the study.

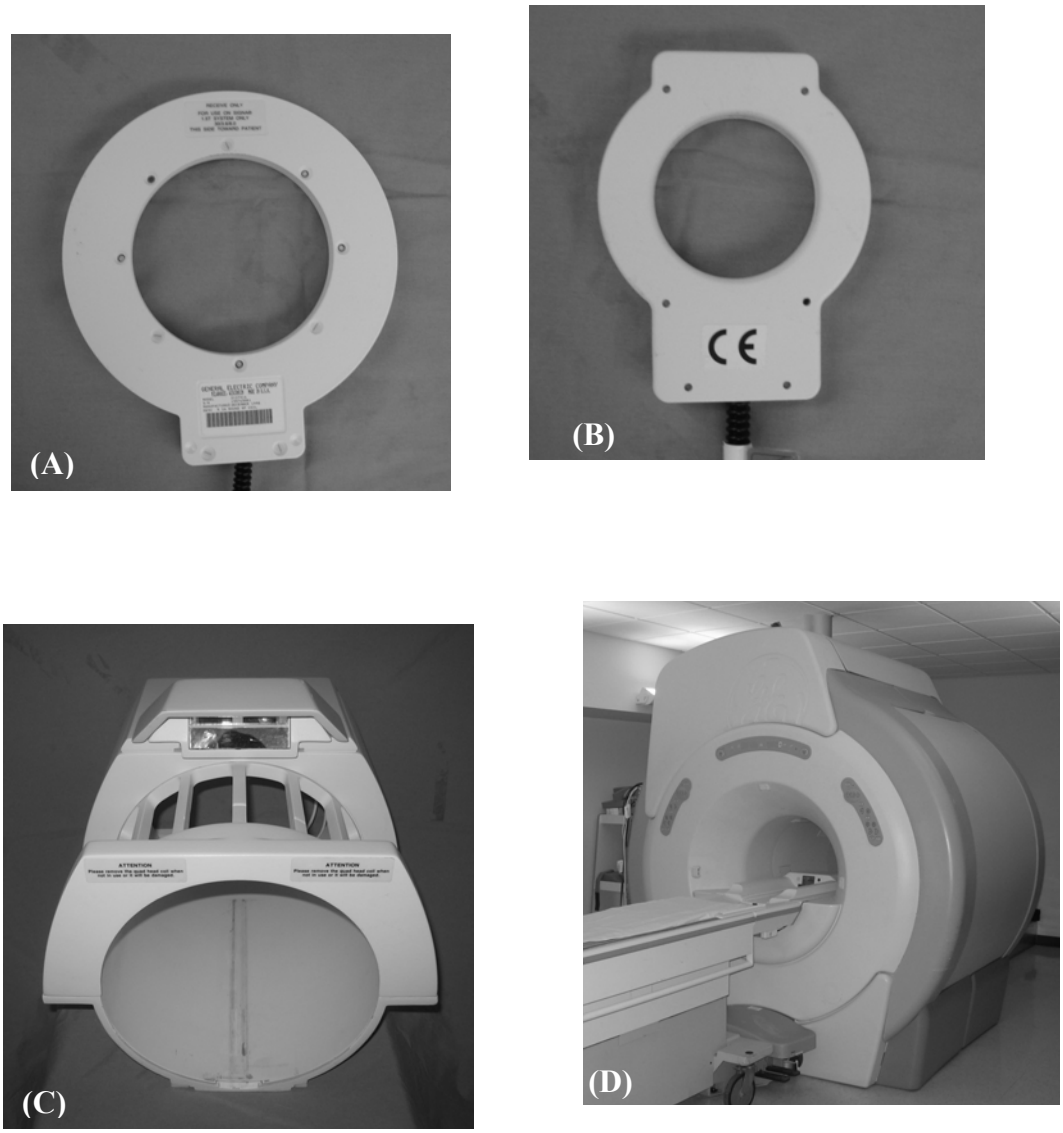

Figure 22. (A) 5 inch surface coil, (B) 3 inch surface coil, (C) head coil, and (D) body coil

T2-weighted sagittal scans, as described in section 4.1.7 were obtained using one NZW rabbit. Signal to Noise Ratio (SNR) was used as an outcome measure to determine the performance of the commercially available coils. The in-vivo SNR will be measured by dividing the mean of the signal from a circular ROI placed inside the NP by the standard deviation of a ROI placed in the noise background of the image. These results will be compared to SNR measurements of the custom quad coil at 3.0T (described later in thesis).

4.2.2 X-Ray Study: Location of Rabbit Spine with 1.5T Scanning Method

The purpose of the study was to determine the position of the rabbit spine in reference to the 5 inch surface coil. MRI study (described later in thesis) will be completed with a MR phantom (CuSO4) positioned at the distance from the 5 inch coil that was measured on the rabbit x-ray. The goal will be to compare the performance of the commercially available 5 inch surface coil to a custom built quad coil at 3.0T, when a phantom is positioned at the location of the rabbit spine.

4.2.2.1 Calibration

A combination of a wooden plate and foam padding was used to reproduce the scanning method used with the 5 inch surface coil at 1.5T. A k-wire (2mm steel rod) was placed on the foam padding and used as a reference on the x-ray. A 2.5 inch diameter steel calibration cylinder was placed on the foam padding, and lateral plain x-rays were taken using a Shimadzu x-ray machine (model 5D150L, Shimadzu Corporation, Kyoto, Japan), with a collimator-to-film distance of 60cm, exposure of 100mAs, and a penetration power of 48 kVp. The radiographs where taken as a calibration method to account for magnification. The following figure shows x-ray setup with calibration cylinder.

Figure 23. Picture of x-ray setup with calibration cylinder

4.2.2.2 Location of Rabbit Spine

A New Zealand White rabbit was then positioned on the foam padding and supported with towels, which were used to secure the position of the rabbits during the MRI scanning procedure described in section 4.1.2. Lateral plain radiographs where completed using one NZW rabbit with parameters described in section 4.2.2.1. The distance from the k-wire to the most anterior portion of the lumbar IVDs was measured, along with the distance from the anterior to posterior ends of the IVD.

4.2.3 X-Ray Study: Location of Rabbit Spine with 3.0T Scanning Method

The purpose of the study will be to determine the position of the anesthesized rabbit spine as the animal is positioned in a trough, with dimensions that will resemble the custom quad coil. The

performance of quad coil will then be tested with a MR phantom positioned at the location of the rabbit spine.

4.2.3.1 Development of Wood Trough

A wooden trough was constructed to resemble the geometry of the 3.0T quad coil. This design would allow for accurate positioning of the anesthesized rabbit during scanning. The goal was to determine the location of the rabbit spine as the rabbit is positioned in the quad coil. The frame was made of wood with a plastic v shaped insert. The plastic insert will be used to connect the plexiglass frame of the prototype quad coil.

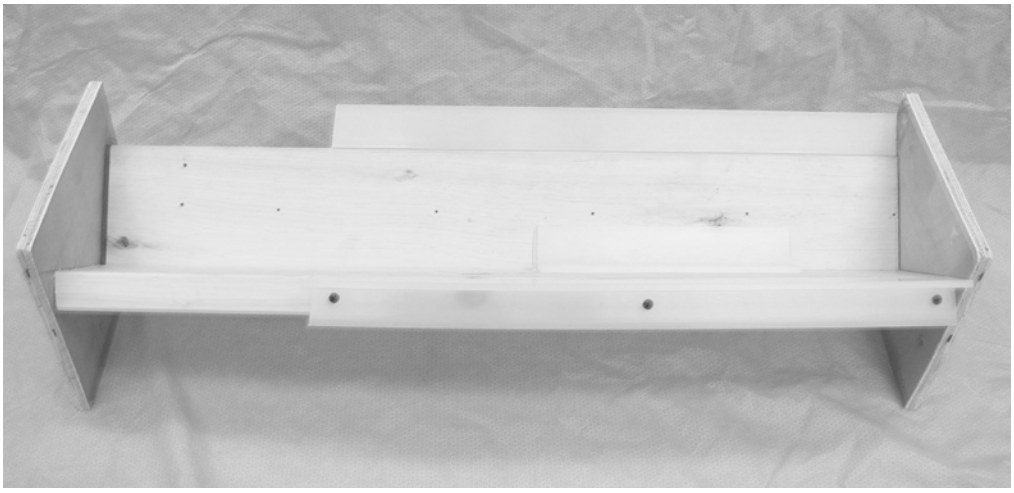

Figure 24. Picture of wood trough with plastic insert.

4.2.3.2 Calibration

First, a k-wire was placed on the wood trough under the plastic insert. Then another k-wire was positioned on the plastic insert. A 2.5 inch diameter steel calibration cylinder was then centered on the plastic insert. Lateral plain radiographs where taken using the method described

in section 4.2.2.1. The radiographs where taken as a calibration method to account for magnification.

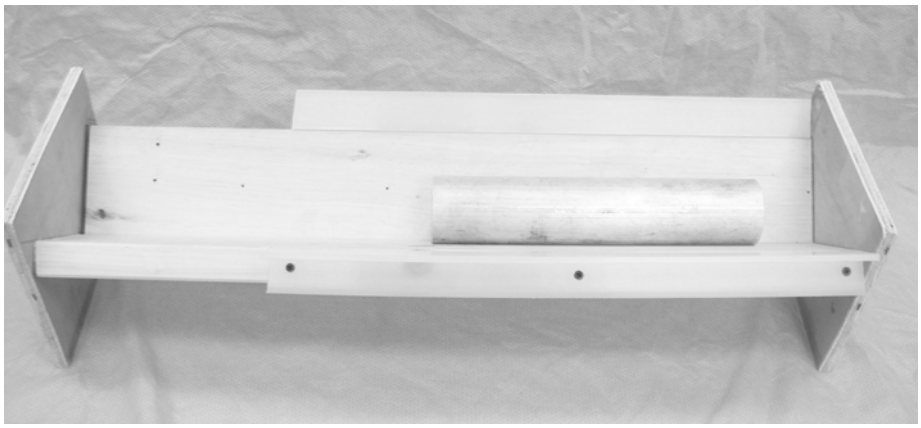

Figure 25 . Picture of wood trough with calibration cylinder

4.2.3.3 Location of Rabbit Spine

The calibration cylinder was removed and an anesthesied NZW rabbit was positioned on the wood trough. Lateral plain radiographs were taken as described in section 4.2.2.2. The distance from the k-wire (on the plastic insert) to the most anterior portion of the lumbar IVDs was measured. Also measured was the distance from the anterior to posterior ends of the IVD.

4.2.4 Quad Coil Design For 3.0T Spine Imaging

The objective was to design a quad coil at 3.0T with geometry optimized for the rabbit lumbar spine that would permit adequate FOV imaging with a higher SNR than that achievable with existing commercially available coils. The quad coil prototype will consist of two coil elements built on a plexiglass frame. Plexiglass end caps will be used to add stability to the coil

for long term use. A basic criterion for optimizing signal reception was to tailor the region of sensitivity of the coil to the desired FOV. To provide improved sensitivity in the region of interest (ROI), it was required to fit the coil to the rabbit spine as tight as possible without compromising the coil circuit electronics. In addition, the coil will be made large enough to accommodate various size rabbits.

A quad coil with optimized geometry for rabbit spine imaging could now be created after exhaustive testing of commercially available coils and x-ray studies to determine the location of the spine as the anesthesized rabbit lay in an X coil design. A design was selected such that each coil element had a 5 inch radius and 9.5 inch length. Thus, the overall length of the coil is 9.5 inches, enabling a FOV of 9.5 inches. An electrical schematic of a quad coil element and constructed custom quad coil are shown in figure. 26

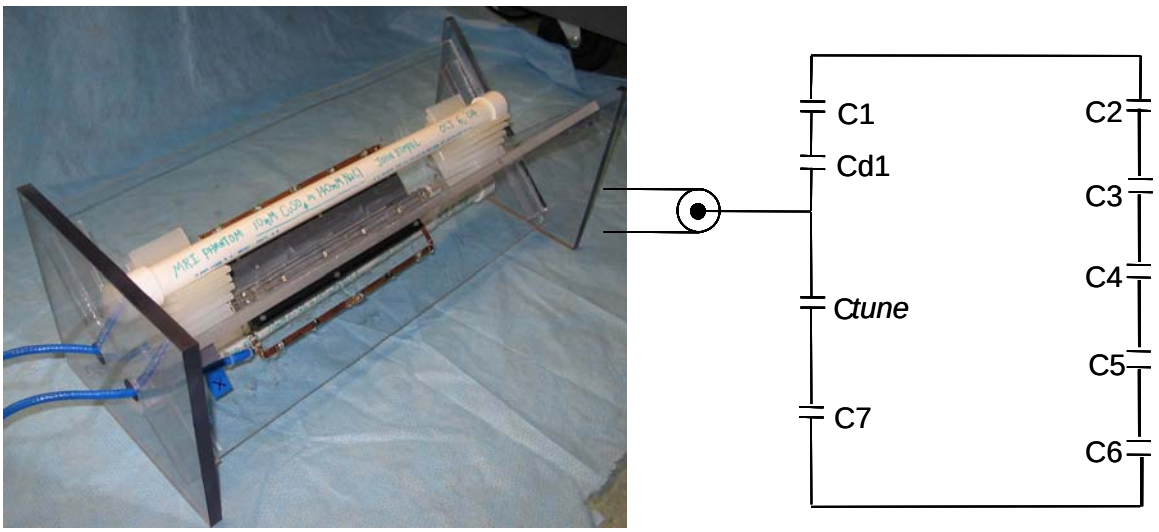

Figure 26. Picture of custom quad coil (A), and electric schematic of one coil element (B).

Coil elements were constructed with 5 distributed capacitors 24 pF (100B series, American Technical Ceramics, Huntington Station, NY) to minimize electric fields, thus reducing the effect of the rabbit load on the resonant frequency and other associated losses. A variable capacitor 1-25 pF (NMA series, Voltronics, Denville, NJ), C_{tune} was placed in series to allow tuning to a resonant frequency of 127.74 MHz (3.0T). The matching capacitor 47 pF, C_{d1}, transformed the real impedance of the coil to within 10% of 50 Ω while a 5 kg rabbit was placed on the coil. The Isolation value for the coil was -8.

4.2.5 Quality (Q) Factor Measurement

The quality factor (Q) of each coil element will be measured on a Hewlett-Packard network analyzer model 8753C. To replicate the manner in which a rabbit would load the quad coil; 1 liter bags will be filled with CuSO4 and loaded on the coil one at a time until a 6kg load is achieved. Figure 27 shows the custom quad coil connected to the network analyzer (A) and also with 1 liter CuSO4 bags totaling 6kg (B).

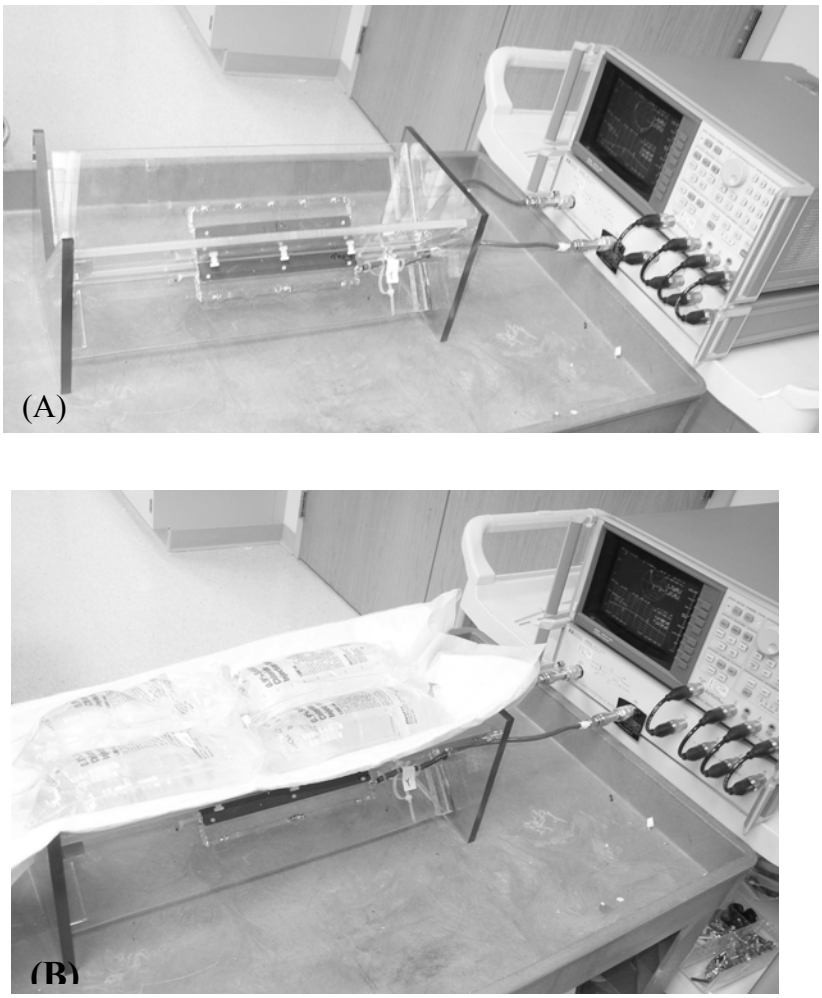

Figure 27. (A) quad coil connected to network analyzer, (B) quad coil with CuSo4 bags

The Q Factor was measured on a Smith Chart by obtaining the center frequency (f) and dividing it by the cutoff frequencies (Δf). The following equation was used to comple the Q factor measurements.

$$Q = \frac{\mathbf{f\ (Center\ Frequency)}}{\mathbf{\Delta f\ (Cutoff\ Frequencies)}}$$

This value was calculated for each 1kg increment load. A plot of Q Factor vs. load (kg) was then generated.

4.2.6 Preliminary Development of Reference Phantom For Quad Coil at 3.0T

The 1.5T clinical scanner was used to obtain preliminary data for the reference phantom to be used with the custom quad coil (the 1.5T scanner was more accessible than the 3.0T scanner, which was the reason for completing this study on 1.5T magnet). The design of the quad coil will allow strategic positioning of a reference phantom below the rabbit. This phantom will be positioned in the desired FOV and will be used to normalize the signal values obtained.

Based on the x-rays obtained in section 4.2.3, a 3/8inch diameter tube was selected for the phantom. Preliminary scans were obtained with the phantom to determine if signal could be detected in a tube of this size. The phantom was positioned over the 5 inch coil (Figure 28) and T2-weighted sagittal scans were achieved as described in section 4.1.2.

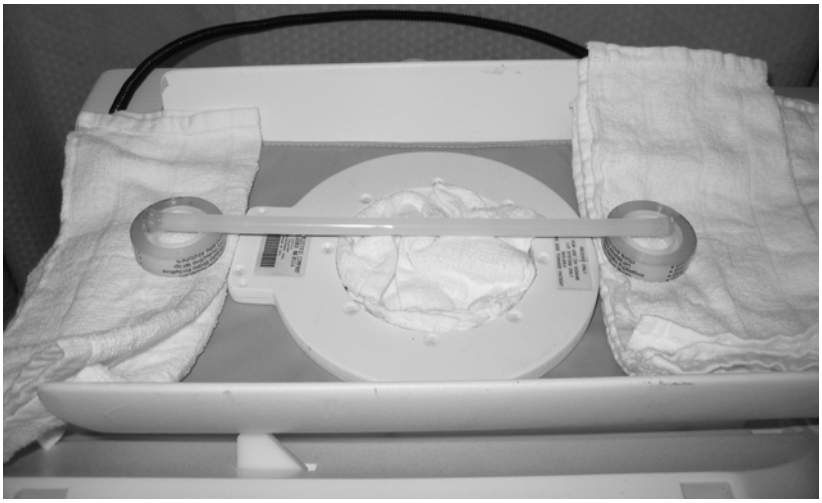

Figure 28. 3/8 inch tube MRI phantom positioned over the 5 inch surface coil

A cardboard trough was then constructed to determine the position of the rabbit in the quad coil with the phantom and "water bed" placed underneath the rabbit. Two condoms filled with saline were used as the "water bed" placed between the phantom and the rabbit (Figure 29). The

"water bed" was used to eliminate air space between the rabbit and phantom. A NZW rabbit was then placed on the cardboard trough equipped with reference phantom. T2-weighted sagittal and axial scans were obtained as described in section 4.1.2.

Figure 29. Wood trough with reference phantom

4.2.7 MRI Comparisons – 3.0T vs. 1.5T

Validation of the custom quad coil was completed with phantom and in-vivo rabbit images. When the quad coil was operating at its potential, experiments where completed to demonstrate its improvements. The 5 inch surface coil at 1.5T (used in part 1 of thesis) was compared to the custom quad coil through the following experiments.

4.2.7.1 Phantom Comparisons – 3.0T vs. 1.5T

A 1in. OD and ¾ ID PVC tube was filled with 10mM $CuSO_4$ and 140 mM NaCl was used as the phantom as seen in figure 30.

Figure 30 1 inch diameter CuSO4 phantom used to validate performance of 5 inch and custom quad coils.

This size tube was chosen after acquiring the x-ray results, which was approximately the size of the rabbit spine.

1.5T Setup Method

The CuSO4 phantom will be positioned at the location of the spine, also based on the x-ray results obtained in section 4.2.2. Figure 31 illustrates the setup of the phantom positioned in the quad coil FOV.

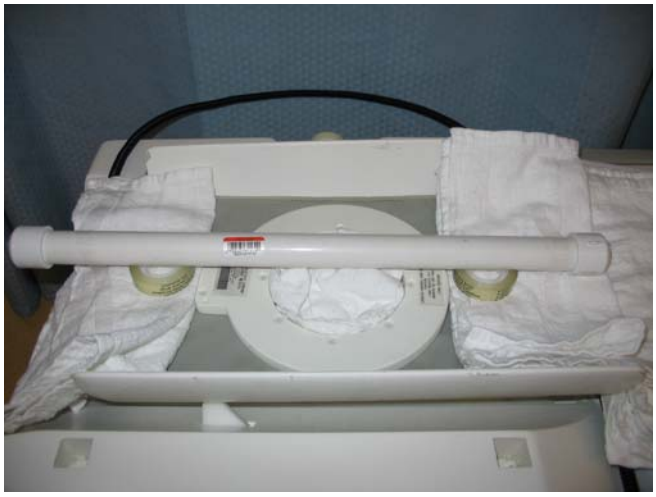

Figure 31. Experiment setup for validation of 5 inch coil. A 1 inch OD CuSO4 phantom was positioned over the 5 inch coil

3T Setup Method

The $CuSO_4$ phantom will be positioned at the location of the rabbit spine based on the x-ray results in section 4.2.3. Figure 32 illustrates the setup of the phantom positioned in the quad coil FOV.

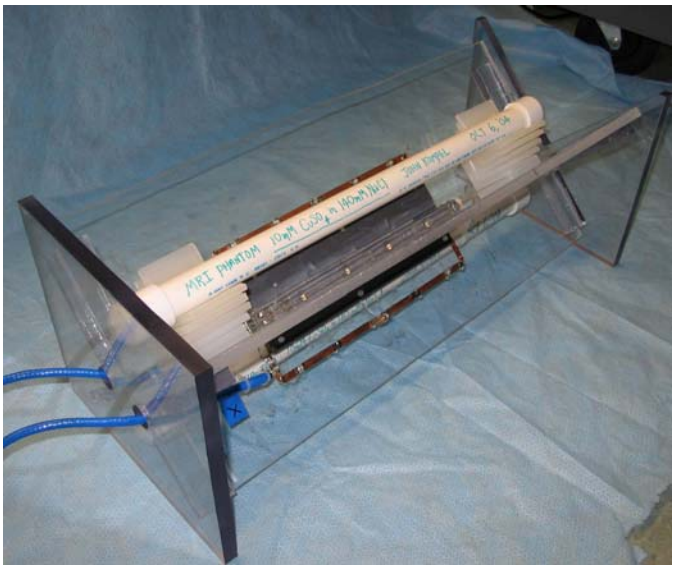

Figure 32. Custom quad coil with phantom positioned at the location of the rabbit spine. This location was based on results obtain through x-ray studies.

Sagittal and coronal localizers, and T2-weighted FSE sagittal images will be obtained with the 5 inch surface coil and custom quad coil using the parameters described in section 4.1.2. Images will be acquired using a 20cm and 30cm FOV to prove the true range of the two coils. Signal as a function of longitudinal position (20cm and 30cm FOVs) will be determined by averaging the signal of each pixel along the major axis of the phantom. The noise level will be determined by computing the standard deviation of a large ROI placed in the noise background of the image. Using these data, the SNR profile will be determined.

4.2.7.2 In-vivo Rabbit Comparisons – 3.0T vs. 1.5T – 256x256 matrix size

In addition to the in-vitro data, in-vivo images will be obtained with the 5 inch surface coil and custom quad coil from one healthy NZW rabbit. Sagittal and coronal localizer, and T2-weighted FSE sagittal images will be obtained using the parameters described in section 4.1.2. The in-vivo SNR will be determined by dividing the mean of the signal from a ROI placed in the NP region of the IVD divided by the standard deviation of a large ROI placed in the noise background of the image. Moreover, the SNR profile will be determined in the reference phantom of the 3.0T image (as described in section 4.2.7.1), to further emphasize the uniform signal produced by the custom quad coil.

4.2.7.3 Rabbit High Resolution Image at 3.0T vs. 1.5T Image

In-vivo images will be obtained with the 5 inch surface coil and custom quad coil from one healthy NZW rabbit. A 512x512 matrix size image with the custom quad coil will be compared to 256x256 matrix size acquired with the 5 inch surface coil. For direct comparison all other scanning parameters will be held constant. The in-vivo SNR will be determined as described in section 4.2.7.2.

5.0 RESULTS

5.1 PART 1: SOFTWARE: CLINICAL MRI ANALYSIS OF RABBIT MODEL OF IDD

5.1.1 Rabbit "Stab" Surgical Procedure

Two rabbits died during surgery as a result of technical problems in the administration of the anesthesia. The remaining 18 rabbits tolerated the surgery well, with no post-operative behavioral or neurological symptoms. During surgery, immediate herniation of nucleus pulposus (NP) upon stab was observed in only 1 out of the 54 stabbed discs.

5.1.2 Qualitative MRI Findings of Longitudinal MRI 'Stab" Model of IDD

Representative serial MRI scans of the lumbar spine of one rabbit are shown in Figure. consisting of T2-weighted, mid-sagittal plane images obtained pre-operatively, and 3, 6, 12, and 24 weeks after stab of the L2-3, L3-4, and L4-5 discs.

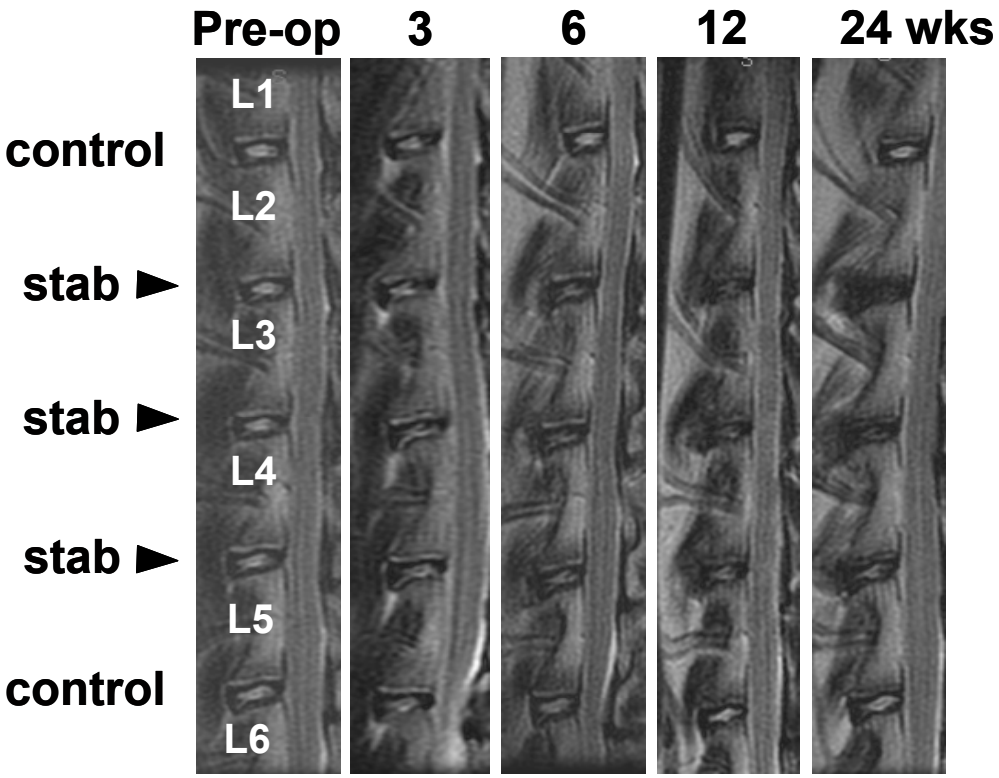

Figure 33. Representative serial MRI scans of lumbar spine of one rabbit, showing T2-weighted, midsagittal plane images obtained before surgery and 3, 6, 12, and 24 weeks after stab of L2-L3, L3-L4, and L4-L5 discs. Note progressive decrease in NP area and signal intensity for each of the three stabbed discs over the 24-week period. In contrast, MRI appearance of the NP of two intact control discs (L1-2 and L5-6) remained relatively constant over the same period.

Progressive decreases in NP area and signal intensity are apparent for each of the three stabbed discs (L2-3, L3-4, and L4-5) over the 24-week period. In contrast, MRI appearance of the nucleus pulposi of the two intact control discs (L1-2 and L5-6) remained relatively constant over the same period. Figure 34 describes further MRI observations seen in the stabbed discs (L2-3, L3-4, and L4-5).

	Qualitative MRI Findings
Time (wks)	MRI
Preop	Homogeneous, bright NP; with or without horizontal band clear distinction between NP and AF
3	Start of progressive decrease NP area and S.I.
6	Some irregular shape of anterior margin of disc
12	Irregular shape of NP area dark signal detected outside anterior AF (Osteophyte)
24	Extensive decrease in NP area and S.I., increasing dark signal outside anterior AF (Osteophyte)

Figure 34. Qualitative MRI Findings of Stabbed Discs at Preop, 3, 6, 12, and 24 wks

5.1.3 MRI Analysis Using PACS Clinical Software

5.1.3.1 MRI Index – Pre-operative IVD Data

Table 1 provides the mean and standard deviation of the pre-operative NP area, average signal intensity, and MRI Index (product of area and average signal intensity) of the 18 rabbits, level by level. No statistically significant differences were detected in these data by disc level($p < .05$).

Table 1 . Preoperative MRI Data (Mean ± Standard Deviation)

Pre-operative Data (Mean ± Standard Deviation)			
Level	NP Area (mm^2)	NP S.I. (GY)	MRI Index (mm^2 GY)
L1-2	3.71 ± 0.73	378.3 ± 89.0	1402 ± 328
L2-3	3.80 ± 0.80	376.3 ± 65.4	1429 ± 348
L3-4	4.00 ± 0.50	364.7 ± 66.5	1458 ± 399
L4-5	4.25 ± 0.61	358.5± 61.5	1523 ± 206
L5-6	4.32 ± 0.63	356.7± 67.2	1549 ± 395

5.1.3.2 MRI Index – Control and Stabbed IVDs Data

Control Discs

Table 2 provides the mean and standard deviation of NP area, average signal intensity, and MRI Index of the control (L1-2, and L5-6) discs at 3, 6, 12, and 24 weeks post-stab, expressed as a percentage of pre-operative values. (These data are from MRI scans of 11 rabbits at 3 weeks post-stab, 7 rabbits at 6 and 12 weeks, and 5 rabbits at 24 weeks.)

Table 2. MRI data of Control Discs (Mean ± Standard Deviation)

MRI Data of Control Discs Using PACS (Mean ± Standard Deviation)				
Level	Time (wks)	Percent of Preop		
		NP Area	NP S.I.	MRI Index
L1-2	3	92.9 ± 13.4	97.5 ± 15.5	92.8 ± 14.5
	6	96.0 ± 9.8	94.8 ± 15.1	95.7 ± 11.9
	12	84.8 ± 25.4	83.6 ± 17.5	86.4 ± 2.4
	24	84.1 ± 22.5	80.3 ± 21.5	84.6 ± 7.9
L5-6	3	98.0 ± 13.9	86.3 ± 18.5	93.4 ± 10.4
	6	95.2 ± 11.5	81.1 ± 9.4	85.5 ± 0.4
	12	80.2 ± 19.7	78.3 ± 10.8	81.3 ± 10.5
	24	80.0 ± 17.6	84.4 ± 27.2	83.6 ± 7.2

Stabbed IVDs

Table 3 provides the mean and standard deviation of NP area, average signal intensity, and MRI Index of the stabbed (L2-3, L3-4, and L4-5) discs at 3, 6, 12, and 24 weeks post-stab, expressed as a percentage of pre-operative values. (These data are from MRI scans of 11 rabbits at 3 weeks post-stab, 7 rabbits at 6 and 12 weeks, and 5 rabbits at 24 weeks.) Note that MRI Index was the only MRI outcome measure to exhibit a significant decrease from pre-operative values by 3 weeks post-stab for all three stabbed disc levels. For the outcome measures NP area and average signal intensity, the time of onset of a significant decrease from pre-operative values varied from as early as 6 weeks post-stab to as late as 24 weeks, depending on disc level. All three MRI outcome measures, however, exhibited progressive decreases with time—without evidence of spontaneous recovery or reversal of MRI changes. By 24 weeks post-stab, mean

MRI Index had decreased to approximately 32% of pre-operative values for all three stabbed levels. Table contains a table of NP area, signal intensity, and MRI Index of stabbed IVDs.

Table 3. MRI data of Stabbed Discs (Mean ± Standard Deviation)

MRI Data of Stabbed Discs Using PACS (Mean ± Standard Deviation)				
Level	Time (wks)	Percent of Preop		
		NP Area	NP S.I.	MRI Index
L2-3	3	82.8 ± 21.4	88.2 ± 25.1	75.2 ± 11.5*
	6	75.7 ± 13.6*	71.4 ± 13.6*	52.7 ± 11.3*†
	12	60.5 ± 15.7*†	69.1 ± 25.4*	40.5 ± 16.7*†
	24	45.5 ± 15.4*	67.7 ± 20.7*	31.2 ± 12.2*†
L3-4	3	90.4 ± 19.2	89.9 ± 25.4	76.5 ± 13.9*
	6	73.2 ± 15.8*	79.7 ± 15.4	58.7 ± 18.4*
	12	57.8 ± 16.6*†	78.6 ± 26.6	44.4 ± 14.7*†
	24	47.0 ± 25.4*†	62.7 ± 16.1	31.5 ± 20.6*†
L4-5	3	92.7 ± 20.3	92.9 ± 20.0	84.6 ± 9.1*
	6	85.0 ± 10.5	91.4 ± 21.7	59.8 ± 17.2*
	12	50.5 ± 10.6*†	86.6 ± 21.1	47.0 ± 16.9*
	24	34.9 ± 16.7*†	75.6 ± 20.3*	31.7 ± 13.7*

* Significantly less than Preop value ($p<0.05$)

† Significantly less than 3 wks value ($p<0.05$)

S.I. = Signal Intensity, MRI Index = NP Area x NP S.I.

Figure 35 is a bar graph demonstrating the MRI Index of the stabbed IVDs. See appendix A for MRI Index, NP area, and signal intensity graphs of each discs level (L1/2-L5/6).

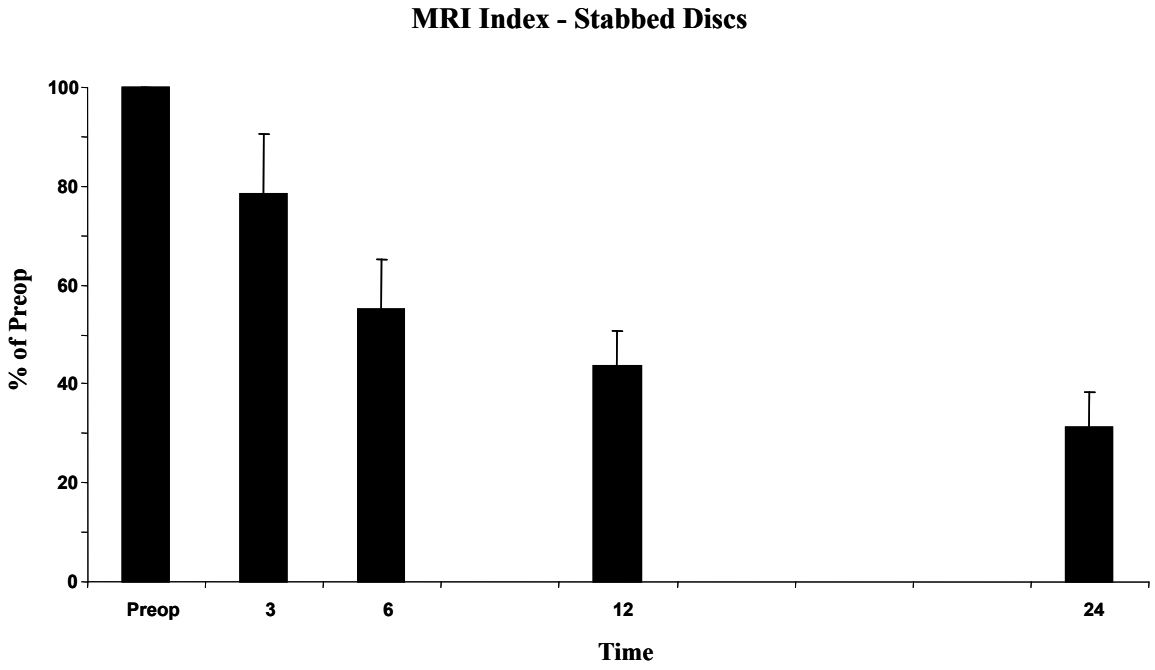

Figure 35. Mean NP MRI Index of all stabbed discs (L2-3, L3-4, and L4-5) using PACS (Mean ± Standard Deviation)

5.1.3.3 95% Confidence Interval – MRI Index

Figure 36 shows the mean nucleus pulposus MRI Index (± 95% confidence interval for the mean) of the pooled data of the stabbed discs (L2-3, L3-4, and L4-5) and the intact control discs (L1-2, L5-6), plotted against time. For both groups, by 3 weeks post-surgery, mean MRI Index was already significantly less than the corresponding pre-operative MRI Index—and remained so through 24 weeks. For the intact control disc group, mean MRI Index was 93% of pre-operative MRI Index by week 3—decreasing to 84% by week 24. For the stabbed disc group, mean MRI Index was 78% of pre-operative MRI Index by week 3—decreasing to 32% by week 24. Linear regression revealed that the average rate of change of MRI Index for the stabbed discs was –7.2% per week over the first 6 weeks ($p = .0061$), and only –1.4% per week thereafter through 24 weeks ($p = .1292$). Comparing the data of the two groups, it is noted that by 3 weeks post-surgery, the mean MRI Index of the stabbed discs was

already significantly less than that of the intact control discs. This difference became even more pronounced by 6 weeks due to the more rapid rate of decrease in MRI Index of the stabbed discs. Wide separation in MRI Index between the stabbed and intact control disc groups persisted through 12 and 24 weeks post-surgery. The narrow confidence intervals show high reproducibility of this animal model of IDD.

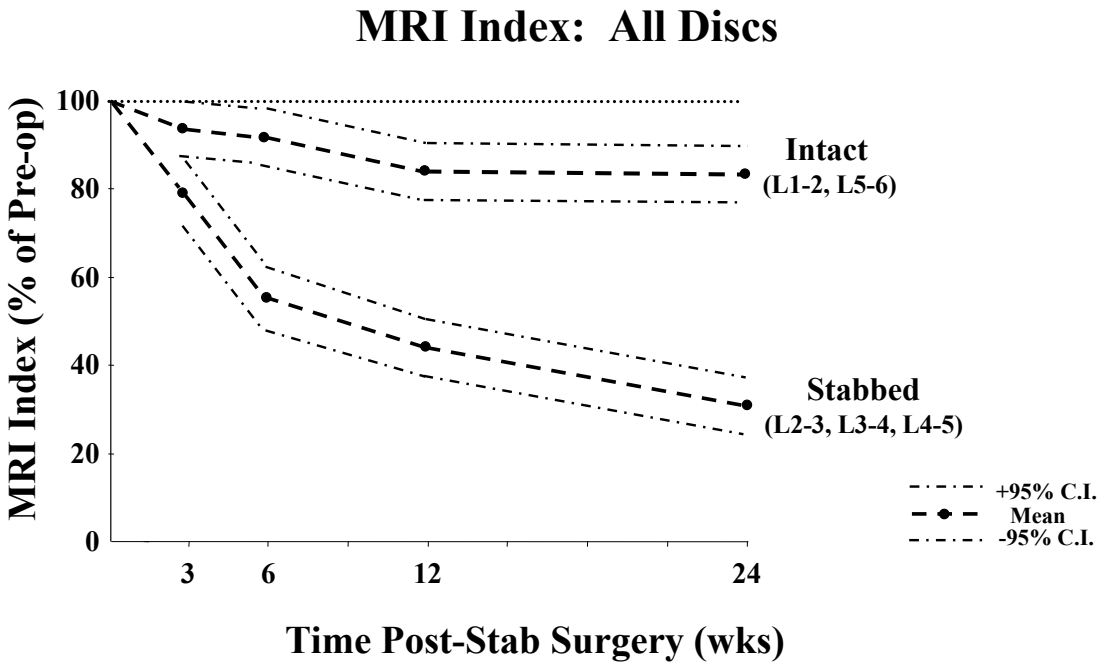

Figure 36. Mean NP MRI Index (±95% confidence interval for the mean) of all stabbed (L2-3, L3-4, L4-5) discs from T2-weighted, midsagittal plane images obtained 3, 6, 12, and 24 weeks post surgery. Narrow confidence intervals show high reproducibility of this animal model of IDD

5.1.3.4 Number of Stabbed Discs That Underwent Degeneration

Figure 37 shows the percentages of stabbed discs at 3, 6, 12, and 24 weeks post-stab exhibiting at least a 15, 30, or 45% decrease in NP MRI Index with respect to pre-operative values. (These data are from MRI scans of 33 stabbed discs at 3 weeks post-stab, 21 stabbed discs at 6 and 12 weeks, and 15 stabbed discs at 24 weeks.) By 3 weeks post-stab, over 70% of stabbed discs exhibited at least a 15% decrease in MRI Index, increasing to 93% of stabbed discs

by week 6, and 100% by week 12. Trends were similar for the 30% and 45% thresholds—demonstrating progressive "recruitment" of stabbed discs exhibiting certain amounts of MRI Index decrease. By 24 weeks post-stab, 100% of stabbed discs exhibited at least a 45% decrease in MRI Index—demonstrating no spontaneous recovery or reversal of MRI changes through 24 weeks.

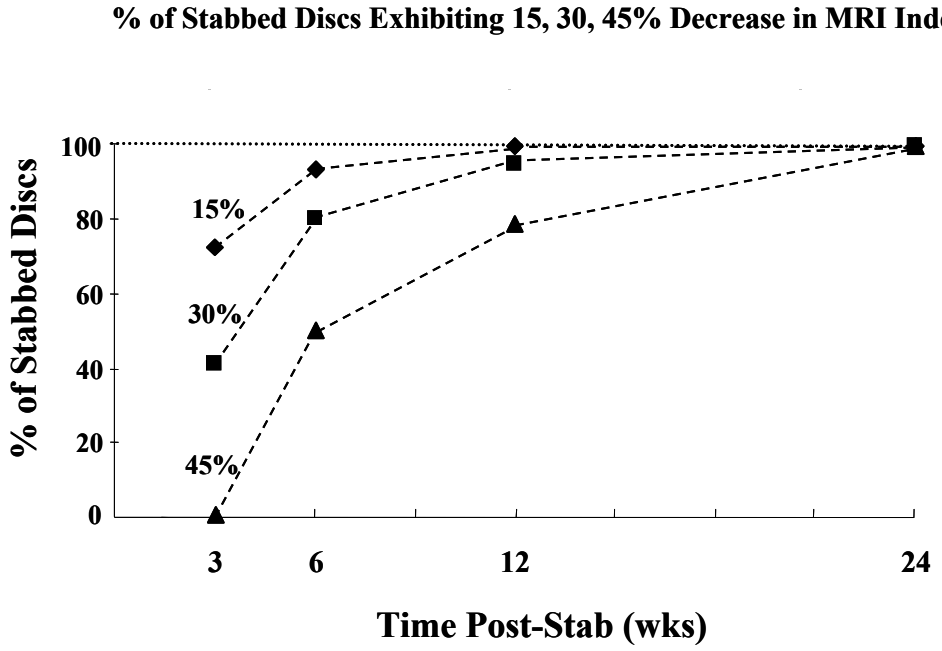

Figure 37. Percentage of stabbed discs at 3, 6, 12, and 24 weeks post stab exhibiting at least a 15, 30, or 45% decrease in NP MRI Index with respect to preoperative values. By 24 weeks post stab, 100% of stabbed discs exhibited at least a 45% decrease in MRI Index. These data demonstrate progressive recruitment of stabbed discs meeting certain thresholds of MRI Index decrease, with no evidence of spontaneous recovery or reversal of these MRI changes through 24 weeks.

5.1.3.5 MRI Intra- and Inter-Observer Repeatability

The Intra-class Correlation Coefficients (ICCs) for intra-observer repeatability of the test/retest MRI data collected at 12 weeks post-stab were 0.97 for NP area, 0.81 for signal intensity, and 0.85 for MRI Index. The corresponding ICCs for inter-observer repeatability were 0.98, 0.94, and 0.88, respectively. All ICCs were greater than 0.75 (considered an excellent degree of correlation)—suggesting that the above-reported MRI changes may be

attributed mainly to actual MRI changes in the disc (as opposed to intra- or inter-observer variability). Figure 38 shows representative MRI scans from one NZW rabbit lumbar spine (12 weeks post stab).

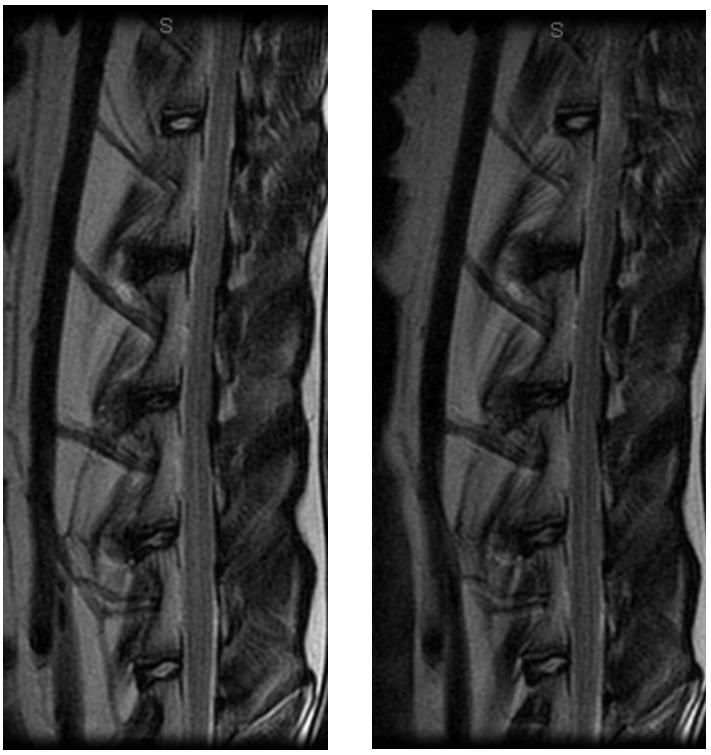

Figure 38. Representative MRI scans of lumbar spine of one rabbit (12 weeks post stab), showing T2-weighted, midsagittal plane images

5.1.4 MRI Analysis Using AMIRA 3.0 Clinical Software

5.1.4.1 MRI Index

Control Discs

Table 4 provides the mean and standard deviation of NP area, average signal intensity, and MRI Index of the control discs (L1-2, L5-6) discs at 3, 6, 12, and 24 weeks expressed as percentage of pre-operative values.

Table 4. MRI data of Control Discs (Mean ± Standard Deviation)

MRI Data of Control Discs Using AMIRA (Mean ± Standard Deviation)				
Level	Time (wks)	Percent of Preop		
		NP Area	NP S.I.	MRI Index
L1-2	3	93.5 ± 11.2	94.5 ± 11.0	96.1 ± 19.4
	6	89.1 ± 10.5	96.8 ± 9.5	90.7 ± 11.5
	12	86.3 ± 17.2	94.2 ± 14.2	90.5 ± 24.8
	24	92.1± 15.2	93.2 ± 18.4	90.9 ± 17.9
L5-6	3	95.3 ± 18.2	94.1 ± 19.5	92.1 ± 14.9
	6	84.2 ± 10.4	87.6 ± 11.2	82.7 ± 17.1
	12	86.3 ± 21.2	85.6 ± 16.2	90.4 ± 18.5
	24	82.4 ± 18.6	86.2 ± 21.2	88.8 ± 15.7

Stabbed Discs

Table 5 provides the mean and standard deviation of NP area, average signal intensity, and MRI Index of the stabbed (L2-3, L3-4, and L4-5) discs at 3, 6, 12, and 24 weeks post-stab, expressed as a percentage of pre-operative values. As seen with PACS, MRI Index was the only MRI outcome measure to exhibit a significant decrease from pre-operative values by 3 weeks post-stab for all three stabbed disc levels. For the outcome measures NP area and average signal intensity, the time of onset of a significant decrease from pre-operative values varied from as early as 6 weeks post-stab to as late as 24 weeks, depending on disc level. All three MRI outcome measures, however, exhibited progressive decreases with time—without evidence of spontaneous recovery or reversal of MRI changes. By 24 weeks post-stab, mean MRI Index had decreased to approximately 39% of pre-operative values for all three stabbed levels. Table 6 demonstrates NP area, signal intensity, and MRI Index of stabbed IVDs using AMIRA software.

See appendix B for NP area and signal intensity graphs of individual IVDs with AMIRA software.

Table 5. MRI data of Control Discs (Mean ± Standard Deviation)

MRI Data of Stabbed Discs Using AMIRA (Mean ± Standard Deviation)				
Level	Time (wks)	Percent of Preop		
		NP Area	NP S.I.	MRI Index
L2-3	3	79.2 ± 24.5	84.2 ± 25.1	76.2 ± 23.5*
	6	68.5 ± 20.4*	75.3 ± 18.4*	54.7 ± 14.7*
	12	57.6 ± 16.5*	60.2 ± 25.4*	40.1 ± 23.1*
	24	41.3 ± 15.4*†	61.5 ± 20.7*	38.4 ± 19.6*†
L3-4	3	81.3 ± 22.1	86.5 ± 25.4	71.8 ± 17.1*
	6	70.2 ± 17.6*	74.3 ± 26.3	67.4 ± 22.2*
	12	63.5 ± 19.3*†	72.1 ± 26.6	55.9 ± 24.8*
	24	42.5 ± 25.1*†	66.8 ± 16.1*	37.4 ± 24.9*†
L4-5	3	94.3 ± 15.2	97.6 ± 17.3	95.0 ± 19.1
	6	75.3 ± 26.3	84.5 ± 18.6	61.7 ± 21.5*
	12	44.6 ± 13.6*	83.4 ± 24.1	58.0 ± 37.4*
	24	38.5 ± 16.7*†	67.7 ± 22.3*	42.9 ± 15.7*†

* Significantly less than Preop value ($p<0.05$)

† Significantly less than 3 wks value ($p<0.05$)

S.I. = Signal Intensity, MRI Index = NP Area x NP S.I.

Figure 39 represents a bar graph demonstrating the MRI Index of the stabbed IVDs.

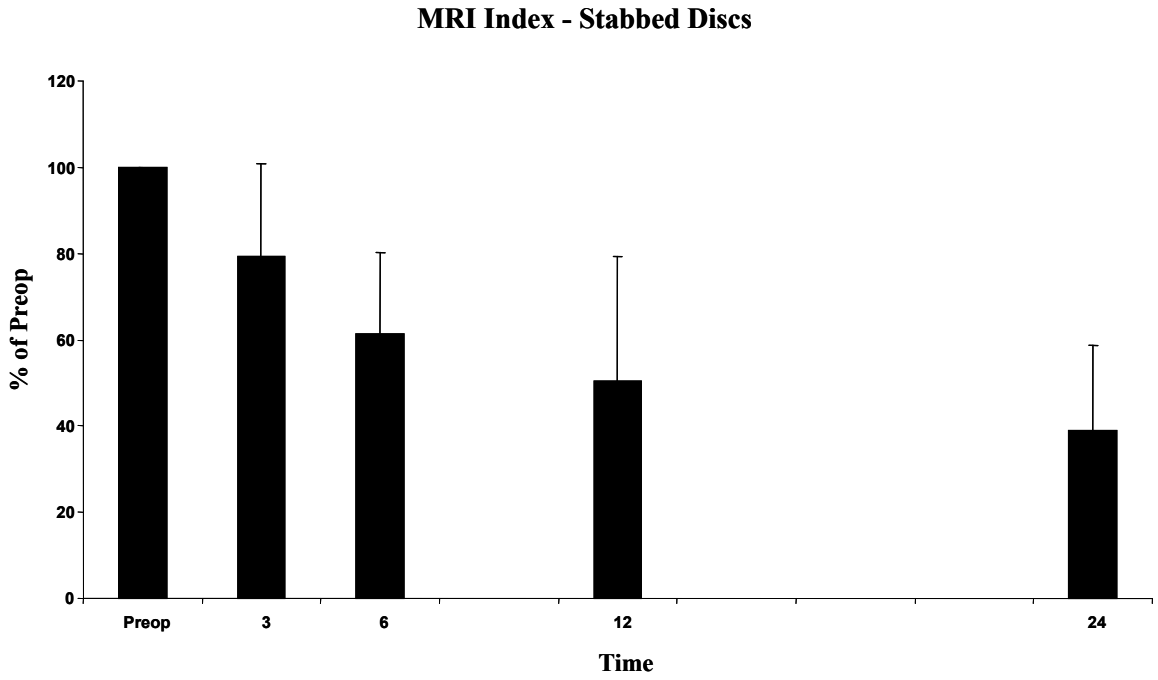

Figure 39. Mean NP MRI Index of all stabbed discs (L2-3, L3-4, and L4-5) using PACS (Mean ± Standard Deviation)

5.1.4.2 95% Confidence Interval

Figure 40 shows the mean nucleus pulposus MRI Index (± 95% confidence interval for the mean) of the pooled data of the stabbed discs (L2-3, L3-4, and L4-5) and the intact control discs (L1-2, L5-6), plotted against time. For both groups, by 3 weeks post-surgery, mean MRI Index was already significantly less than the corresponding pre-operative MRI Index—and remained so through 24 weeks. For the intact control disc group, mean MRI Index was 94% of pre-operative MRI Index by week 3—decreasing to 89% by week 24. For the stabbed disc group, mean MRI Index was 79% of pre-operative MRI Index by week 3—decreasing to 39% by week 24. Linear regression revealed that the average rate of change of MRI Index for the stabbed discs was –7.2% per week over the first 6 weeks ($p = .0061$), and only –1.4% per week thereafter through 24 weeks ($p = .1292$). Comparing the data of the two

groups, it is noted that by 3 weeks post-surgery, the mean MRI Index of the stabbed discs was already significantly less than that of the intact control discs. This difference became even more pronounced by 6 weeks due to the more rapid rate of decrease in MRI Index of the stabbed discs. Wide separation in MRI Index between the stabbed and intact control disc groups persisted through 12 and 24 weeks post-surgery. The narrow confidence intervals show high reproducibility of this animal model of IDD.

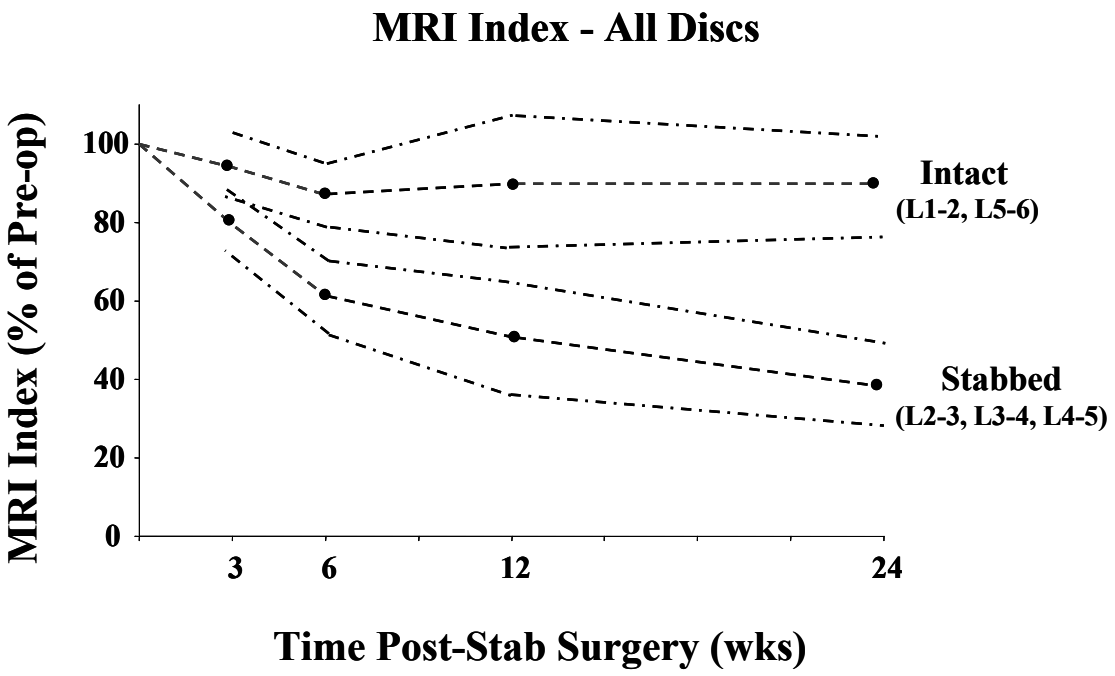

Figure 40. Mean NP MRI Index (±95% confidence interval for the mean) of all stabbed (L2-3, L3-4, L4-5) discs from T2-weighted, midsagittal plane images obtained 3, 6, 12, and 24 weeks post surgery.

5.1.4.3 # of Stabbed Discs That Underwent Degeneration

Figure 41 shows the percentages of stabbed discs at 3, 6, 12, and 24 weeks post-stab exhibiting at least a 15, 30, or 45% decrease in NP MRI Index with respect to pre-operative values. By 3 weeks post-stab, over 65% of stabbed discs exhibited at least a 15% decrease in

MRI Index, increasing to 81% of stabbed discs by week 6, and 100% by week 24. Trends were similar for the 30% threshold—demonstrating progressive "recruitment" of stabbed discs exhibiting certain amounts of MRI Index decrease. A similar trend was also seen for the 45% threshold with the exception that by 24 weeks post-stab, 77% of stabbed discs exhibited at least a 45% decrease in MRI Index.—which also demonstrated no spontaneous recovery or reversal of MRI changes through 24 weeks.

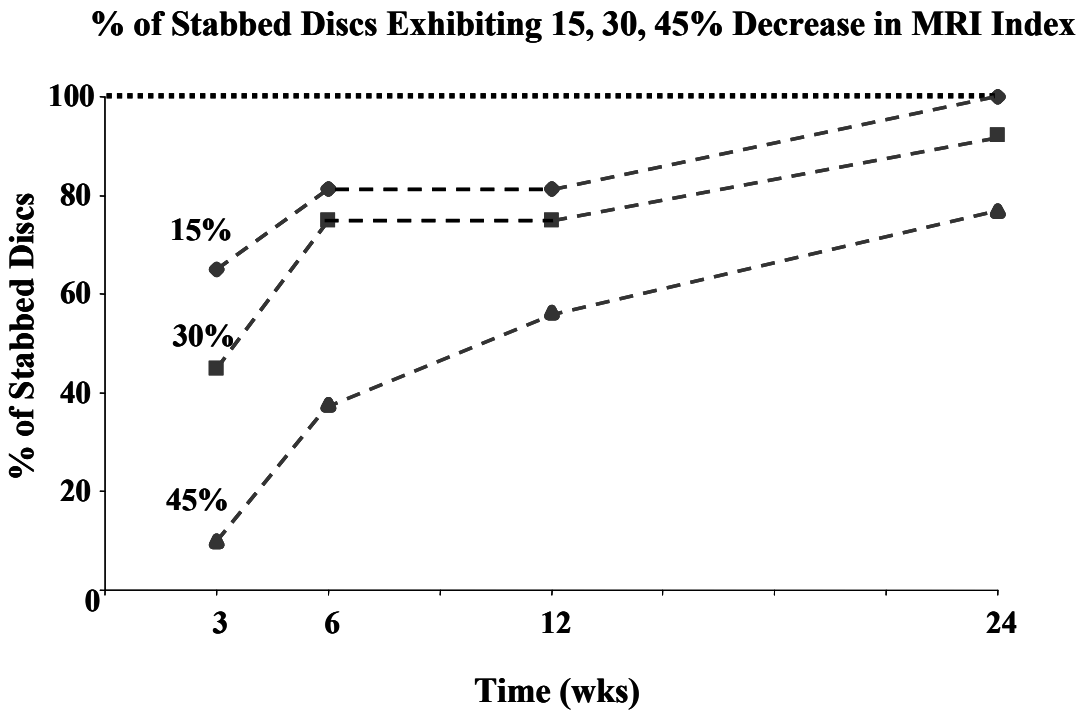

Figure 41. Percentage of stabbed discs at 3, 6, 12, and 24 weeks post stab exhibiting at least a 15, 30, or 45% decrease in NP MRI Index with respect to preoperative values. These data demonstrate progressive recruitment of stabbed discs meeting certain thresholds of MRI Index decrease, with no evidence of spontaneous recovery or reversal of these MRI changes through 24 weeks.

5.1.5 Natural Course of Rabbit IVD Degeneration

Figure 42 illustrates representative T2-weighted MRIs of one rabbit demonstrating natural course of IDD. The MRIs were taken using the 5 inch surface coil at 1.5T at time 0, 12, and 24 wks, with rabbits discs (L1-2-L5-6) left intact (no stab surgery).

Figure 42. Representative serial MRI scans of lumbar spine of one rabbit, showing T2-weighted, midsagittal plane images obtained at time 0, 12, and 24 weeks of L1-2, L2-L3, L3-L4, L4-L5, and L5-6 discs.

Figure 43 shows MRI Index of 4 rabbits calculated as described in section 4.1.3.2. No statistically significant differences were detected in these data between weeks ($p < .05$). MRI Index remains fairly constant through the 24 week time point.

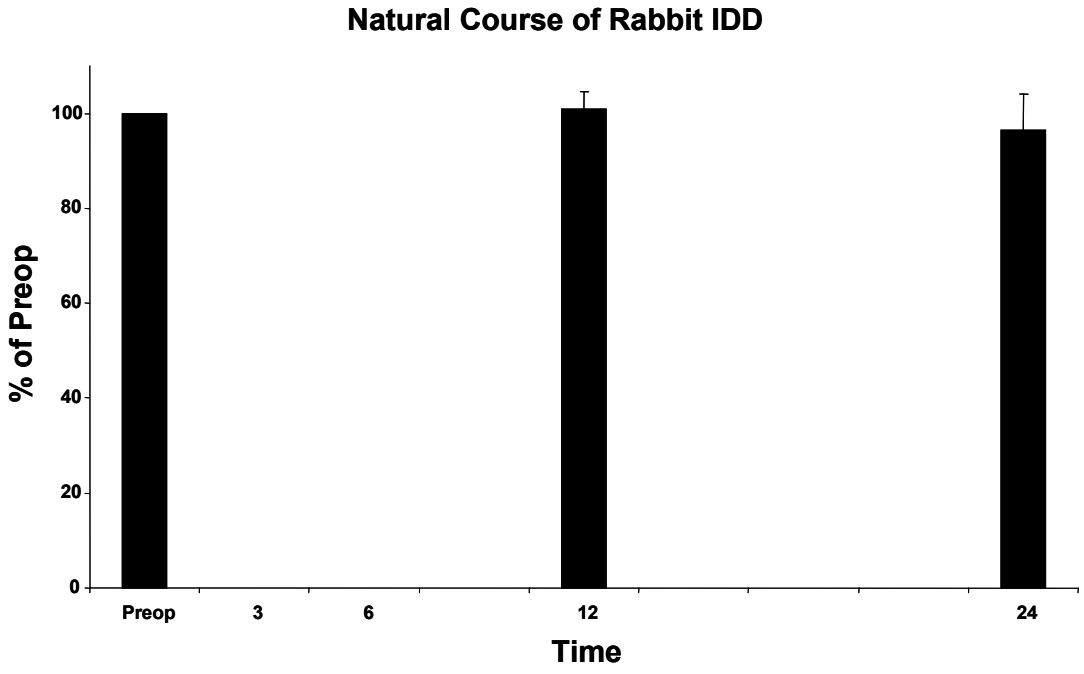

Figure 43. Mean NP MRI Index of natural course of degeneration (L1-2, L2-3, L3-4, L4-5, and L5-6) using AMIRA (Mean ± Standard Deviation)

Table 6 provides mean and standard deviation of NP area, average signal intensity, and MRI Index of all discs (L1-2, L2-3, L3-4, L4-5 and L5-6) discs at time 0, 12, and 24 weeks expressed as a percentage of time 0 values. (These data are from MRI scans of 4 rabbits)

Table 6. Natural Course MRI Index as a Percent of Preop (Mean ± Standard Deviation)

MRI Index - Natural Course of Degeneration (Mean ± Standard Deviation)				
Level	Time (wks)	Percent of Preop		
		NP Area	NP S.I.	MRI Index
L1-2	12	90.2 ± 2.3	108.7 ± 4.5	98.1 ± 1.6
	24	92.8 ± 1.6	96.1 ± 16.5	96.9 ± 3.2
L2-3	12	87.5 ± 2.6	116.6 ± 5.7	102.1 ± 1.9
	24	90.1 ± 8.9	111.5 ± 13.1	99.7 ± 6.8
L3-4	12	95.7 ± 2.4	108.4 ± 1.5	103.6 ± 1.2
	24	96.5 ± 10.4	101.8 ± 17.3	97.4 ± 12.1
L4-5	12	100.8 ± 11.6	105.8 ± 6.7	98.1 ± 7.2
	24	107.2 ± 8.7	84.7 ± 16.8	87.7 ± 8.5
L5-6	12	76.4 ± 0.2	133.1 ± 9.1	101.6 ± 7.3
	24	84.9 ± 5.2	114.6 ± 3.1	97.3 ± 5.9

5.2 PART 2: HARDWARE: DEVELOPMENT OF 3.0T MRI QUAD COIL FOR IMAGING RABBIT SPINE.

5.2.1 SNR Measurements of Existing Clinically Available MR Coils

The body and head coil at 1.5T demonstrated the lowest SNR of the coils tested with values of 7.3 and 17.83 respectively. These coils did allowed for ample coverage of the rabbit spine, although were not the optimal geometry for rabbit lumbar spine. The 3 and 5 inch at 1.5T both performed with better SNR than the head and body coils at 1.5T. As expected the 3 inch possessed higher SNR than the 5 inch with values of 39.31 and 28.62 respectively. The coverage

of the 3 inch coil was insufficient for imaging the L1/2 to L5/6 lumbar IVDs of a NZW rabbit. The 5inch coverage was more capable of acquiring these discs although not ideal for rabbit spine. The head and body coils were then tested at 3.0T. The SNR of the head coil was similar to that of the 5 inch coil at 1.5T and was more than twice that of the body coil at 3.0T. The head coil at 3.0T demonstrated a larger coverage range than the 5 inch coil at 1.5T despite both having similar SNRs.

Since, the 3.0T scanner was not available during the start of the animal model study, the 5 inch surface coils was the best option to complete the study. Although, the 5 inch coil displayed some performance concerns and the need for a custom coil became apparent.

(A)

(B)

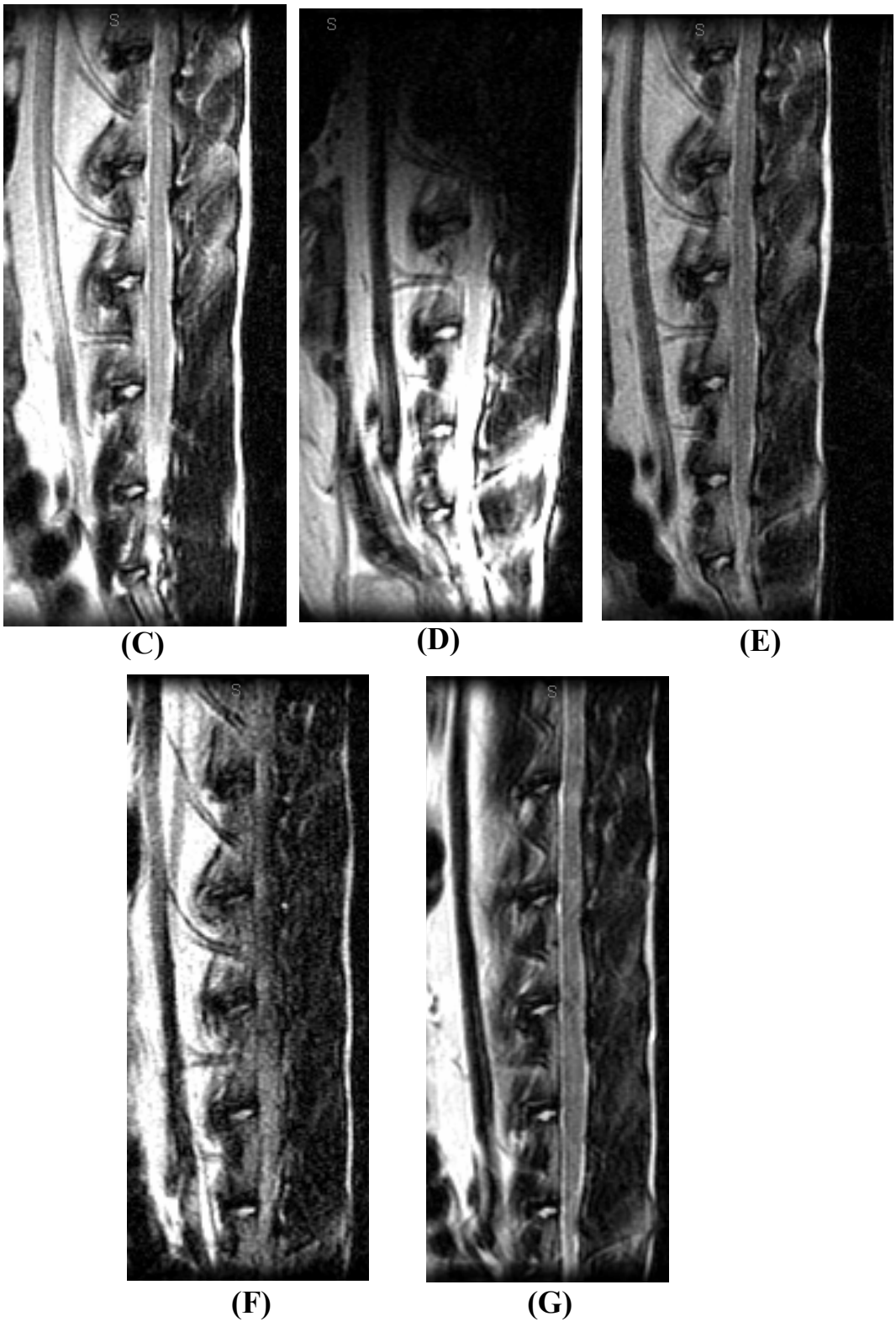

Figure 44. Body coil (A), head coil (B), 5 inch surface coil (C), 3 inch surface coil (D), license plate coil (E) at 1.5T; and body coil (F), Head coil (G) at 3.0T

Table 7 describes the SNR results obtained from MRIs of various commercially available coils.

Table 7. SNR measurements of commercially available MRI coils

SNR Measurements From Various Commercially Available Coils	
Coil Type	SNR Measurements
3” Surface (1.5T)	39.31
5” Surface (1.5T)	28.62
License Plate (1.5T)	13.01
Head (1.5T)	17.83
Body (1.5T)	7.30
Head (3.0T)	32.30
Body (3.0T)	13.87

5.2.2 X-Ray study: Location of Rabbit Spine With 1.5T Scanning Method

Calibration

Figure 45 show an x-ray of 2.5 inch diameter steel calibration cylinder. The measurement of the calibration cylinder on the x-ray was 2.75inches, resulting in a 0.25inch magnification. All rabbit x-rays where then multiplied by .91in. to obtain the accurate dimensions.

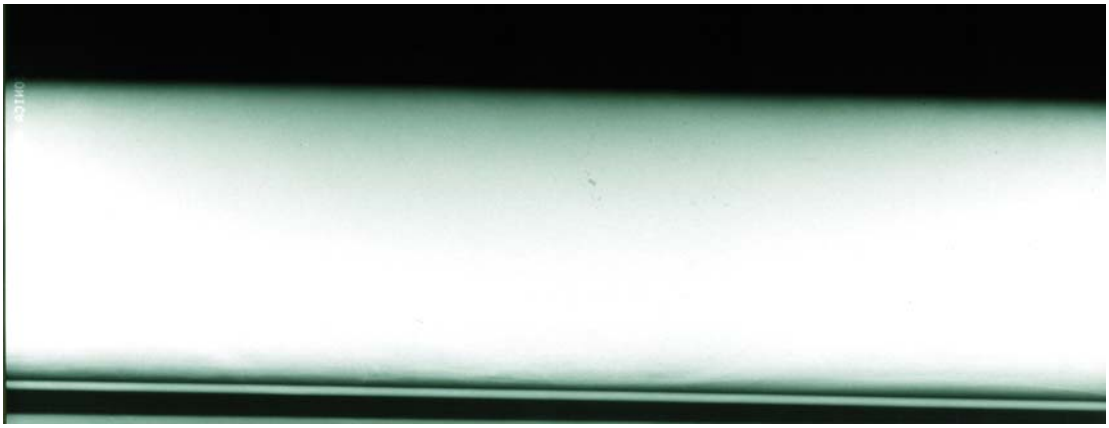

Figure 45. X-ray of calibration cylinder using 1.5T scanning setup.

Rabbit Study:

The goal of this study was to determine the location of the rabbit spine in reference to the 5 inch surface coil. Figure 46 shows an x-ray of a NZW. The calibration findings in section 5.2.2 were used to correct for magnification of the rabbit x-ray. The distance from the k-wire to the most anterior portion of the rabbit lumbar IVD was 34.7mm. Finally, the anterior to posterior distance of the rabbit spine was 12.8mm.

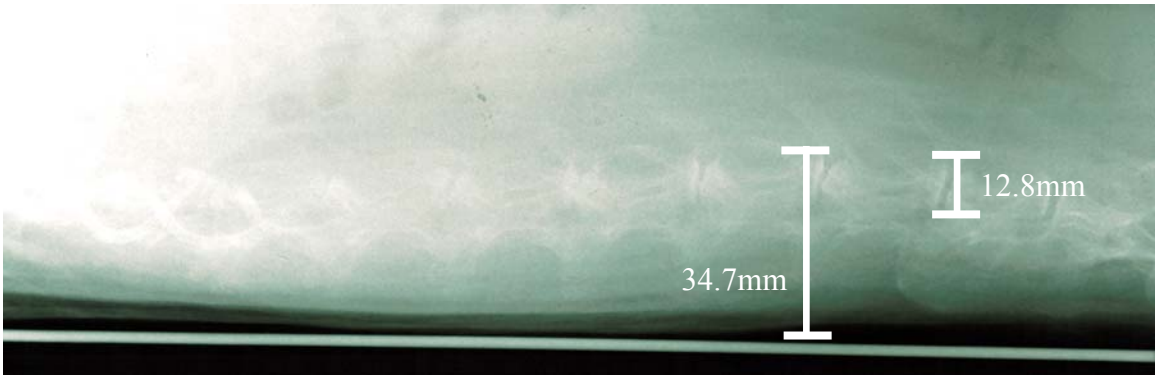

Figure 46. X-ray of rabbit spine using 1.5T scanning setup

5.2.3 X-Ray Study: Location of Rabbit Spine With 3.0T Scanning Method

Calibration

Figure 47 show x-ray of steel calibration cylinder. Contains the measurements completed on the x-ray. The real dimension of the cylinder was 2.5in. The measurement of the calibration cylinder on the x-ray was 2.75in. Thus, the cylinder was magnified by .25in. All rabbit x-rays where then multiplied by .91in. to obtain the accurate dimensions. These results were consistent with the calibration measurements in section 5.2.2.

Figure 47. X-ray of calibration cylinder using wooden trough

Rabbit Study:

Figure 48 shows an x-ray of a NZW rabbit. The calibration findings in section 5.2.2 were used to correct for magnification of rabbit x-ray. The goal of this study was to determine the location of the rabbit spine while the anesthesized rabbit lay supine in the quad coil. The x-ray study was completed on the wood trough, which was constructed to resemble the future quad coil prototype

design. An important factor in designing the quad coil was confirming that the spine would be positioned in the range of the coil. Thus, the distance from the k-wire to the most anterior portion of the rabbit lumbar IVD was measured at 44.2mm. Another critical measurement was the anterior to posterior distance of the rabbit spine, which was measured to be 12.2mm. A phantom of similar size was then constructed for the MRI phantom studies with the quad coil (described later in the thesis).

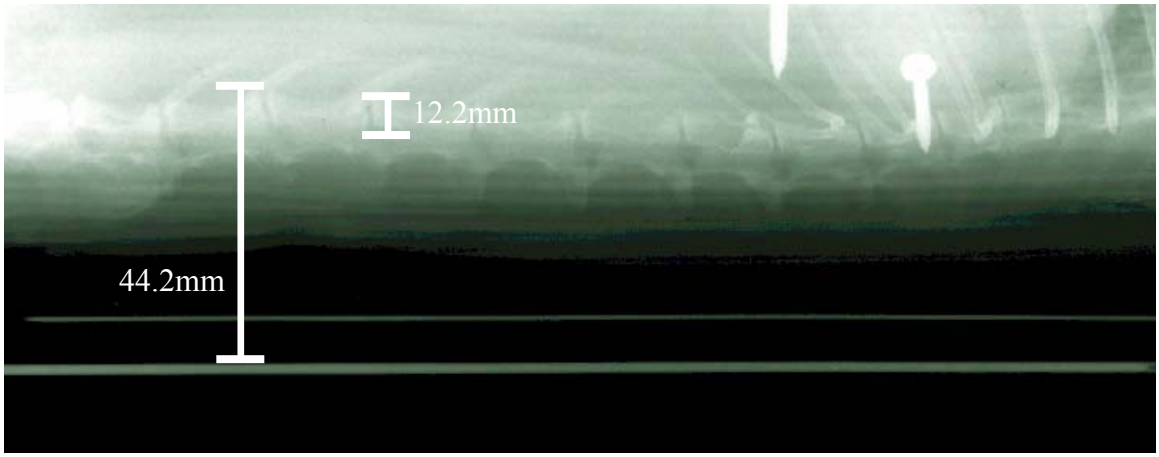

Figure 48. X-ray of rabbit spine using wooden trough

5.2.4 Quality Factor Results

Figure 49 is a plot of the Q factor measurement. A 1kg load produces a Q of 30 and 35 for the X and Y ports respectively. The Q factor decreases to 18 and 25 for the X and Y ports respectively with a 6kg load, although, the Q values remain relatively constant over the 3-5kg loading. The 3-5kg range is the weights of the rabbits used in the study.

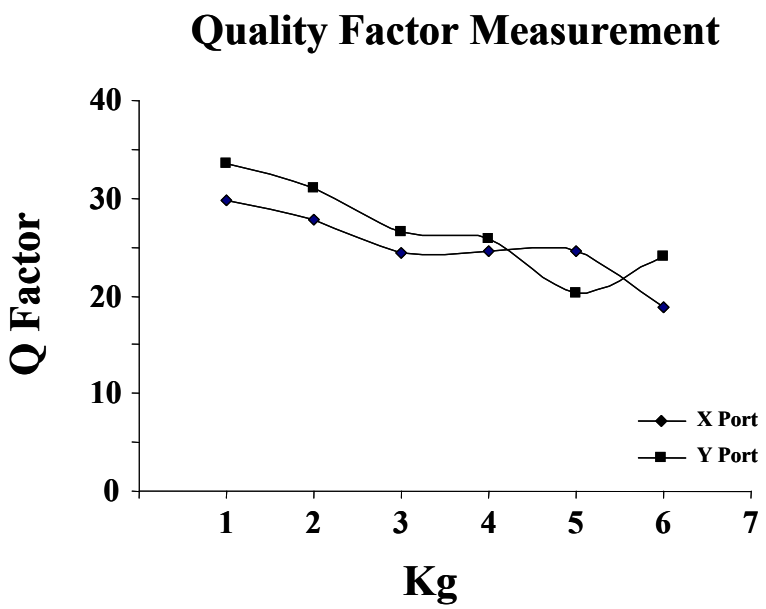

Figure 49. Plot of Quality Factor vs. Load(kg). 1 liter CuSO4 bags were loaded on quad coil to a 6kg load. Note the "leveling" off of the curve between 3-6kg, which is the range of weights of the rabbits

5.2.5 Reference Phantom Development For 3.0T Quad Coil

Figure 50 shows MRIs obtained on the 1.5T scanner using the 3/8 inch tube. Preliminary T2-axial and sagittal images demonstrated that signal was achievable with the 3/8 inch tube.

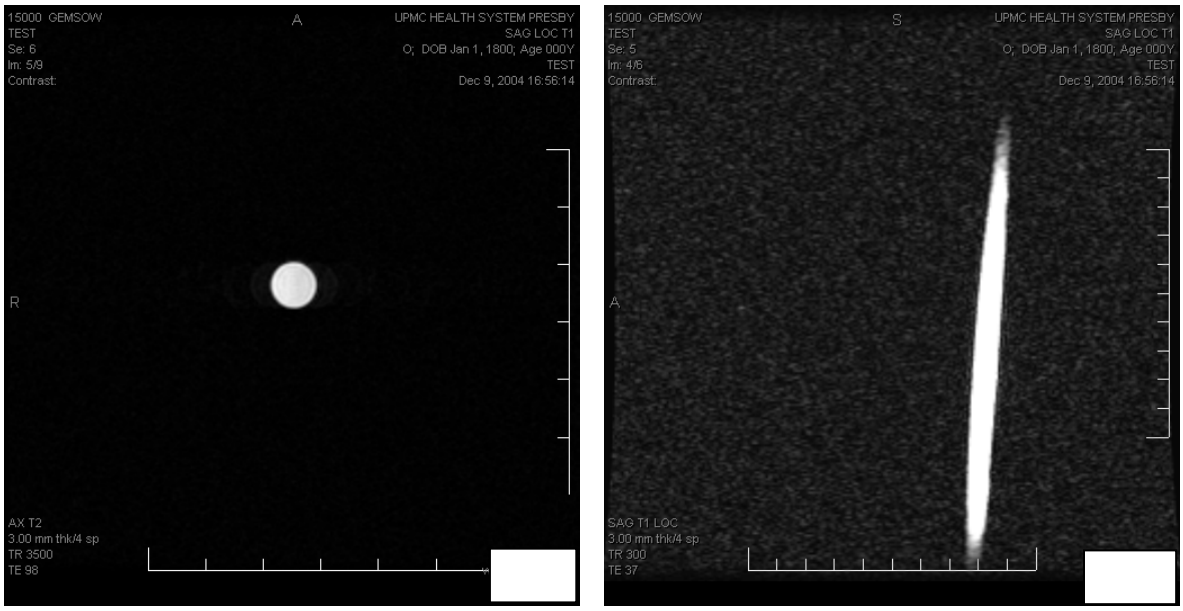

Figure 50 T2-weighted Axial (A), and sagittal (B) scans of 3/8 inch tube (reference phantom) at 1.5T.

Figure 51 illustrates preliminary T2-axial and sagittal images of one NZW rabbit containing the 3/8 inch reference phantom. The goal was to determine if the cardboard trough, which was the desired size for the prototype quad coil, could produce a rabbit image with a reference phantom in the FOV.

First, a preliminary T2-weighted axial image was obtained. The rabbit disc was clearly visible along with the reference phantom in the FOV. Then, a T2-weighted sagittal image was acquired. This again produced a clear rabbit image, which contained the reference phantom in the FOV.

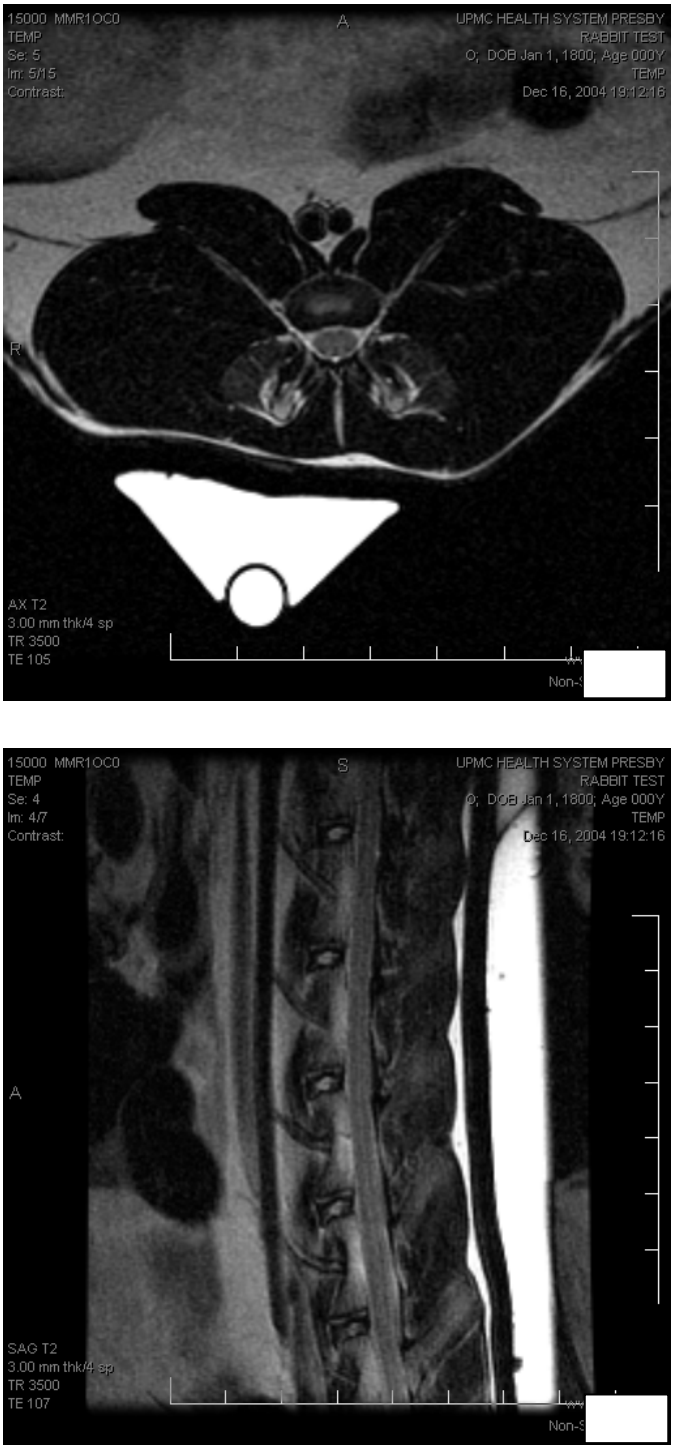

Figure 51. T2-weighted Axial (A), and sagittal (B) scans of same NZW rabbit at 1.5T.

5.2.6 Phantom Image Comparisons at 1.5 and 3.0T

The following sections 5.2.7.1.1 and 5.2.7.1.2 contain sagittal localizer images with 20 and 30cm FOVs (parameters described in section 4.1.2) in order to determine the coverage of the 5 inch surface and custom quad coils. Moreover, SNR as a function of longitudinal position was plotted to quantitatively determine the coverage of the 5 inch surface coil as compared to the custom quad coil.

5.2.6.1 20cm FOV

Figure 52 contains a sagittal localizer phantom image (section 4.2.8) with the 5 inch surface coil at 1.5T and custom quad coil at 3.0T using a 20cm FOV.

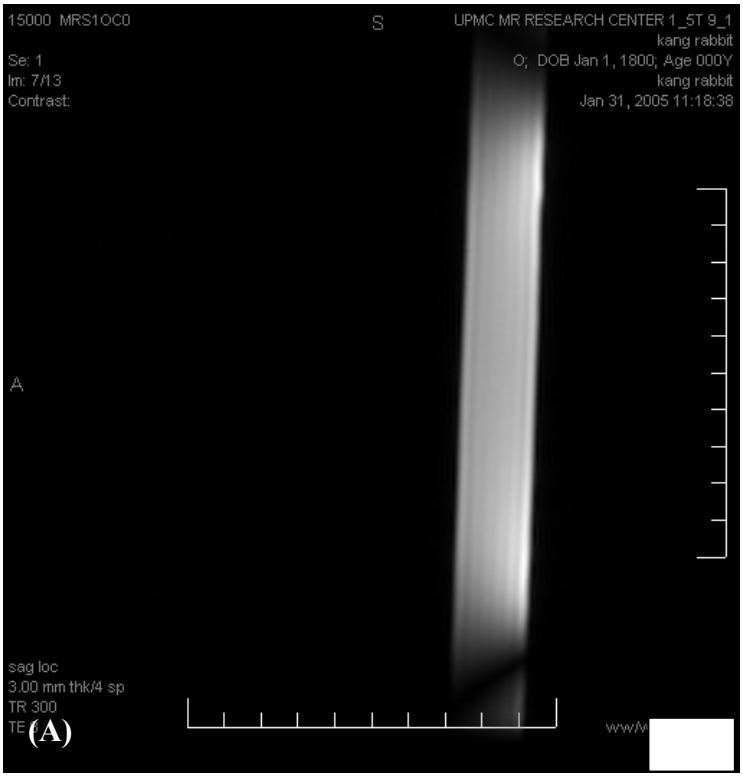

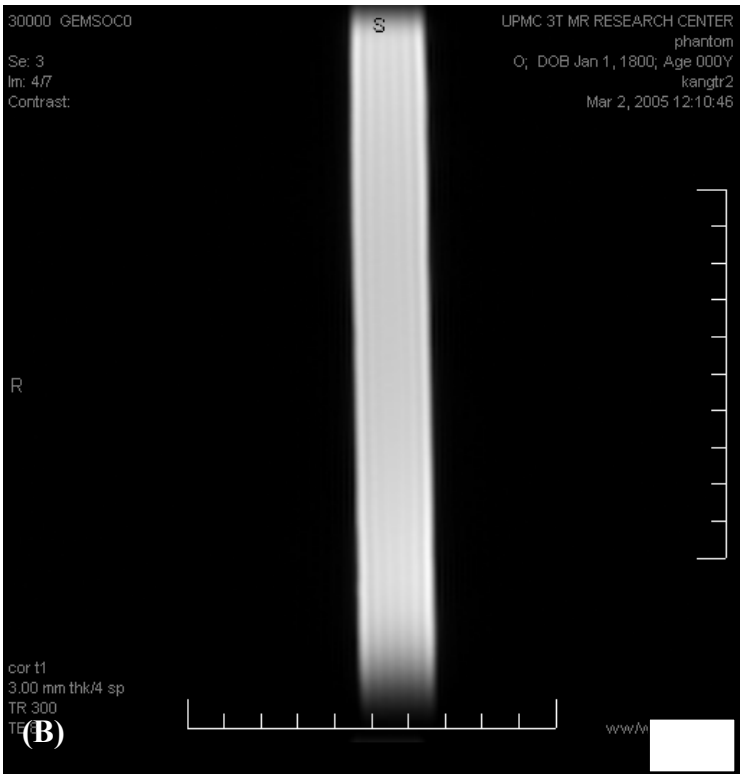

Figure 52. Sagittal localizer scans with 5 inch surface coil at 1.5T (A), and custom quad coil at 3.0T (B), using a 20cm FOV

Figure 53 illustrates the SNR profile of the 5 inch surface and custom quad coils using a 20cm FOV. Note the increased coverage of the custom quad coil as compared to the 5 inch surface coil. Also, the quad coil demonstrates slightly more than double the SNR when compared to the 5 inch surface coil.

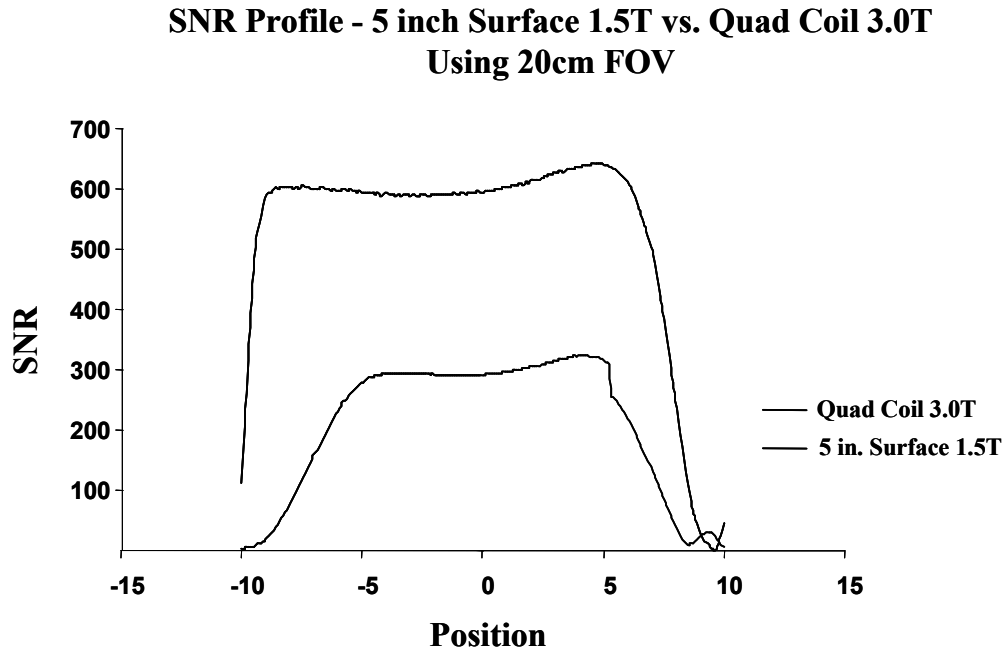

Figure 53. SNR Profile of 5 inch surface at 1.5T and quad coil 3.0T. Note larger range of the quad coil compared to the 5 inch surface. Moreover, the custom quad coil demonstrates approximately double the SNR when compared to the 5 inch surface coil.

5.2.6.2 30cm FOV

Figure 54 contains phantom images (section 4.2.8) with the 5 inch surface coil at 1.5T and custom quad coil at 3.0Tusing a 30cm FOV.

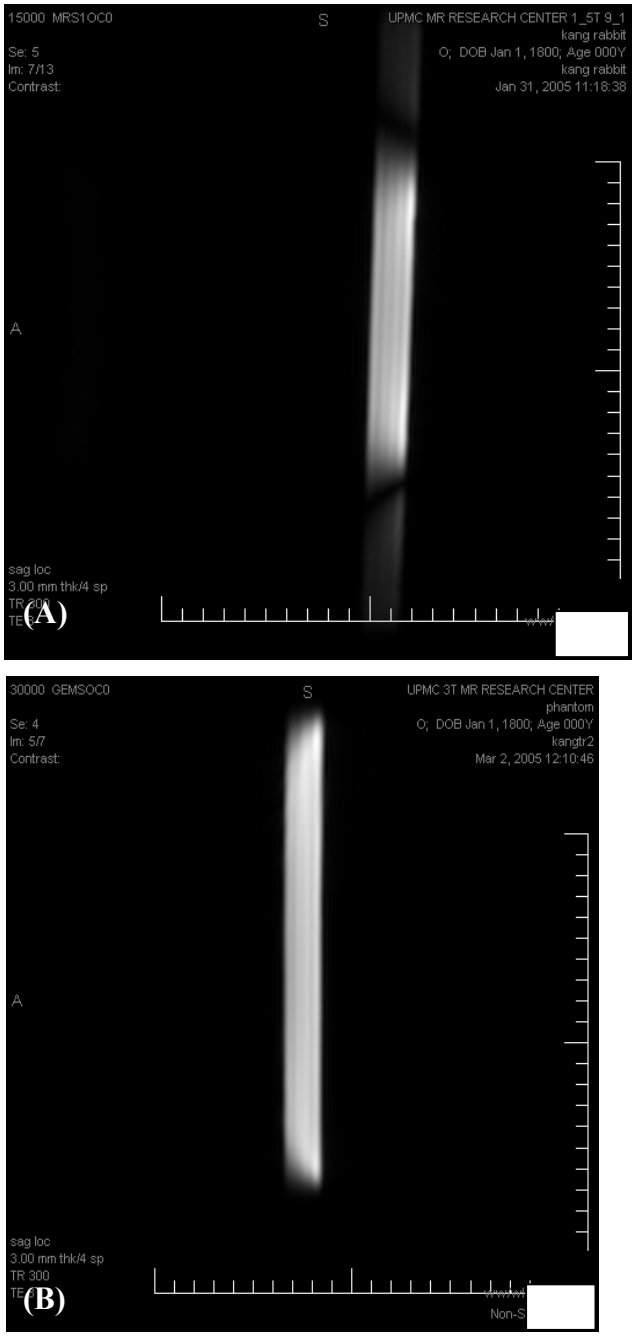

Figure 54 Sagittal localizer scans with 5 inch surface coil at 1.5T (A), and custom quad coil at 3.0T (B), using a 30cm FOV

Figure 55 illustrates the SNR profile of the 5 inch surface and custom quad coils using a 30cm FOV. The increased coverage of the custom quad coil as compared to the 5 inch surface coil was again demonstrated with the 30cm FOV. The quad coil possesses a longitudinal range of 24cm, thus it was important to test the "true" range of the coil by selecting a FOV larger than 24cm. For comparison reasons the 5 inch surface coil was also scanned using a 30cm FOV.

The SNR profile of the quad coil reveals that in practice the quad coil does have a longitudinal range of approximately 24cm, since the range if SNR values as a function of position span from -14 to 10. Clearly, the custom quad coil has a larger scanning range allowing for the rabbit lumbar IVDs of interest to be imaged accurately. Moreover, accurate positioning of the rabbit in the desired FOV will become easier and more time efficient.

Finally, the custom quad coil demonstrates slightly more than double the SNR when compared to the 5 inch surface coil using the 30cm FOV. The 5 inch surface and quad coils each provide an area of acceptable and consistent SNR values. Although, for accurately scanning rabbit lumbar spine the custom quad coil will provide higher SNR in a larger area when compared to the 5 inch surface coil.

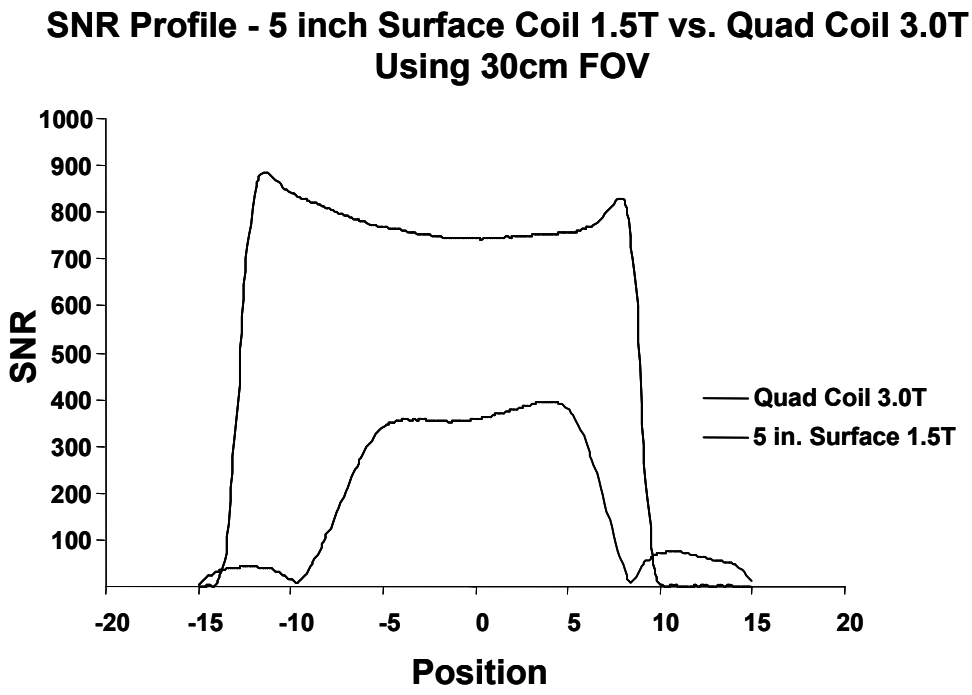

Figure 55. SNR Profile (30cm FOV) of 5 inch surface at 1.5T and quad coil 3.0T. Note the 30cm FOV is larger than the range of the quad coil, resulting accurate method of testing the full SNR profile of the quad coil.

5.2.7 In-vivo Rabbit Image Comparisons – 1.5T vs. 3.0T

5.2.7.1 Rabbit Scans Comparisons 1.5T vs. 3.0T – 256x256 Matrix Size

Figure 56 shows T2-weighted sagittal MRIs obtained with the 5 inch surface and custom quad coils from one NZW rabbit using the same resolution (256x256 matrix size, 12cm FOV). The scanning parameters used were those described in section 4.2.1, and were also held constant in order to acquire and compare the SNR in the two coils.

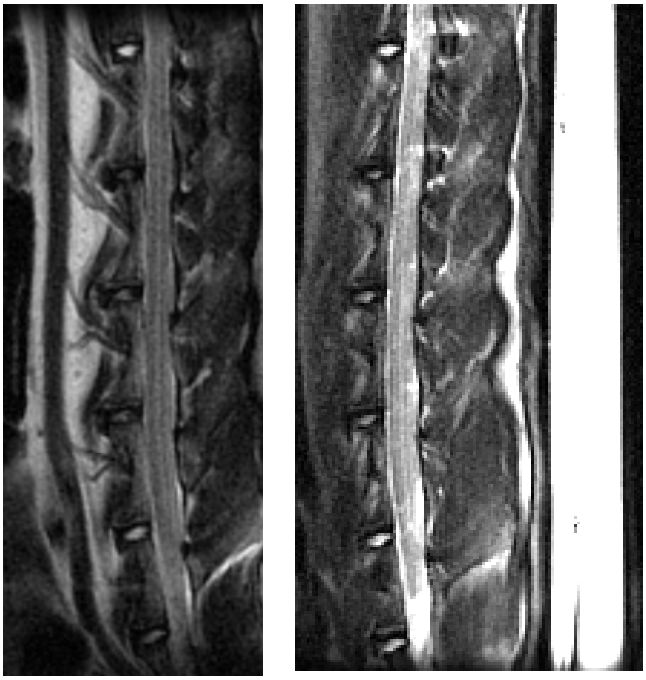

Figure 56. T2-weighted scans of one rabbit with the 5 inch surface coil (A), and the custom quad coil with reference phantom (B).

Figure 57 shows screen captures of the magnified L1-2 disc such that each pixel of the disc can be seen.

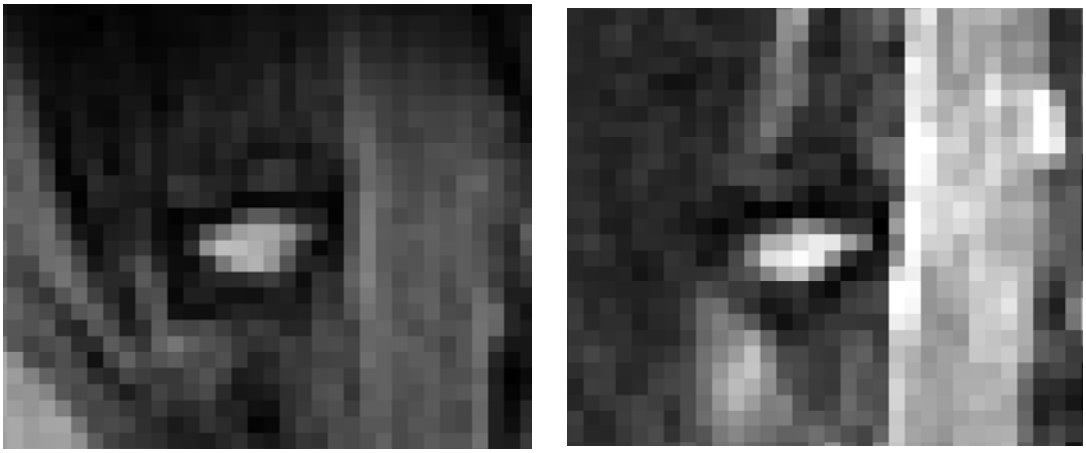

Figure 57 Magnified screen capture of the L1-2 disc obtained with the 5 inch surface coil at 1.5T (256x256 matrix size) (A), and the custom quad coil (256x256 matrix size) (B).

Table 8 shows SNR values of the rabbit scans completed with the 5 inch surface and custom quad coil, at 1.5T and 3.0T respectively.

Table 8. SNR measurements of 5 inch surface and quad coils, with a 256x256 matrix size

In-vivo SNR Measurements of 5 inch Surface and Custom Quad Coils	
Coil Type	SNR Measurements
5” Surface (1.5T)	27
Custom Quad (3.0T)	52

Figure 58 illustrates the SNR profile of the reference phantom within the rabbit MRI.

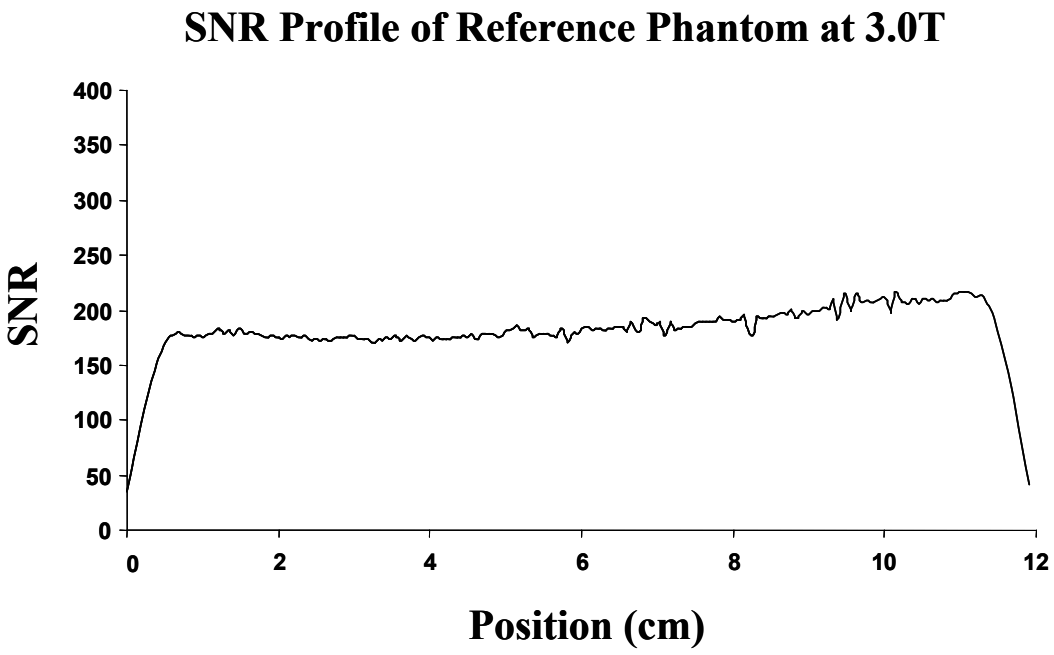

Figure 58. SNR profile of Reference Phantom at 3.0T

5.2.7.2 Rabbit Scans – 1.5T (256x256, 12cm FOV) vs. 3.0T (512x512, 12cm FOV)

Figure 59 shows T2-weighted sagittal MRIs obtained with the 5 inch surface and custom quad coils from one NZW rabbit using 256x256 and 512x512 matrix sizes respectively.

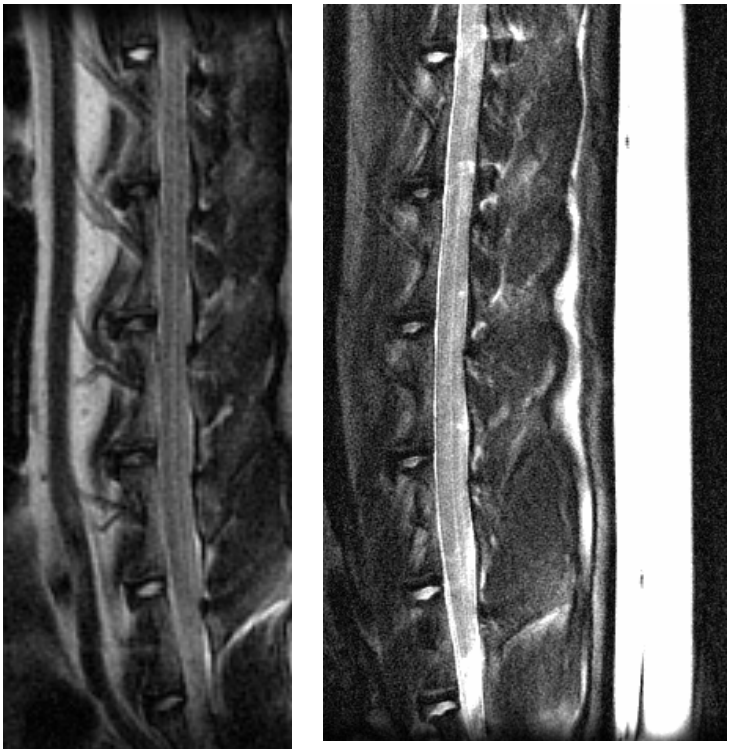

Figure 59. T2-weighted scans of one rabbit with the 5 inch surface coil 256x256 matrix (A), and the custom quad coil with reference phantom 512x512 matrix size (B).

Figure 60 shows screen captures of the magnified L1-2 disc such that each pixel of the disc can be seen.

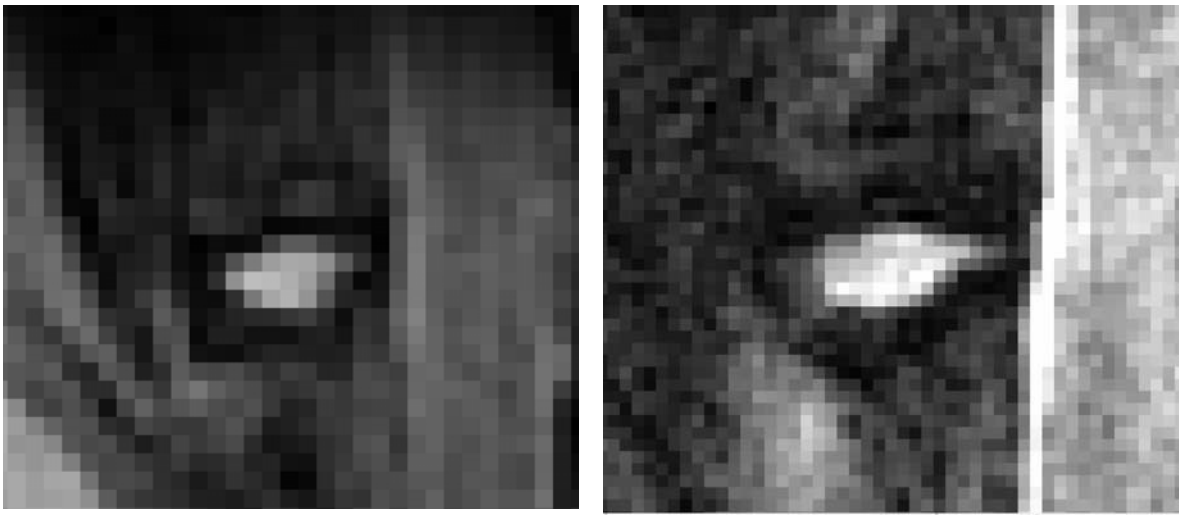

(A) **(B)**

Figure 60. Magnified screen capture of the L1-2 disc obtained with the 5 inch surface coil at 1.5T (256x256 matrix size) (A), and the custom quad coil (512x512 matrix size) (B).

Table 9 shows SNR values of the rabbit scans completed with the 5 inch surface and custom quad coil, at 1.5T and 3.0T respectively.

Table 9. SNR measurements of 5 inch surface and custom quad coils, using 256x256 and 512x512 matrix sizes respectively.

In-vivo SNR Measurements of 5 inch Surface and Custom Quad Coils	
Coil Type	SNR Measurements
5” Surface (1.5T)	27
Custom Quad (3.0T)	25

6.0 DISCUSSION

The quantitative MRI data provides evidence that this is a progressive model of IDD. Although an inflammatory reaction to the acute anular injury is likely to have been present soon after stab, the MRI data suggest that a slow and progressive degenerative process had begun by 3 weeks post stab. The stabbed discs exhibited a progressive decrease in MRI index (the product of NP area and signal intensity from T2-weighted midsagittal plane images) starting at 3 weeks post stab and continuing through 24 weeks, with no evidence of any spontaneous recovery or reversal of MRI changes. These findings suggest that the stab injury induced in this study is a reliable method for initiating a progressive form of disc degeneration in the adult rabbit that does not recover by itself.

The intact control discs (L1–L2 and L5–L6) of the present model may also have undergone some (mild) degenerative changes, possibly because of their proximity to and interaction with the degenerating stabbed discs (L2–L3, L3–L4, and L4–L5). Over the 24-week duration of the present study, the intact control discs exhibited a 16% decrease in mean MRI index from preoperative values, in contrast to the 68% decrease for the stabbed discs over the same period. It is unclear how much of the MRI index decrease for the intact control discs may have been due to normal aging processes as opposed to "adjacent segment" phenomena. If the intact control discs of this stab model do indeed degenerate faster than the corresponding discs of rabbits that do not undergo surgery (i.e., normal aging model), such discs may offer yet another,

more subtle, model of disc degeneration. Evidence suggests that the degenerating stabbed discs may also have interacted with each other in some fashion throughout the study since by 24 weeks, mean MRI index values for the stabbed L2–L3, L3–L4, and L4–L5 discs were nearly the same (~32% of corresponding preoperative values).

In summary, it was found that anterolateral stab of skeletally mature rabbit lumbar discs by 16-gauge needle to a limited (5-mm) depth provides a slowly progressive, reproducible model of disc degeneration in terms of the MRI as an outcome measure. This model appears to be suitable for studying pathogenesis and pathophysiology of IDD and testing safety and efficacy of novel treatments of IDD.

Moreover, a RF coil customized for rabbit lumbar spine at 3.0T with the ability to image the L1-2 – L5-6 IVDs accurately was designed and built. The coil consists of two elements placed such that high isolation is achieved between them. For the rabbit tested, the quad coil at 3.0T permits large FOV imaging with a higher SNR than that achievable with the body coil, head, 5 inch, 3 inch, and license plate coils at 1.5T; and also the body and head coils at 3.0T. Through in-vitro and in-vivo experiments, it was have shown that along its major axes the custom quad coil provides an SNR ~2.0 times greater than the 5 inch surface coil at 1.5T. At the same time, the quad coil provides a longitudinal FOV of ~23 cm, ~77% larger than that of the 5 inch surface coil. In addition, through in-vitro and in-vivo experiments we have quantitatively and qualitatively shown that high resolution images (512x512 matrix size) obtained with the quad coil achieve greater detail than the 5 inch surface coil while maintaining the same SNR.

6.1 COMPARISON TO PREVIOUS LITERATURE

6.1.1 Part 1: Animal Models of IDD

In the present study, anterolateral "stab" of skeletally mature rabbit lumbar discs by 16-gauge needle to a limited (5-mm) depth resulted in a number of slowly progressive and reproducible MRI, radiograph, and histologic changes over 24 weeks that show a similarity to changes seen in human intervertebral disc degeneration (x-ray and histology results not shown in thesis) (Sobajima, 2005 #34). The disc degeneration seemed to occur in a less precipitous manner than that reported for the classic Lipson and Muir (Lipson, 1981 #24) stab model, in which progressive degenerative changes in adult rabbit discs were achieved via a full-thickness, ventral lesion of the lumbar anulus with a number 11 scalpel blade. A contributing factor may be that whereas the approach used by Lipson and Muir results in immediate herniation of the bulk of the nucleus, the present approach does not appear to result in acute loss of nuclear content (immediate herniation of nucleus pulposus was observed in only one 1 of the 54 stabbed discs).

Lipson and Muir 9 hypothesized that "loss of confined fluid mechanics" initiated a final common pathway of disc degeneration in the classic stab model. On the other hand, Osti et al,13 using a sheep model, have shown that disc degeneration can be induced by acute anular injury without immediate herniation. The current model did not exhibit immediate herniation on stab with the hypodermic needle, hence, the degeneration pathway may be different from that of the Lipson and Muir model (at least in its early stages before the "final common pathway").

6.1.2 Development of Custom Coils

Custom coils for MR imaging have been developed to enhance image quality. With a lack of RF coils that specifically address lower extremity needs, Brown *et al* developed a receive-only phased array RF coil optimized for lower extremity imaging. The authors discovered that certain commercially available coils can lack the SNR needed to acquire certain data. For example, although convenient for patient positioning, the body coil attains a poor signal-to-noise ratio. Also, coils that can produce the desired SNRs, at time provide a limited field of view. For example, the knee coil attains high SNR but has a limited region of sensitivity and is not capable of imaging both legs simultaneously. Moreover, patient and animal positioning can be inconsistent with coils like the torso array that are not fixed, and are built on flexible material. Therefore, imaging at specific FOVs, while still maintaining high SNR in the image generally involves constructing custom coils.

6.2 LIMITATIONS

6.2.1 Part 1: Slowly Progressive Animal Model of IDD with 5 inch Surface Coil at 1.5T

The present study has a number of limitations. Although designed primarily as a serial MRI study, it was necessary to sacrifice some animals at intermediate stages for histology, hence there was unavoidable "dropout" in rabbits as time progressed.

Stabilizing the anesthesized rabbit in the 1.5T MR scanner over the 5 inch surface coil was difficult and time consuming, due to a lack of housing for the rabbit and limited size of the 5 inch surface coil. Towels were positioned around the animal to prevent the rabbit from moving

during the scan, which resulted in the rabbit being slightly misaligned over the coil. On many occasions we noticed the spine was bent on the coronal localizer images, resulting in an inability to accurately acquire the T2-weighted sagittal images. In addition, the range of the 5 inch surface coil was approximately the size of the lumbar spine of the rabbit. This resulted in having to reposition the animal and repeating the localizer images. Moreover, due to the varying size of the rabbits it became difficult to accurately capture both the L1-2 and L5-6 control discs in the larger rabbits. We observed signal drop off in some of these discs that possibly can be attributed to an inadequate range of the 5 inch surface coil.

Accuracy of the MRI measurements might benefit from signal intensity normalization at the different time points, which could be achieved by application of a phantom-based method. No special measures were undertaken to account for possible variations in signal intensity across the image (a characteristic drawback of surface-coil MRI). Nevertheless, because the rabbit spines were relatively straight when placed in the magnet, the location of the discs with respect to the surface coil, and therefore their position within the MR images, was quite consistent. Each control disc (L1-2, L5-6) was analyzed for inaccurate signal drop off due to the limitations of the 5 inch surface coil. Accordingly, the authors believe that the changes observed in signal intensity were unlikely to have been influenced greatly by systematic error associated with use of the surface coil. In this regard, it is noted that a number of studies that used MRI in the investigation of dog models of disc degeneration have also reported decreases in T2-weighted signal intensity in degenerating discs.

The magnetic resonance image processing method used in the present study could be improved by implementing automated techniques to analyze the disc, rather than relying on an observer to identify the regions of interest. Nevertheless, intra- and interobserver repeatability

with the present method was quite good. The authors defined MRI index to use its value as an objective reference point to document quantitative changes within the discs of rabbits followed in a longitudinal fashion. The rationale was that the combination of two variables (NP signal intensity and area) in MRI index might better represent the overall degenerative process present in the present model than either variable alone. It is recognized that more sophisticated MRI outcome measures are available 18 that could provide an even more comprehensive picture of disc degeneration in this model. Yet, even with the relatively simple MRI outcome measures used in the present study, MRI proved to be a useful, objective tool to gauge the progression of degeneration in a reasonably quantitative manner as certain biologic processes were occurring within the disc.

6.2.2 Part 2: Custom Quad Coil for Imaging Rabbit Spine

One limitation of the coil is that it can only be used at 3.0T. As technology advances and higher field strength magnets become available the custom quad coil will need to be retuned and matched to function. The use of higher field strengths will allow for even more SNR resulting in larger matrix sizes.

Currently, the 2D imaging technique has been developed with the custom quad coil. To more accurately image the intervertebral disc, volume (3D) techniques need to be developed. This coil currently is limited to 2D scanning, although the possibility of 3D scanning is available with further development.

6.3 FUTURE DIRECTIONS

6.3.1 Part 1: Slowly Progressive Animal "Stab" Model of IDD

The authors are currently measuring gene expression and biochemical profiles to assist in the delineation of the causal pathways of the present model, whereas ongoing biomechanical studies are addressing the mechanical aspects. The authors have also begun using this model to test the efficacy of vector-mediated therapeutic gene transfer in altering the course of disc degeneration. The wide separation between the mean MRI index data of the stabbed and intact control discs (combined with small standard deviations) creates an ample "window of opportunity" for identifying significant effects of therapeutic interventions in the present model.

6.3.2 Part 2: Custom Quad Coil for Imaging Rabbit Spine

The custom quad coil tuned and matched for 3.0T has proven to possess many advantages when compared to imaging at 1.5T. One important advantage involves sacrificing the increased SNR to produce higher resolution images. Researchers are currently developing higher field strength magnets (7 Tesla), which will allow for high resolution imaging while maintaining and also potentially increasing SNR. The custom quad coil has the ability to be tuned to the frequency of 7T, due to the strategic positioning of the variable capacitors.

Moreover, the custom quad coil is currently tuned to the frequency of hydrogen. Future work may involve re-tuning the coil to the frequency of sodium to obtain more quantitative results of the degenerative process. Convincingly, this coil has the capability to be used at multiple field strengths and is not limited to hydrogen scanning. This will prove to be an important advantage in future MR studies to assess IDD.

APPENDIX A

MRI INDEX EACH DISC

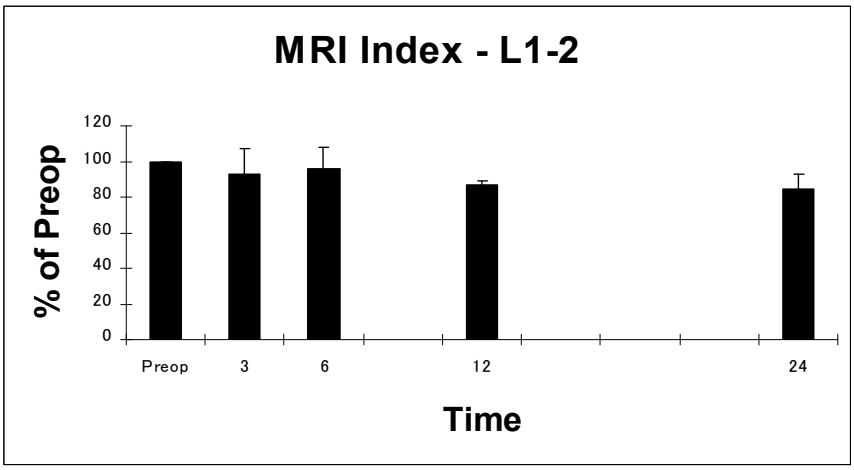

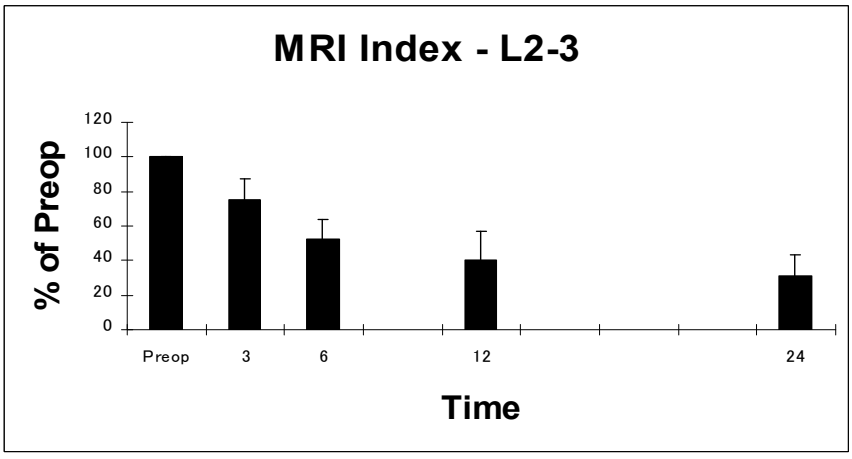

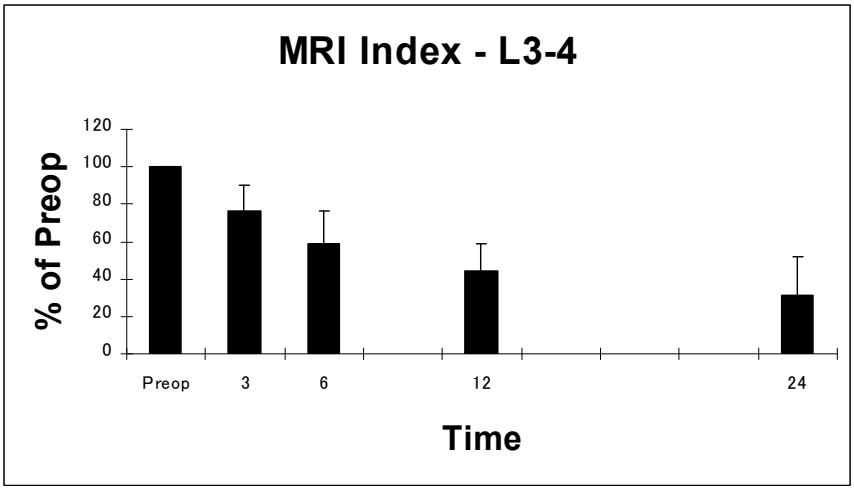
MRI Index - L3-4
% of Preop
120
100
80
60
40
20
0
Preop
3
6
12
24
Time

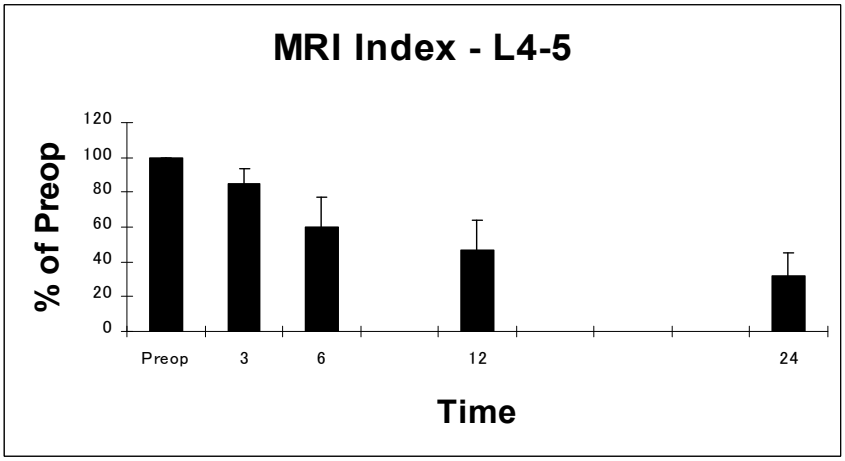
MRI Index - L4-5
% of Preop
120
100
80
60
40
20
0
Preop
3
6
12
24
Time

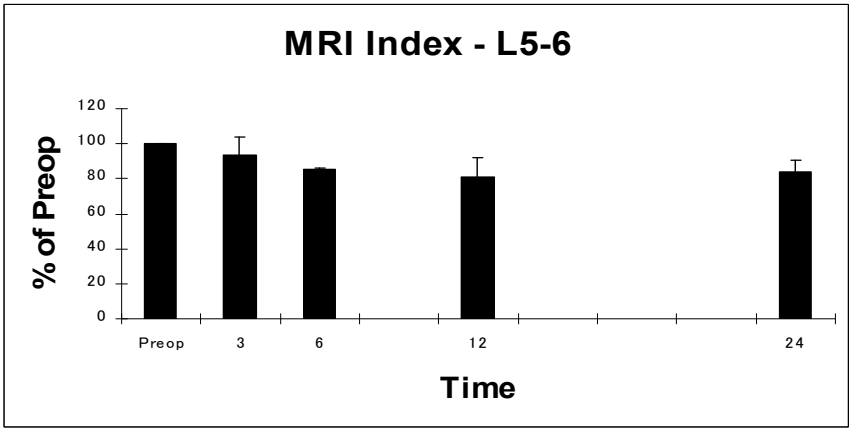
MRI Index - L5-6
% of Preop
120
100
80
60
40
20
0
Preop
3
6
12
24
Time

NP Area Each Disc

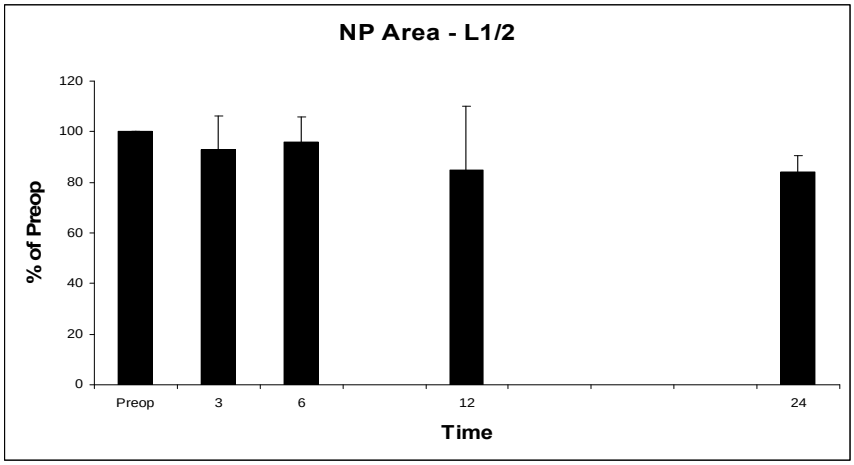

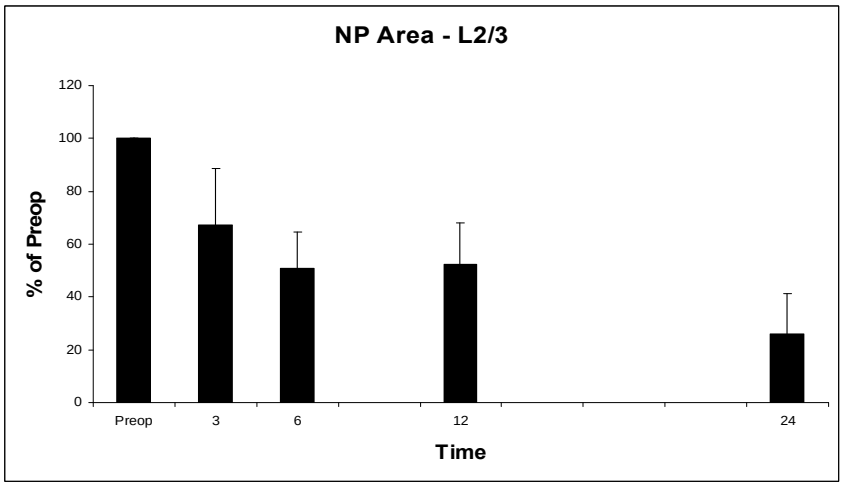

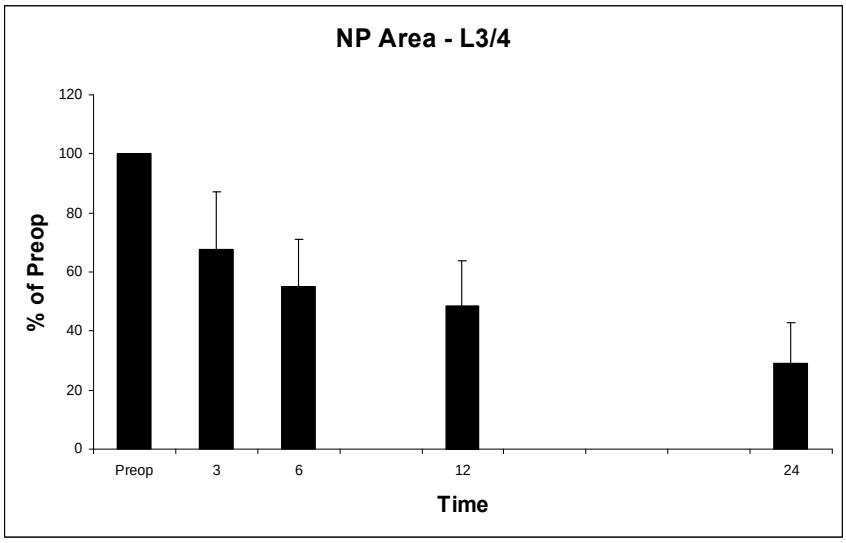

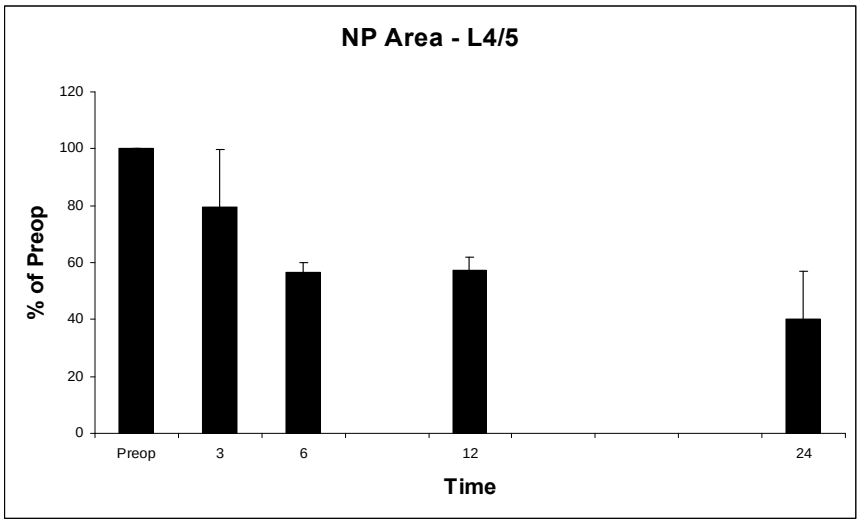
NP Area - L4/5
% of Preop
120
100
80
60
40
20
0
Preop
3
6
12
24
Time

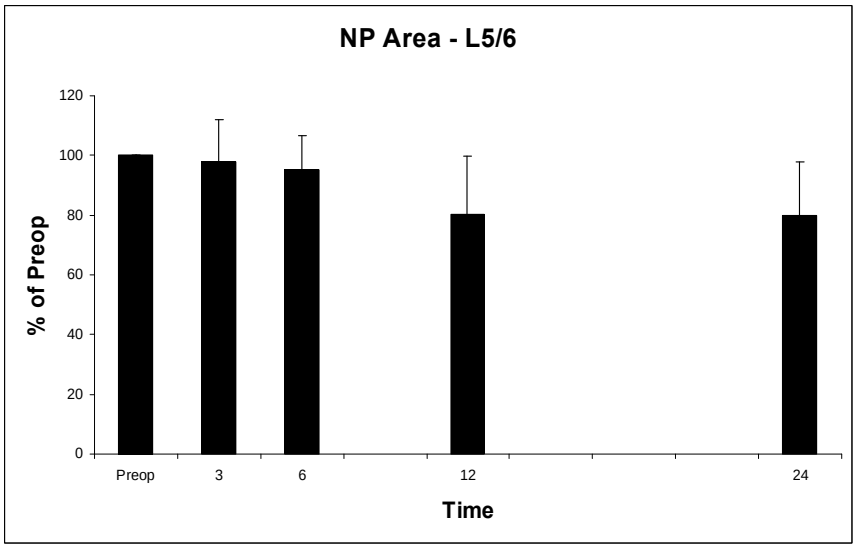
NP Area - L5/6
% of Preop
120
100
80
60
40
20
0
Preop
3
6
12
24
Time

NP SI each Disc

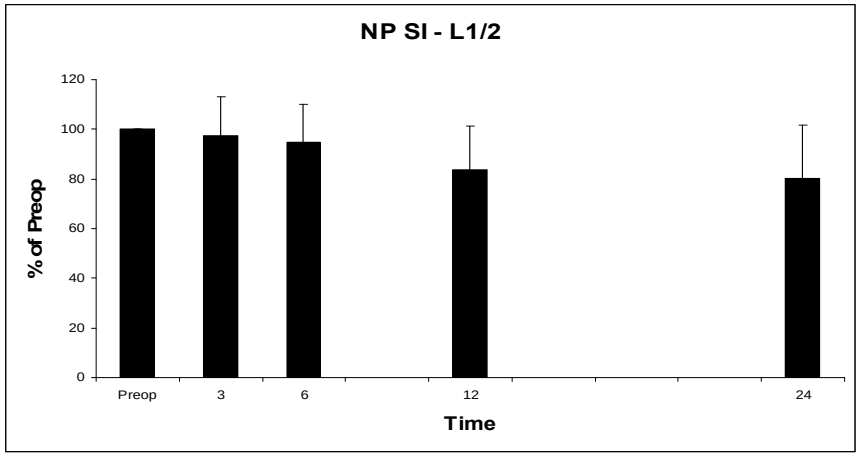

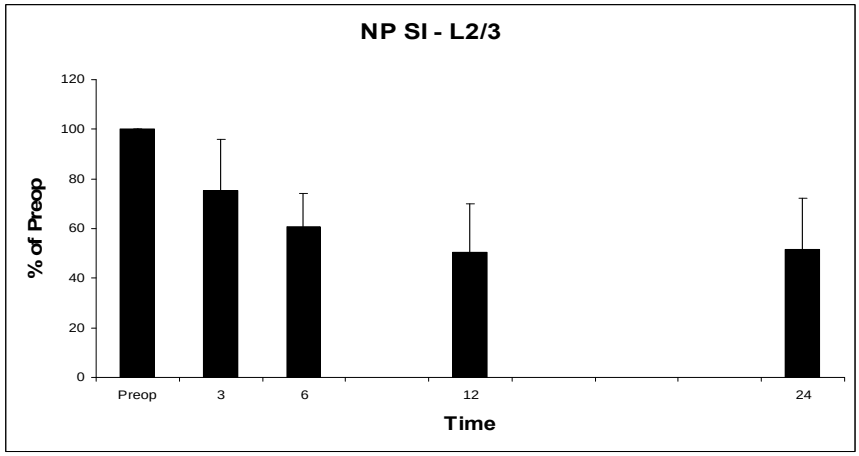

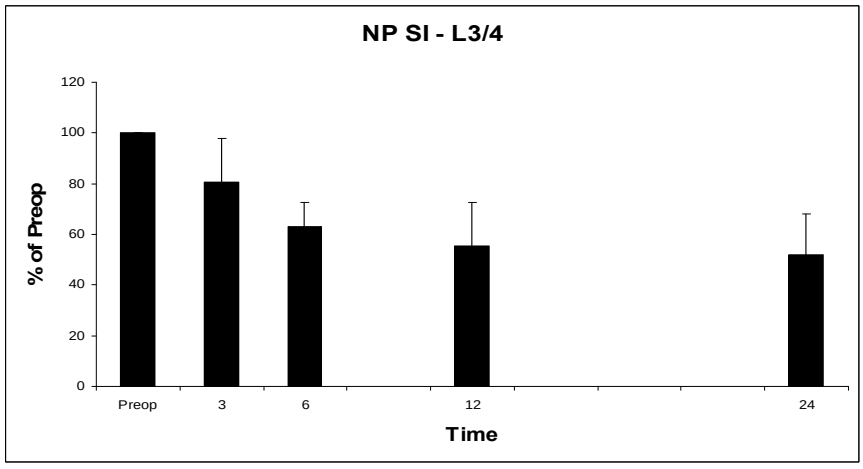

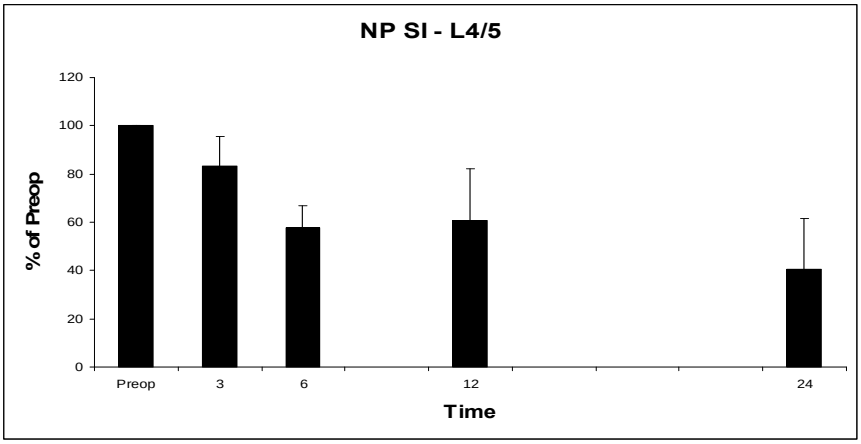
NP SI - L4/5
% of Preop
120
100
80
60
40
20
0
Preop
3
6
12
24
Time

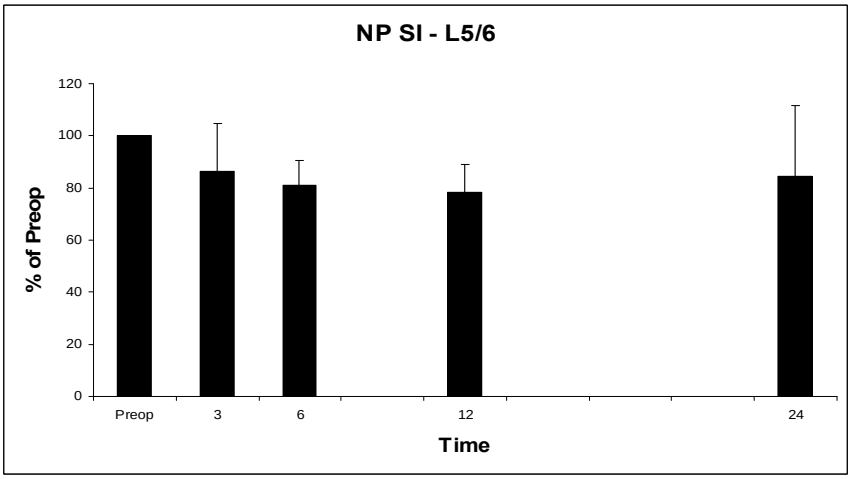
NP SI - L5/6
% of Preop
120
100
80
60
40
20
0
Preop
3
6
12
24
Time

APPENDIX B

AMIRA MRI INDEX

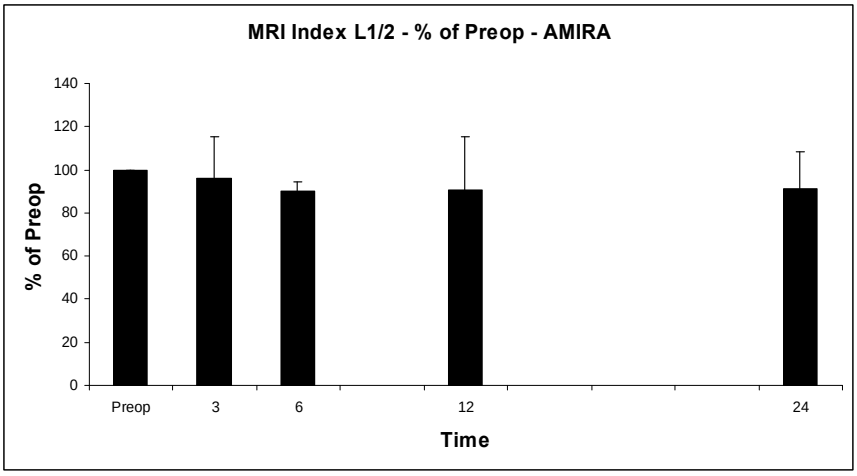

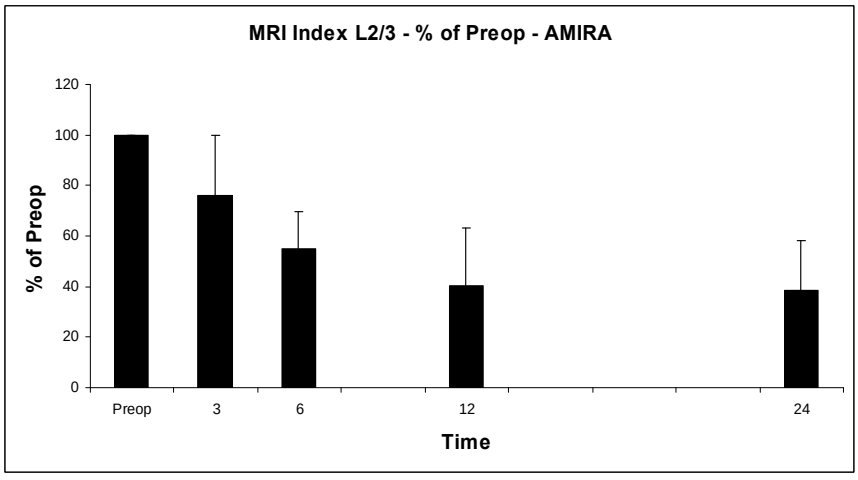

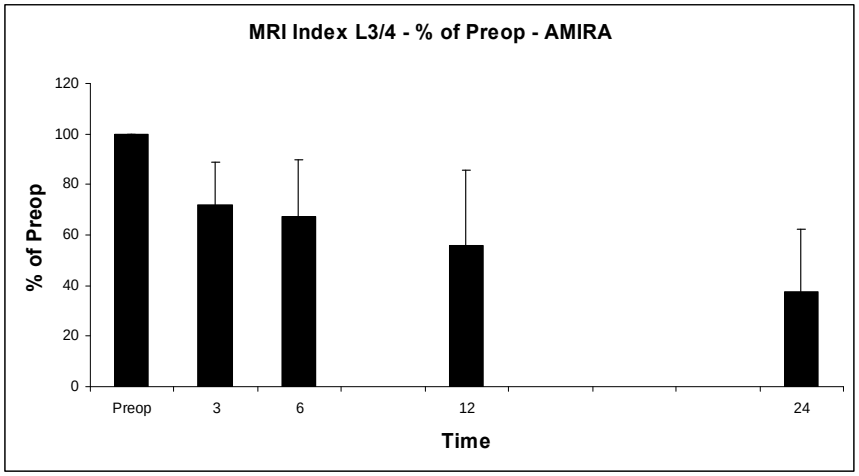
MRI Index L3/4 - % of Preop - AMIRA
% of Preop
120
100
80
60
40
20
0
Preop
3
6
12
24
Time

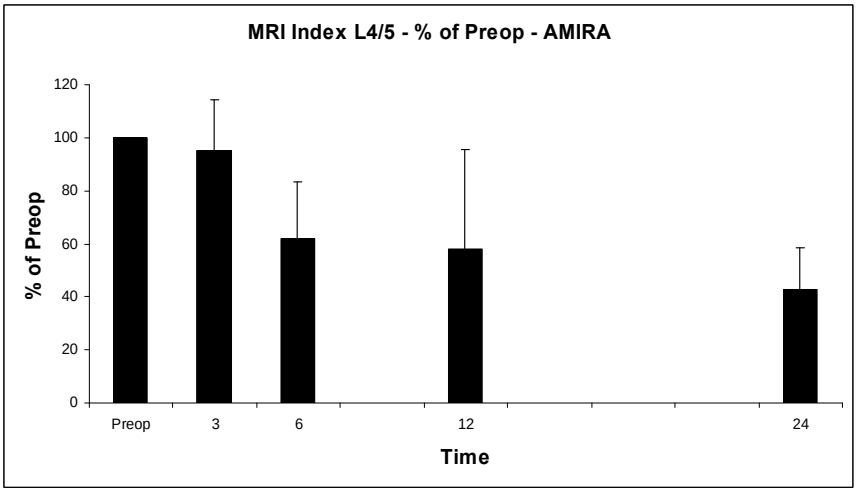
MRI Index L4/5 - % of Preop - AMIRA
% of Preop
120
100
80
60
40
20
0
Preop
3
6
12
24
Time

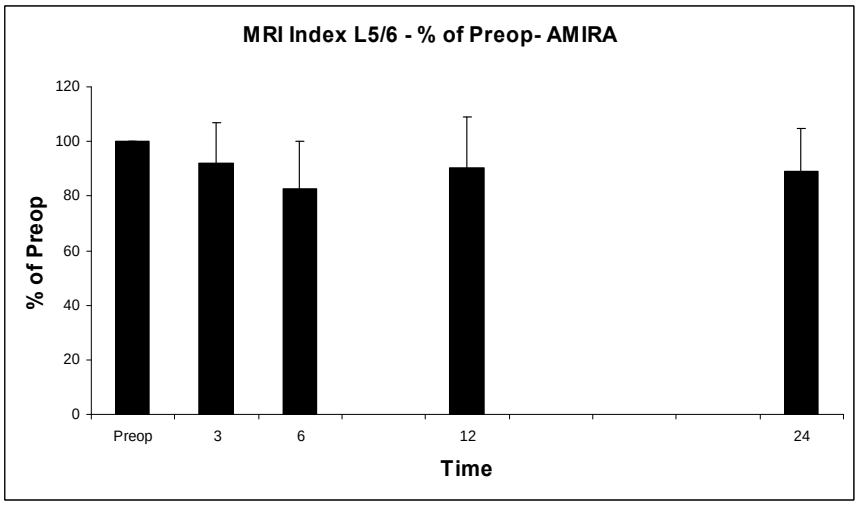
MRI Index L5/6 - % of Preop- AMIRA
% of Preop
120
100
80
60
40
20
0
Preop
3
6
12
24
Time

NP Area
AMIRA

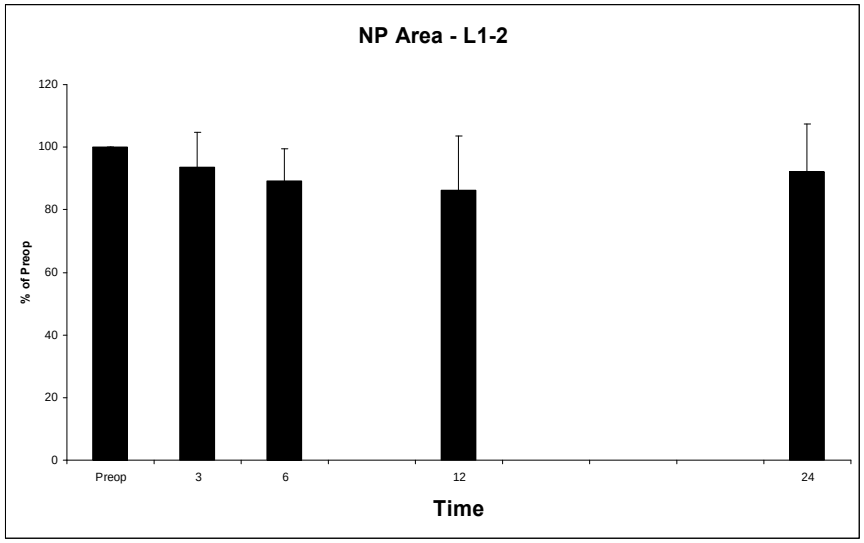

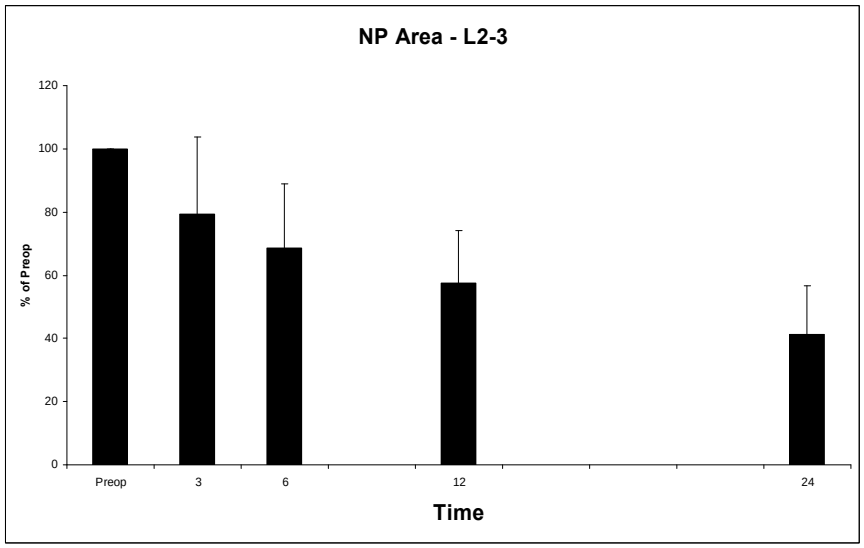

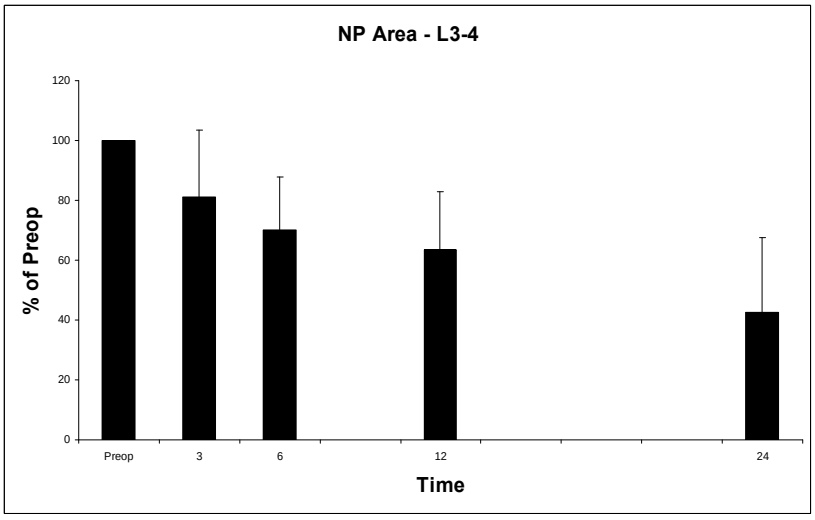

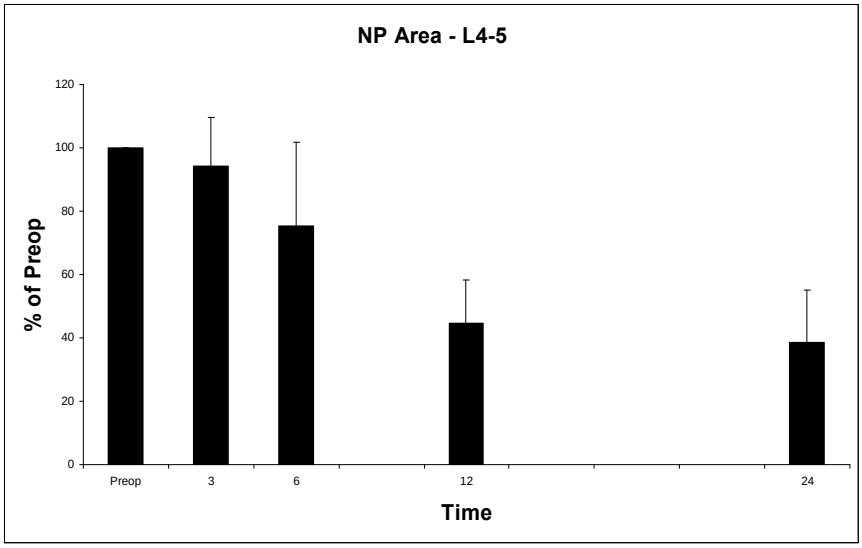
NP Area - L4-5
120
100
80
60
40
20
0
% of Preop
Preop
3
6
12
24
Time

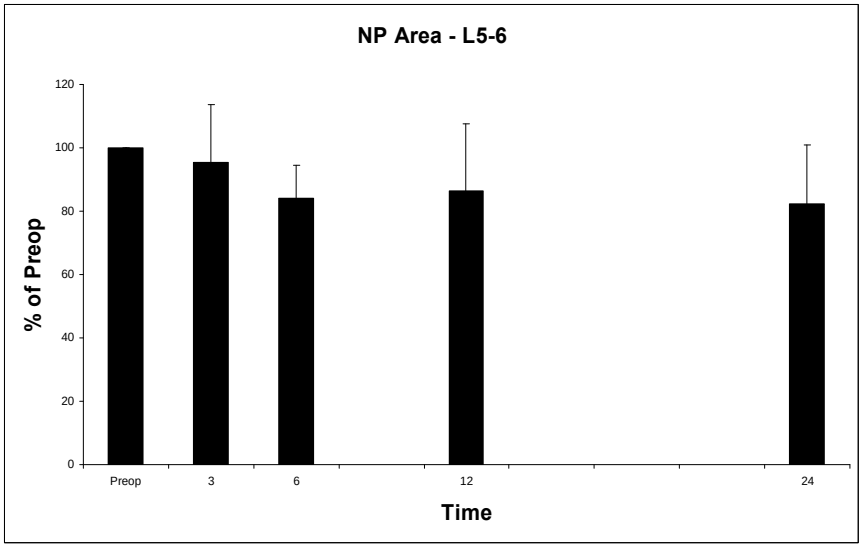
NP Area - L5-6
120
100
80
60
40
20
0
% of Preop
Preop
3
6
12
24
Time

NP SI
AMIRA

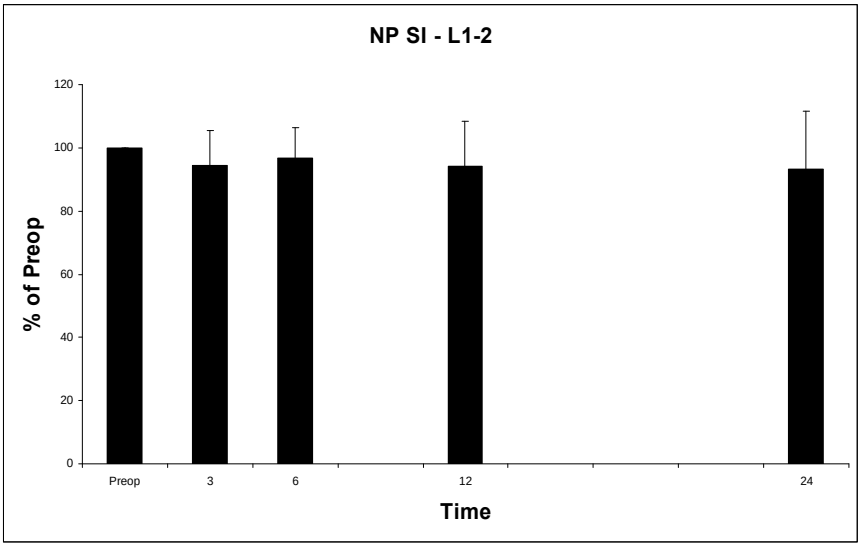
NP SI - L1-2
% of Preop
120
100
80
60
40
20
0
Preop
3
6
12
24
Time

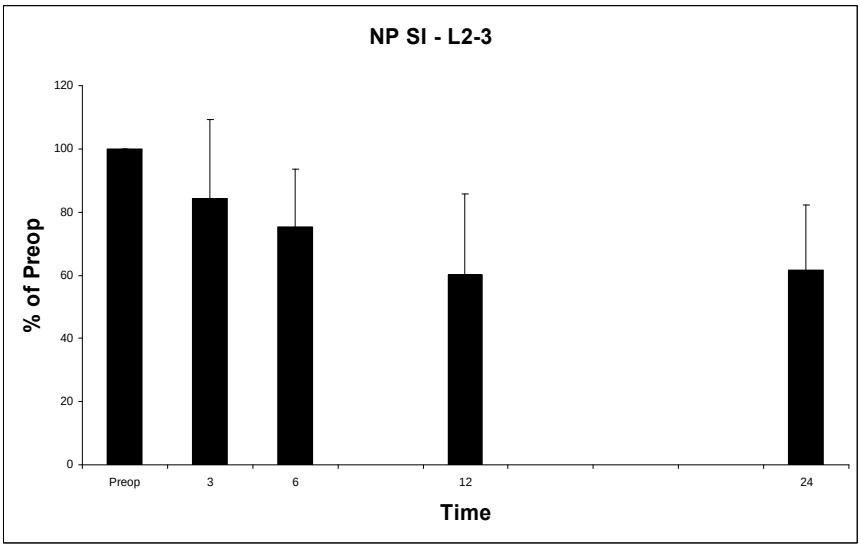
NP SI - L2-3
% of Preop
120
100
80
60
40
20
0
Preop
3
6
12
24
Time

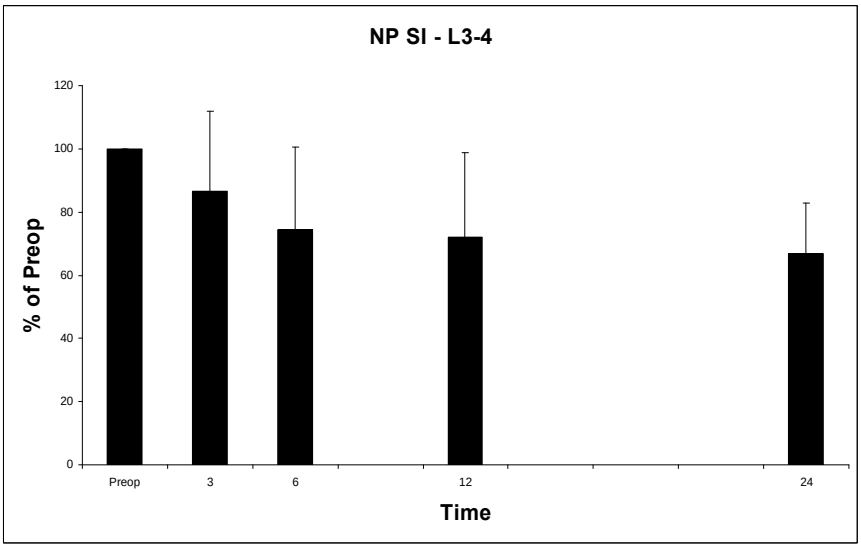
NP SI - L3-4
% of Preop
120
100
80
60
40
20
0
Preop
3
6
12
24
Time

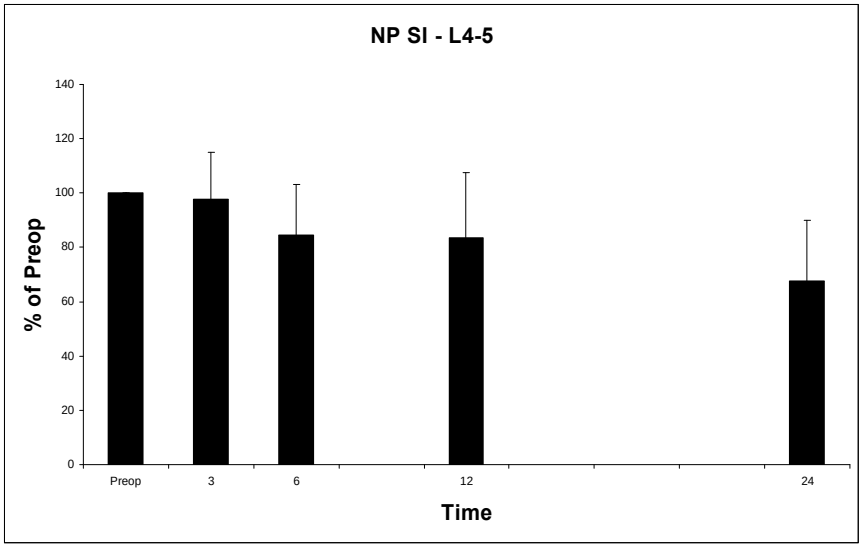
NP SI - L4-5
140
120
100
80
60
40
20
0
% of Preop
Preop
3
6
12
24
Time

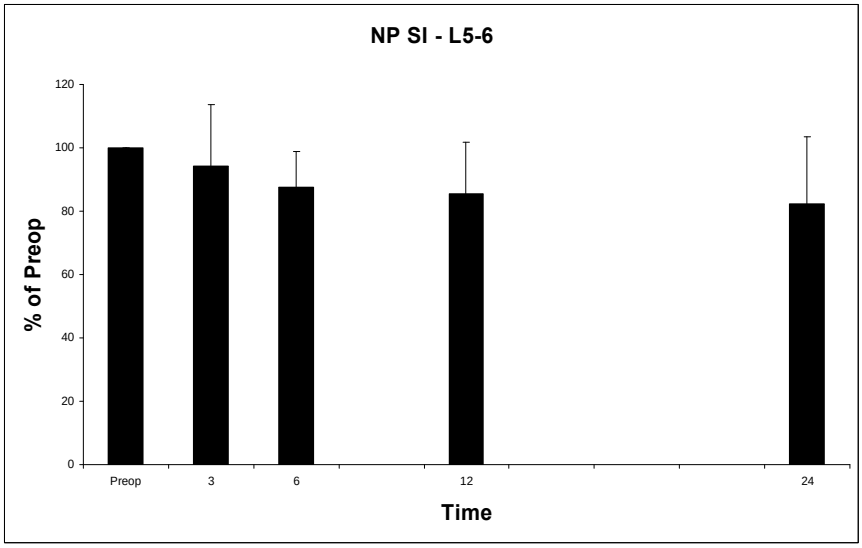
NP SI - L5-6
120
100
80
60
40
20
0
% of Preop
Preop
3
6
12
24
Time

APPENDIX C

NATURAL COURSE MRI INDEX

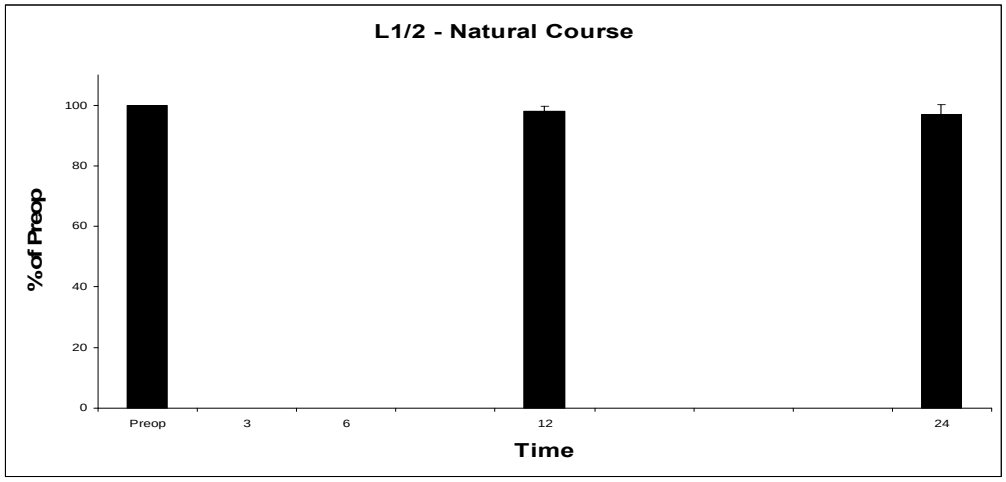

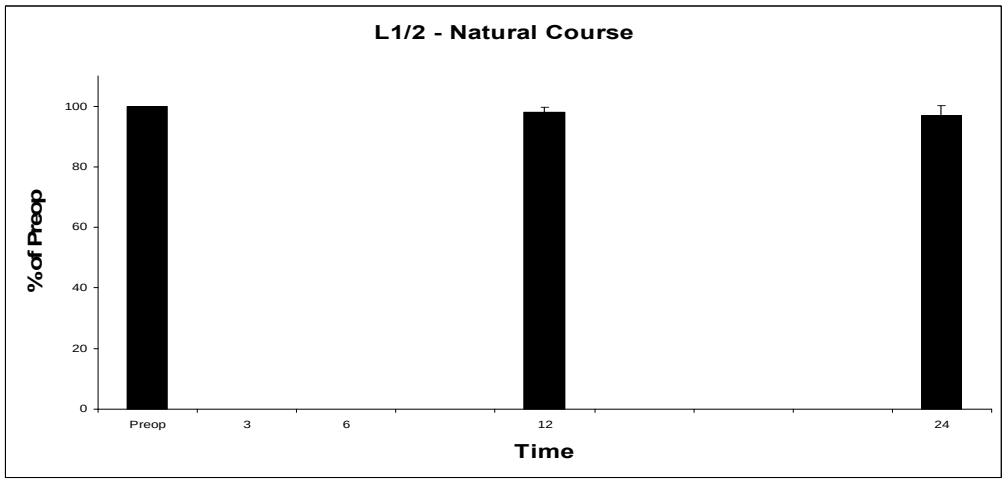

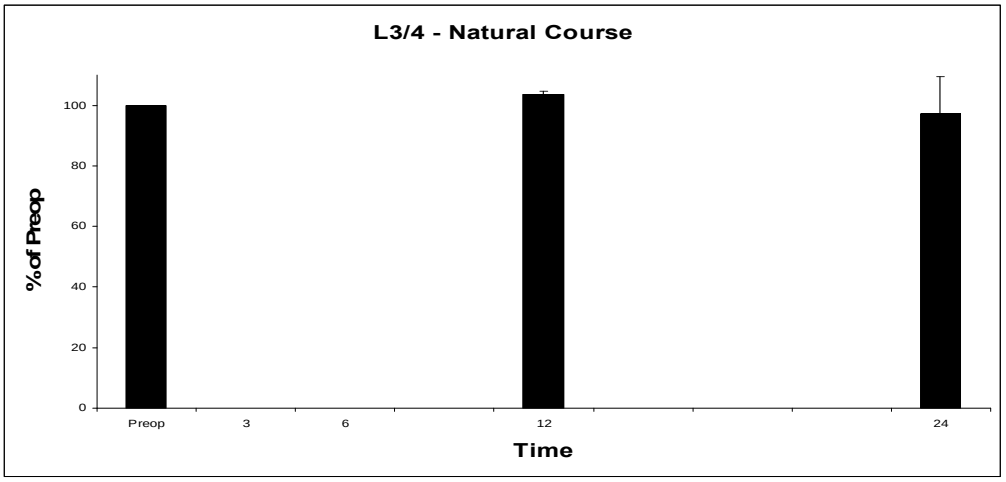
L3/4 - Natural Course
% of Preop
0
20
40
60
80
100
Preop
3
6
12
24
Time

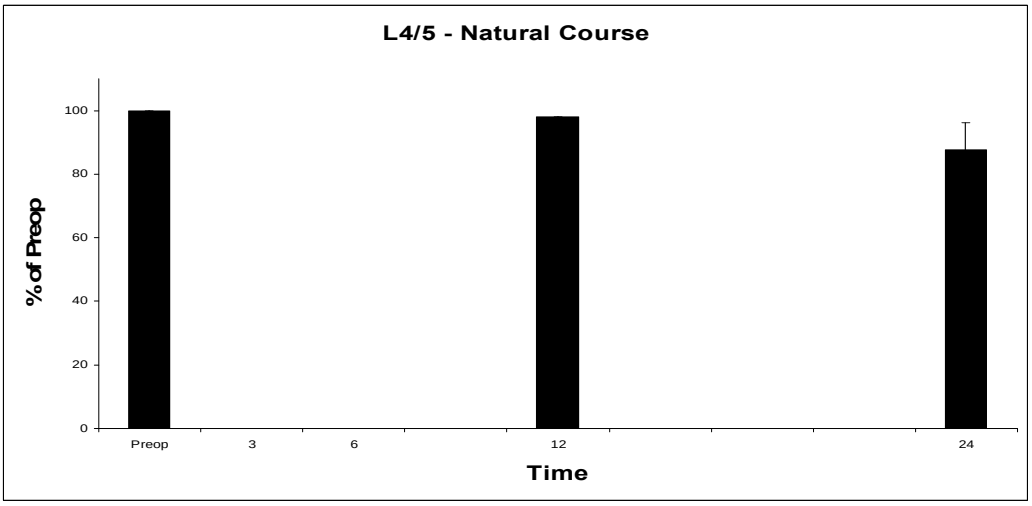
L4/5 - Natural Course
% of Preop
0
20
40
60
80
100
Preop
3
6
12
24
Time

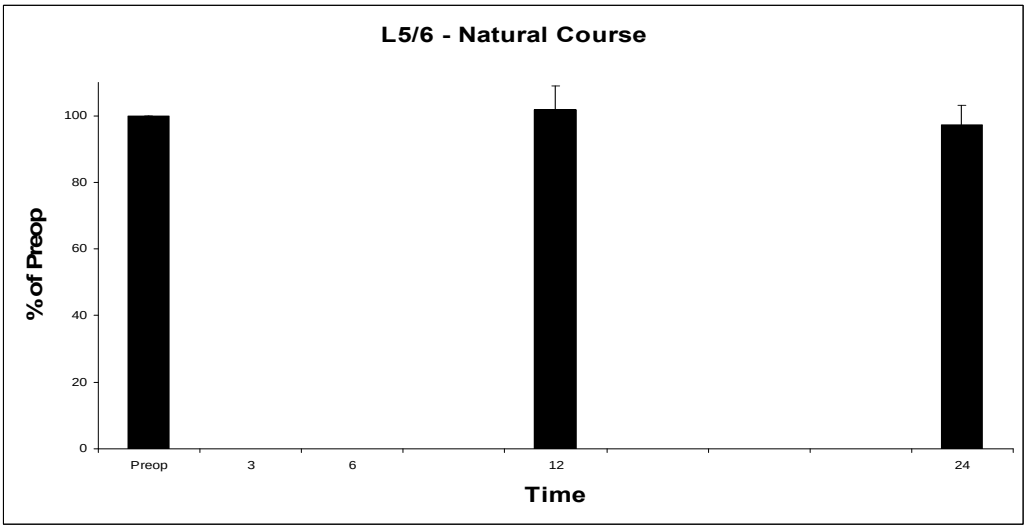
L5/6 - Natural Course
% of Preop
0
20
40
60
80
100
Preop
3
6
12
24
Time

BIBLIOGRAPHY

1. **Benoist, M., *Natural history of the aging spine.* Eur Spine J, 2003. 12 Suppl 2: p. S86-9.**

2. **Niosi, C.A. and T.R. Oxland, *Degenerative mechanics of the lumbar spine.* Spine J, 2004. 4(6 Suppl): p. 202S-208S.**

3. **Walker, M.H. and D.G. Anderson, *Molecular basis of intervertebral disc degeneration.* Spine J, 2004. 4(6 Suppl): p. 158S-166S.**

4. **Guiot, B.H. and R.G. Fessler, *Molecular biology of degenerative disc disease.* Neurosurgery, 2000. 47(5): p. 1034-40.**

5. **Coventry, M.B., *Degenerative changes in the spinal column.* Mayo Clin Proc, 1951. 26(25): p. 473-7.**

6. **Yoon, S.T. and S.D. Boden, *Spine fusion by gene therapy.* Gene Ther, 2004. 11(4): p. 360-7.**

7. **Danielsson, A.J., et al., *The prevalence of disc aging and back pain after fusion extending into the lower lumbar spine. A matched MR study twenty-five years after surgery for adolescent idiopathic scoliosis.* Acta Radiol, 2001. 42(2): p. 187-97.**

8. **Bigos, S.J., et al., *Back injuries in industry: a retrospective study. III. Employee-related factors.* Spine, 1986. 11(3): p. 252-6.**

9. **Georgy, B.A. and J.R. Hesselink, *MR imaging of the spine: recent advances in pulse sequences and special techniques.* AJR Am J Roentgenol, 1994. 162(4): p. 923-34.**

10. **Deyo, R.A., et al., *Cost, controversy, crisis: low back pain and the health of the public.* Annu Rev Public Health, 1991. 12: p. 141-56.**

11. **Evans, W., W. Jobe, and C. Seibert, *A cross-sectional prevalence study of lumbar disc degeneration in a working population.* Spine, 1989. 14(1): p. 60-4.**

12. **Gundry, C.R. and H.M. Fritts, *Magnetic resonance imaging of the musculoskeletal system. Part 8. The spine, section 1.* Clin Orthop, 1997(338): p. 275-87.**

13. **Beattie, P.F. and S.P. Meyers, *Magnetic resonance imaging in low back pain: general principles and clinical issues.* Phys Ther, 1998. 78(7): p. 738-53.**

14. **Gundry, C.R. and H.M. Fritts, *Magnetic resonance imaging of the musculoskeletal system. Part 8. The spine, section 2.* Clin Orthop, 1997(343): p. 260-71.**

15. **Modic, M.T. and J.S. Ross, *Magnetic resonance imaging in the evaluation of low back pain.* Orthop Clin North Am, 1991. 22(2): p. 283-301.**

16. **Gundry, C.R. and H.M. Fritts, Jr., *MR imaging of the spine in sports injuries.* Magn Reson Imaging Clin N Am, 1999. 7(1): p. 85-103.**

17. **Boos, N. and P.H. Lander, *Clinical efficacy of imaging modalities in the diagnosis of low-back pain disorders.* Eur Spine J, 1996. 5(1): p. 2-22.**

18. **Antoniou, J., et al., *Quantitative magnetic resonance imaging in the assessment of degenerative disc disease.* Magn Reson Med, 1998. 40(6): p. 900-7.**

19. **Sether, L.A., et al., *Intervertebral disk: normal age-related changes in MR signal intensity.* Radiology, 1990. 177(2): p. 385-8.**

20. **Chatani, K., et al., *Topographic differences of 1H-NMR relaxation times (T1, T2) in the normal intervertebral disc and its relationship to water content.* Spine, 1993. 18(15): p. 2271-5.**

21. **Georgy, B.A., J.R. Hesselink, and M.S. Middleton, *Fat-suppression contrast-enhanced MRI in the failed back surgery syndrome: a prospective study.* Neuroradiology, 1995. 37(1): p. 51-7.**

22. **Coventry, M.B., *Anatomy of the intervertebral disk.* Clin Orthop, 1969. 67: p. 9-15.**

23. **Eyring, E.J., *The biochemistry and physiology of the intervertebral disk.* Clin Orthop, 1969. 67: p. 16-28.**

24. **Pritzker, K.P., *Aging and degeneration in the lumbar intervertebral disc.* Orthop Clin North Am, 1977. 8(1): p. 66-77.**

25. **Bayliss, M.T., *Proteoglycan structure and metabolism during maturation and ageing of human articular cartilage.* Biochem Soc Trans, 1990. 18(5): p. 799-802.**

26. **Mason, R.M. and A.J. Palfrey, *Intervertebral disc degeneration in adult mice with hereditary kyphoscoliosis.* J Orthop Res, 1984. 2(4): p. 333-8.**

27. **Silberberg, R. and G. Gerritsen, *Aging changes in intervertebral discs and spondylosis in Chinese hamsters.* Diabetes, 1976. 25(6): p. 477-83.**

28. **Hansen, H.J., *A pathologic-anatomical interpretation of disc degeneration in dogs.* Acta Orthop Scand, 1951. 20(4): p. 280-93.**

29. **Goggin, J.E., A.S. Li, and C.E. Franti, *Canine intervertebral disk disease: characterization by age, sex, breed, and anatomic site of involvement.* Am J Vet Res, 1970. 31(9): p. 1687-92.**

30. **Ford, L.T. and J.A. Key, *The experimental production of intervertebral disc lesions by chemical injury.* Surg Forum, 1951. 94: p. 447-53.**

31. **Lauerman, W.C., et al., *Age-related disk degeneration: preliminary report of a naturally occurring baboon model.* J Spinal Disord, 1992. 5(2): p. 170-4.**

32. **Silberberg, R., M. Aufdermaur, and J.H. Adler, *Degeneration of the intervertebral disks and spondylosis in aging sand rats.* Arch Pathol Lab Med, 1979. 103(5): p. 231-5.**

33. **Silberberg, R., *The vertebral column of diabetic sand rats (Psammomys obesus).* Exp Cell Biol, 1988. 56(4): p. 217-20.**

34. **Moskowitz, R.W., et al., *Spondylosis in sand rats: a model of intervertebral disc degeneration and hyperostosis.* J Orthop Res, 1990. 8(3): p. 401-11.**

35. **Adler, J.H., M. Schoenbaum, and R. Silberberg, *Early onset of disk degeneration and spondylosis in sand rats (Psammomys obesus).* Vet Pathol, 1983. 20(1): p. 13-22.**

36. **Smith, J.W. and R. Walmsley, *Experimental incision of the intervertebral disc.* J Bone Joint Surg Br, 1951. 33-B(4): p. 612-25.**

37. **Lipson, S.J. and H. Muir, *Experimental intervertebral disc degeneration: morphologic and proteoglycan changes over time.* Arthritis Rheum, 1981. 24(1): p. 12-21.**

38. **Lipson, S.J. and H. Muir, *1980 Volvo award in basic science. Proteoglycans in experimental intervertebral disc degeneration.* Spine, 1981. 6(3): p. 194-210.**

39. **Lipson, S.J. and H. Muir, *Vertebral osteophyte formation in experimental disc degeneration. Morphologic and proteoglycan changes over time.* Arthritis Rheum, 1980. 23(3): p. 319-24.**

40. **McFarland, E.W. and B.R. Rosen, *NMR instrumentation and hardware available at present and in the future.* Cardiovasc Intervent Radiol, 1986. 8(5-6): p. 238-50.**

41. **Budinger, T.F., *Nuclear magnetic resonance (NMR) in vivo studies: known thresholds for health effects.* J Comput Assist Tomogr, 1981. 5(6): p. 800-11.**

42. **New, P.F., et al., *Potential hazards and artifacts of ferromagnetic and nonferromagnetic surgical and dental materials and devices in nuclear magnetic resonance imaging.* Radiology, 1983. 147(1): p. 139-48.**

43. **Saunders, R.D. and H. Smith, *Safety aspects of NMR clinical imaging.* Br Med Bull, 1984. 40(2): p. 148-54.**

44. **Luechinger, R., et al., *In vivo heating of pacemaker leads during magnetic resonance imaging.* Eur Heart J, 2004.**

45. **Armenean, C., et al., *RF-induced temperature elevation along metallic wires in clinical magnetic resonance imaging: influence of diameter and length.* Magn Reson Med, 2004. 52(5): p. 1200-6.**

46. **Cline, H., et al., *Radiofrequency power deposition utilizing thermal imaging.* Magn Reson Med, 2004. 51(6): p. 1129-37.**

47. **Sobajima, S., et al., *A slowly progressive and reproducible animal model of intervertebral disc degeneration characterized by MRI, X-ray, and histology.* Spine, 2005. 30(1): p. 15-24.**